FLEXURAL ANALYSIS AND MATERIAL CHARACTERIZATION OF LASER WELDED 316L STEEL BLANKS

BY

ADESINA AKEEM YUSUF

A Thesis Presented to the
DEANSHIP OF GRADUATE STUDIES

KING FAHD UNIVERSITY OF PETROLEUM & MINERALS

DHAHRAN, SAUDI ARABIA

In Partial Fulfillment of the
Requirements for the Degree of

MASTER OF SCIENCE

In

MECHANICAL ENGINEERING

DHUL-QA'DAH 1434
(SEPTEMBER 2013)

KING FAHD UNIVERSITY OF PETROLEUM & MINERALS

DHAHRAN- 31261, SAUDI ARABIA

DEANSHIP OF GRADUATE STUDIES

This thesis, written by ADESINA AKEEM YUSUF under the direction of his thesis advisor and approved by his thesis committee, has been presented and accepted by the Dean of Graduate Studies, in partial fulfillment of the requirements for the degree of **MASTER OF SCIENCE IN MECHANICAL ENGINEERING.**

Dr. IYAD T. ALZAHARNAH
(Advisor)

Dr. BEKIR SAMIR YILBAS
(Member)

Dr. AHMET Z. SAHIN
(Member)

Dr. ZUHAIR M. GASEM
Department Chairman

Prof. Salam A. Zummo
Dean of Graduate Studies

29/10/13

Date

DEDICATION

قُلْ إِنَّنِي هَدَانِي رَبِّي إِلَىٰ صِرَاطٍ مُّسْتَقِيمٍ دِينًا قِيَمًا مِّلَّةَ إِبْرَاهِيمَ حَنِيفًا ۚ وَمَا كَانَ مِنَ الْمُشْرِكِينَ (١٦١)

قُلْ إِنَّ صَلَاتِي وَنُسُكِي وَمَحْيَايَ وَمَمَاتِي لِلَّهِ رَبِّ الْعَالَمِينَ (١٦٢)

لَا شَرِيكَ لَهُ ۖ وَبِذَٰلِكَ أُمِرْتُ وَأَنَا أَوَّلُ الْمُسْلِمِينَ (١٦٣)

(161) Say (O Muhammad صلى الله عليه وسلم): "Truly, my Lord has guided me to a Straight Path, a right religion, the religion of Ibrahim (Abraham), Hanifa [i.e. the true Islamic Monotheism - to believe in One God (Allah i.e. to worship none but Allah, Alone)] and he was not of Al-Mushrikun."

(162) Say (O Muhammad صلى الله عليه وسلم): "Verily, my Salat (prayer), my sacrifice, my living, and my dying are for Allah, the Lord of the 'Alamin (mankind, jinn and all that exists).

(163) "He has no partner. And of this I have been commanded, and I am the first of the Muslims."

--Sooratul-An’aam, 161 – 163

ACKNOWLEDGMENTS

All praise belongs to Allaah, to Him alone worship is to be directed. I am really grateful to Him for His numerous favors and bounties upon me to this age and stage in life, **AlhamduliLLaah**.

Thereafter, I really appreciate the efforts of my parents, Mr Y. Adesina and Mrs Khadeejah, towards me and for what they bore for me to get to this level. May Allaah bless and reward them both with the best of reward. To my immediate family; my wife Mrs Bilqis O. Adedapo, 'Umar and Hafsah for their patience and understanding, may Allaah ease your affairs and grant you Jannah.

This acknowledgement will be incomplete without appreciating the effort of my thesis advisor Dr Iyad T. AlZaharnah. He is always accommodating, listening, and understanding and always ready to render help, I indeed appreciate your encouragement and brotherly advice during the course of this study. Also, indispensible in this list of appreciation is the Distinguished Professor Bekir S. Yilbas whose contribution to the success of this work cannot be overemphasized, indeed I benefited from what Allaah has bestow you of knowledge. Dr Ahmet Z. Sahin's contribution as member of my thesis committee is highly applauded as well. Also, in this list of appreciation are Dr Tahar Laoui, Mr Khalid Naseem, Dr Faadi and Dr Atia, who had really rendered their wealth of experience to the success of this study.

To my friends and colleagues, I say JazaakumuLLaah khayrah fid-duniyah wal aakhirah for the brotherly companionship. In this regard, I appreciate the advises and helping hand rendered by my beloved brothers; Bro. Sadiq Damilola Owoduuni, Bro Sabith Yonus N.

Dr Sunday Olatunji Olushola (aka Abu Aisha), Bro Tariq Muhammad – my current roommate, Bro Abdulhafeedh Kola Popoola, Bro Naasir Ibraheem, Bro Safiullah Yinka Sanusi and the list will be inexhaustible to mention all who had influence my thought and/or be of assistance to me during my study. May Allaah reward you all with much good, BaarakaLLaahu feekum.

I also appreciate the effort and patience of our beloved fathers and teachers in the 'deen'; Sheikh Muhammad bin Ramzam Al-Haajiree, Sheikh AbdulQaadir bin Junaid Al-Quroshee and Sheikh Baraak bin Riyadh. May Allaah preserve them and bless their effort in teaching the *Ummah* the 'deen'.

ABSTRACT

Full Name : [Adesina Akeem Yusuf]

Thesis Title : [Flexural Analysis and Material Characterization of Laser Welded 316L Steel Blanks]

Major Field : [Mechanical Engineering]

Date of Degree : [September 2013]

Modal test for flexural analysis and metallurgical characterization of laser welded 316L Austenitic Stainless Steel (ASS) blanks are considered, since laser welding offers considerable advantages over the conventional welding techniques such as high precision of operation, increased welding speed, and narrow heat affected zone. Laser welding also provide improved mechanical and metallurgical properties of the weld section, due to localized high intensity heating, as compared to those produced by the conventional techniques. Despite these advantages, the high cooling rates associated with laser welding process results in microstructural changes which eventually changes the mechanical and flexural response of the welded region. Consequently, it is necessary to investigate the metallurgical changes, the effect of the laser welding parameters and mechanical properties, such as the hardness of the weld sections. In addition, the effects of workpiece thickness on the laser weld quality and metallurgical changes in the fusion zone are studied. Flexural analysis technique in which the natural frequency is use to characterized flexural response of the welded region is employed. For the modal testing, data acquisition system coupled with a physical flexural experimental set-up was used to capture the natural frequency of the welded blanks. The quality of the weld and the

microstructural changes are examined using Optical Microscope, SEM and Vickers Microhardness testing machine. Simulation of the welding process is also performed to predict the temperature distribution and stress analysis. Finite element software code ANSYS 14.0 is employed for the simulation. It is found that the difference between the natural frequencies of the "as received" and welded samples reaches a maximum of about 12%. The modification of the elastic modulus at the welded region and the subsequent effect on the moment of inertia of the system are responsible for the new natural frequencies. Analysis of the results reveals that sample thickness is the most influential parameter influencing the natural frequency and stiffness of the system. Metallurgical examination shows that the welded region consists of dendritic and cellular structures at positions near and away from the center line respectively with austenitic phase. However, lowering the welding speed shows a positive effect on the microstructure due to high solidification and cooling rates, while increasing the beam power and workpiece thickness results in grain coarsening because of increased heat input. Also, the microhardness of the fusion zone drops rapidly from the near fusion boundary to the certerline. The heat affected zone (HAZ) experiences grain growth due to self annealing process which causes the observed reduction in the microhardness of the HAZ. It is found that the stress attains high values in the cooling cycle after the solidification of the molten regions. The weld bead width predicted agreed well with the SEM bead width measurements.

ملخص الرسالة

الاسم الكامل: اديسينا أكيم يوسف

عنوان الرسالة: تحليل الانحناء وتوصيف للمواد الفولاذ المقاوم للصدأ الأوستنيتي 316L الملحوم بالليزر

التخصص: الهندسة الميكانيكية

تاريخ الدرجة العلمية: سبتمبر 2013

فى هذه الرسالة تم نمذجة وتحليل الانحناء والتوصيف الميتالورجى لمواد الفولاذ المقاوم للصدأ الأوستنيتي 316L الملحوم بالليزر . لحام الليزر له مميزات مقارنة بطرق اللحام التقليدى مثل ان دقة التشغيل عالية وزيادة سرعة اللحام وتقارب المنطقة المتاثرة بالحرارة. لحام الليزر أيضا يعطى الخواص الميكانيكية وميتالورجية لوصلة اللحام، نظراً للكثافة العالية لحرارة التسخين بالمقارنة مع تلك التي تنتجها طرق اللحام تقليدية. على الرغم من هذه المزايا، ارتفاع معدلات التبريد المصاحب للحام الليزر يؤدى الى تغيرات فى البنية المجهرية والتى تغير الاستجابة الميكانيكية ومقاومة الانحناء للمنطقة الملحومة.

ونتيجة لذلك، من الضروري دراسة التغييرات المعدنية، تأثير متغيرات عملية اللحام بالليزر و الخصائص الميكانيكية، مثل صلادة مقطع اللحام. وبالإضافة إلى ذلك، تاثير سمك الوصلة الملحومة على جودة لحام الليزر و التغييرات المعدنية في منطقة الانصهار. تقنية تحليل الانحناء والتى فيها التردد الطبيعي يستخدم لتوصيف استجابة الانحناء فى المنطقة الملحومة تم تطويره. ،و استخدم نظام تجميع البيانات مقترنا ب تختة اختبار الانحناء لالتقاط الترددات الطبيعية للوصلات الملحومة.

تم فحص جودة اللحام والتغييرات الحادثة فى البنية المجهرية باستخدام المجهر الضوئي،و المجهر الالكترونى وماكينة اختبار الصلادة فيكرز.. أيضا تم إجراء محاكاة لعملية اللحام للتنبؤ بتوزيع درجة الحرارة وتحليل الاجهادات.

تم استخدام طريقة العناصر المتناهة الصغر وبرنامج ANSYS 14.0 للمحاكاة. وجدت أن الفرق بين الترددات الطبيعية "المعدن المستلم" و العينات ملحومة عينات يصل إلى بحد أقصى الى حوالي 12%. تعديل معامل مرونة في المنطقة الملحومة وأثر لاحقاً على القصور الذاتي للنظام هو المسؤول عن الترددات الطبيعية الجديدة. تحليل النتائج يعكس أن سمك العينة هو المتغير الأكثر تأثيرا على التردد الطبيعى وجساءة النظام .

ويبين الفحص المعدنى أن المنطقة الملحومة تتكون من بنية شجرية وخلوية فى المواضع القريبة والبعيدة عن خط اللحام على التوالي مع طور الأوستنيتي. ومع ذلك، تخفيض سرعة اللحام يبين تأثير إيجابي على البنية المجهرية بسبب ارتفاع معدلات التجميد والتبريد ، بينما مع زيادة طاقة الشعاع وسمك الوصلة ادى الى سماكة الحبيبات نظراً لزيادة الحرارة الداخلة.

أيضا، انخفضت الصلادة (ميكرو) من منطقة الانصهار الى خط المنتصف. فى المنطقة المتاثرة بالحرارةحدث نمو للحبيبات وذلك بسبب عملية التخمير والتى تسببت في الانخفاض الملحوظ في الصلادة (الميكرو). وجد ان الاجهاد يظل عند قيمة عالية في دورة التبريد بعد تجمد المناطق المنصهره. عرض منطقة اللحام الذى تم التنبؤ به باستخدام البرنامج اتفق تماما مع نتائج التى حصلنا عليها بالمجهر الالكترونى.

TABLE OF CONTENTS

LIST OF FIGURES

LIST OF TABLES

LIST OF SYMBOLS

a = Acceleration (m/s^2)

b = Breadth (m)

c_p = Specific heat capacity (J/kgK)

D = Amplitude of signal (m)

d = Displacement (m)

d = Thickness (m)

E = Young Modulus (N/m^2)

f = Circular Frequency (Hertz)

f_n = Circular Natural frequency (Hertz)

I = Second moment of area (m^4)

K = Stiffness (N/m)

k =Thermal conductivity (J/K)

L = Length (m)

l = Length (m)

M = Total Mass (kg)

m = Mass per unit length (kg/m)

m_a = Mass of accelerometer (kg)

m_{ef1} = Effective mass (kg)

$\dot{q}$ = Heat Flux (W/m^2)

S_0= Volume heat-source (W/m^3)

t = Time (s)

ν = Velocity (m/s)

w = width (m)

ρ = Density (kg/m^3)

ω = Angular frequency (rad/s)

ω_d= Damped frequency (rad/s)

ω_{nf} = Natural Frequency (rad/s)

ξ = Damping coefficient

CHAPTER ONE

1.0 INTRODUCTION

1.1 Background

The exceeding merits of laser welding, which include noncontact welding process with minimal thermal distortion, high precision and relatively high welding speed/high energy density, had increased its applications over the past two decades. In addition, fine grain structure/excellent weld quality, low costs and increased productivity were also responsible for its adoption in automobile, aircraft, marine, aerospace and medical device manufacturing industries substituting other welding techniques. Material versatility of laser welding is another advantage that has made the process more acceptable to the industries. Low carbon steels are considered good candidate for laser welding processes because high carbon content can promote solidification cracking. The 316L stainless steel is an extra-low carbon version of grade 316, it minimizes harmful carbide precipitation due to welding. Due to this property (low carbon: 0.03% max) amongst other austenitic stainless steels, 316L steel has become an important material both to researchers and manufacturers.

This research aims to investigate the effects of laser welding and the geometry parameters on laser welding of 316L steel blanks. This study was carried out by analyzing the mechanical and metallurgical properties of full penetration laser welded materials. Also, the modal analysis is conducted to investigate the effects of these parameters on the welded materials. The natural frequency which is a modal parameter is then used to characterize the welded materials. Micro-hardness testing and optical microscope, Field Emission Scanning Electron Microscope

(FESEM), Elemental Dispersion Spectroscopy (EDS), X-ray Diffraction (XRD) are utilized to study the mechanical and metallurgical characteristics accordingly.

The following sections of this chapter give an overview of the principles and processes of laser welding and modal analysis:

1.2 Laser Welding

Laser welding is a high energy-density, low heat input process with specific advantages over the conventional fusion welding process. In some applications, laser welding is commonly replacing MIG, MAG and resistance spot weld process, it is a kind of evolution that cannot be avoided [1, 2]. The following sub-section discusses the principle, types, mechanism of laser welding as well as some laser welding considerations such as laser welding parameters, material selection and microstructure of laser welded materials.

1.2.1 Principle of Laser Generation

Laser generation is the result of energy emission this is associated with the transition of an electron from a higher to a lower energy level or orbit within an atom[3].

The generation of a laser beam is essentially a three step process that occurs almost instantaneously as follows:

When an atom is irradiated with photons, the electrons are excited or stimulated to a higher energy level by absorbing the energy of the incident photons. This process is referred to as absorption or stimulated absorption. The energy absorption rate depends proportionally on the number of atoms at the lower energy level and the energy density of the incident photons. Due to the excitation of electrons to higher energy levels, the atom becomes unstable and seeks to return to the ground state, thereby emitting some of its energy as photons. The emission is because the

atom always seeks to return to the ground state and if left alone, they would return, just a matter of time before they do. The emission process can occur in two ways, either by spontaneous and/or stimulated emission.

The spontaneous emission happens when the transition from a higher energy level to a lower energy level occur naturally without being stimulated by incident radiation. If the atom is fully stable in its excited state, then no spontaneous emission will occurs.

If the atom in its excited state is irradiated again with photons, the photons will stimulate the atom to undergo a transition to the lower energy level. This is what is called stimulated emission. The energy release due to this transition in form of photons is the same as the incident stimulating photons, and it is superimposed on the incident photons, hence strengthening the emitted photons. This results in stimulated emission, where the incident and emitted photons have the same characteristics and are in phase, resulting in a high degree of coherence, and the direction, frequency, and state of polarization of the emitted photons are essentially the same as those of the incident photons[3]. The two photons can generate an avalanche of photons within the atom by repetitive occurrence of the stimulated emission also referred to as amplification by stimulated emission as illustrated in Figure 2.

1.2.2 Laser Welding Types

Laser welding is a process that melts and joins metals by heating them with a laser beam. The laser beam is produced using a gas mix of CO_2 , N_2 and He, which is continually excited by electrodes, to produce a collimated photon beam [4]. Laser welding became invoke in the industry due to its various meritorious advantages ranging from higher speed/precision, welding of complex joint geometry, low heat application which means less microstructural alterations, low thermal distortion and relatively cavity-free welds.

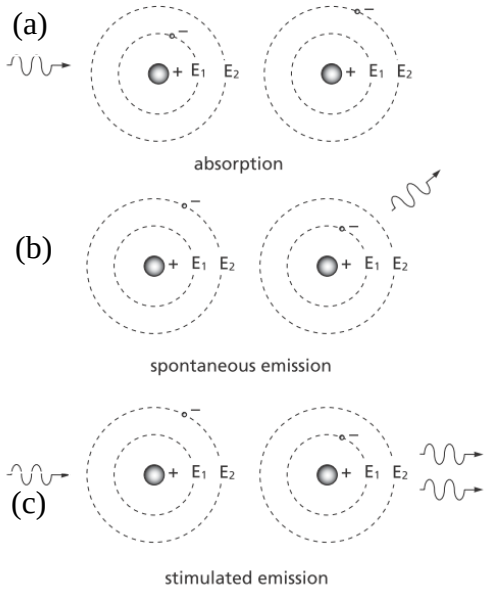

Figure 1: Schematic of (a) absorption, (b) spontaneous emission, and (c) stimulated emission[5]

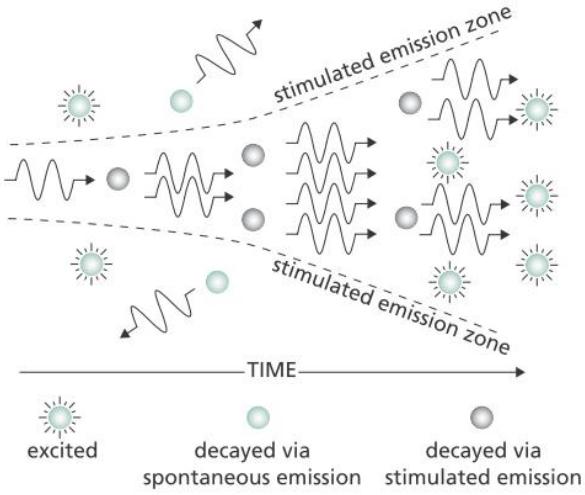

Figure 2: Amplification by stimulated emission[5]

The often use laser for welding are the CO_2 and neodymium:yttrium-aluminum-garnet (Nd:YAG) Lasers. CO_2 Laser is conventionally used for continuous welds because high power

continuous wave (CW) beams are achieved by using CO_2 lasers. Not until recent advancement in high-power continuous wave Nd:YAG lasers, Nd:YAG have been used for spot welding of small components like medical instruments, razor blades etc.[6]

1.2.3 Material Selection Consideration

As with other joining technologies where certain materials are not favored, laser can weld wide range of materials but some materials are more suitable for laser welding as well as there exist materials that are difficult or impossible to weld with laser. The deterministic material properties, specific to laser welding are; a) the material reflectivity, b) the effect of the high thermal cycling and c) the vaporization of volatile alloying elements. The most widely laser welded material is steel, and the general rule is to keep its carbon content below 0.12% [7]. Welding gas plays a major role in the laser welding as it increases the welding speed and enhances the mechanical properties of the weld.

1.2.4 Laser Welding of Steels

As earlier mentioned, laser is generally suitable for welding low carbon steels. However, an increase in the carbon content above 0.25% may require heat treatment before the actual welding to avoid the formation of brittle microstructures due to the high cooling rate that usually happens while welding with laser. On the contrary, high cooling rate can be beneficial in producing fine-particle strengthening as in high-strength low alloy (HSLA) steels but during arc welding of HSLA this result in strength reduction [3].

1.2.5 Laser Welding Parameters

The major parameters that affect laser welding process include the laser power, the traverse velocity, the shielding gas, the joint type, the beam characteristics and the focusing distance which is the distance between specimen and the optical focal points. It was reported that the penetration depth increases with increasing laser power (

Figure 3). Laser power has a less influence on both weld profile and HAZ width in comparison with its effect on penetration depth [8]. The welding speed plays a significant role in the size and shape of the fusion zone. An increase in the welding speed will lead to an increase in the weld-depth to width ratio which means a decrease in the fusion zone size. The welding (shielding) gas often plays an active role in the welding process, such as increasing the welding speed and improving the mechanical properties of the joint [6].

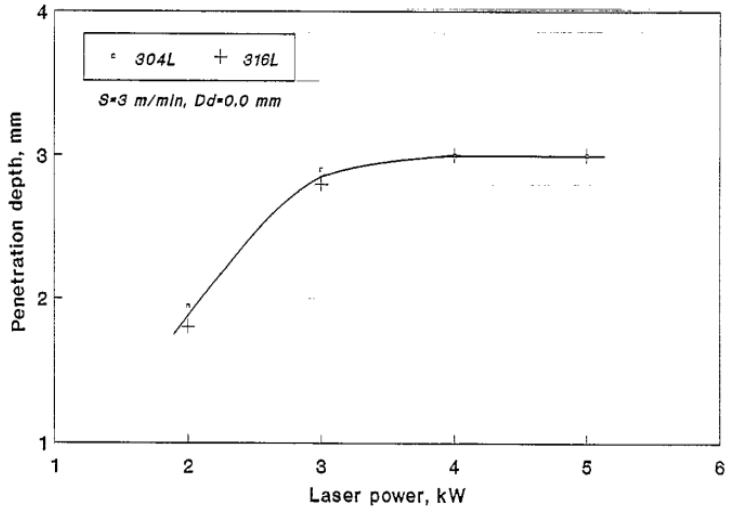

Figure 3: Effect of laser power on penetration depth of type 304 and type 316L steel welds [8]

1.2.6 Mechanism of Laser Welding

When the laser beam is irradiated on a workpiece surface, a significant percentage of the beam energy is reflected away while the remaining percentage is absorbed by the surface. The absorbed energy heats up the surface thereby increasing it temperature. With raise in temperature, the surface absorptivity increases which helps increasing the temperature further. A level is reached where melting and possible evaporation of the metal are localized which creates a vapor cavity within the metal. Hence, laser welding can be of two types based on the mechanism:

a. The conduction mode (Conduction Limited) welding
b. The keyhole (Deep Penetration) welding

The conduction mode is usually employed for welding foils and thin sheets, while keyhole mode welding is used for relatively thick workpiece. Both mechanisms are hereby described briefly:

a. The Conduction Mode Welding

This mode of laser welding occurs at a low power density (less than 10^6 W/cm^2) with minimal workpiece vaporization. The laser beam is first focused on the surface and then transferred to the surroundings by conduction. This results in forming a nugget that is shallow and wider heat-affected zone as compared to keyhole welding. Figure 4 illustrates a conduction mode welding.

The shape of the weld pool in a conduction mode welding is primarily determined by the flow in the weld pool and due to influence of surface active elements [3, 6].

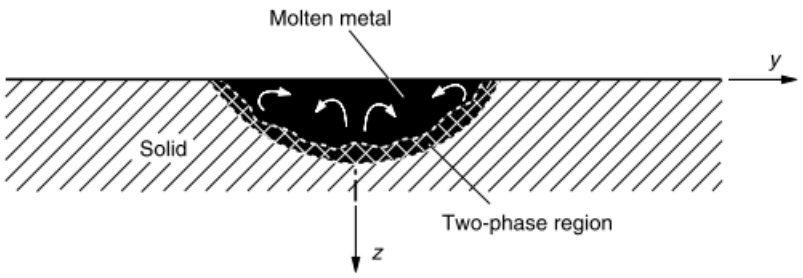

Figure 4: Schematic of Conduction Mode Welding [3]

b. Keyhole Mode Welding

This is characterized by deep narrow welds. A high power density of above 10^6 W/cm^2, the workpiece material is vaporized to form a cavity (*the keyhole)*, which is surrounded by molten metal, which in turn is surrounded by the solid material. The molten material fills the cavity which contains vapor, plasma (or both) as the laser beam progresses along the joint [6, 9, 10].

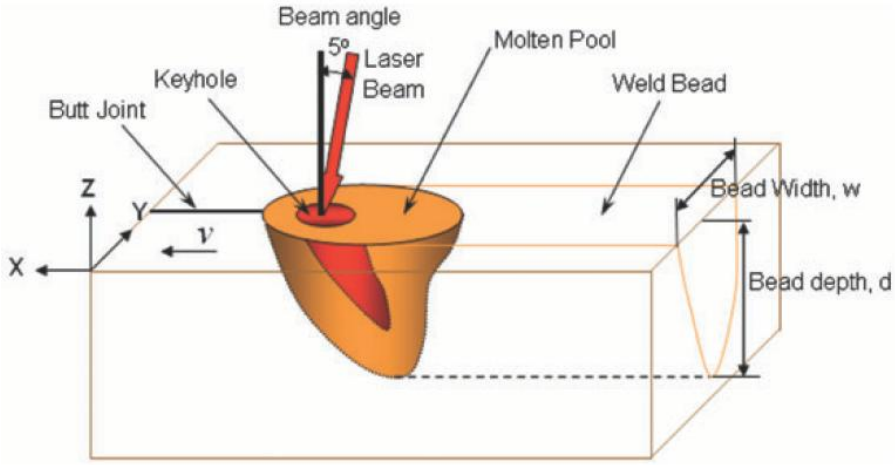

Figure 5: Schematic of the keyhole mode laser welding process: Illustration of bending of the keyhole in the direction of workpiece travel [10]

There are some forces that tend to collapse the keyhole cavity. These forces include the surface tension at the interface between the molten metal and the vapor or plasma, the hydrostatic pressure of the molten metal and the hydrodynamic pressure of the molten metal. They are however balanced by vapor pressure higher than the atmospheric pressure which exists within the cavity and ablation pressure of the material as it vaporizes from the inner surface of the keyhole and which reinforce the vapor pressure [9]. The keyhole is sustained by the balancing pressure.

About 70 – 90% of the laser energy formed at the keyhole is transferred deeper into the material which results in absorption and hence enable very narrow and deep penetration welds to be achieved. The high energy in laser welding coupled with minimal distortion makes laser keyhole welding entrancing for machined component and aerospace engine components. The keyhole shape is best represented with a vertical cylinder which is generally bent in the direction of the workpiece travel as shown in Fig 5.

1.2.7 Microstructural Defects in Laser Welding

Despite the aforementioned merits of laser welding, it has its shortcomings and challenges as it could cause undesirable defects that reduce the mechanical properties of the material and hence affect the reliability and performance of the material. The defects include coring or macro-segregation, solidification cracking and porosity:

a. Coring or Macro-segregation: In laser processing, the cooling rates are so high which makes achieving equilibrium during diffusion is difficult. This implies that the cooling and subsequent solidification are too fast that the solid formed do not have sufficient time to uniformly distribute the elements all around the solid. Hence there is a composition gradient across the solid formed. The variation in the composition across the solid is as a result of the segregation of impurities and alloying elements during the solidification process which consequently causes variation in the material properties across the fusion. This would cause a region within the fusion zone to have poor microstructural composition thereby affecting the region's mechanical properties adversely.

b. Porosity: This is the presence of gas pores within the fusion zone. It is also known as voids (or cavity) formed due to entrapment of gas during solidification process. It is formed by the absorption of gases into the melt and their subsequent escape during solidification as a result of limited solubility of the gas in the solid. Surface contamination such as oils, moisture and paints, and chemical reactions are major sources of gases in the molten metal[3].

c. Cracking: This is caused by the residual stresses resulting from the fusion zone contraction during cooling. If the crack occurs just after solidification process in the temperature range of about 200–300°C below the melting temperature it is referred to as hot cracking and cold cracking when the bead has cooled down to room temperature. Other forms of cracking that may occur include liquid cracking, lamellar cracking and reheat cracking. Cracks are the most devastating of all defects and also difficult to detect [3, 11].

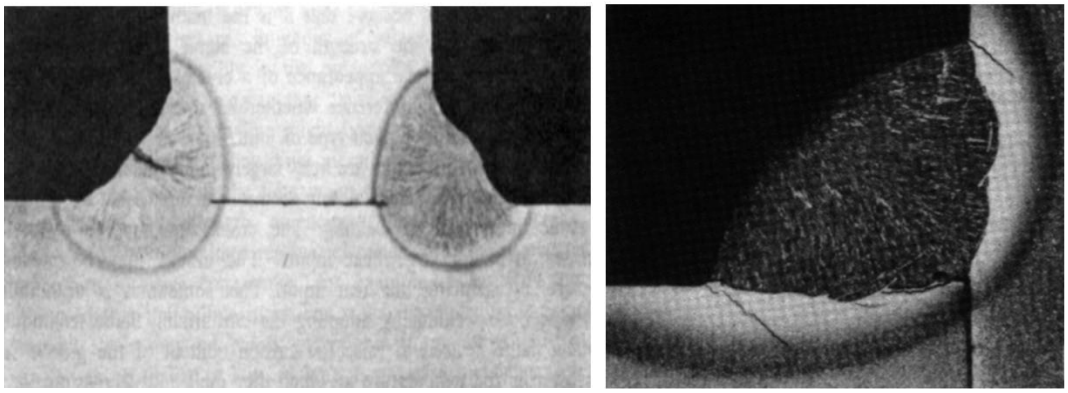

(a) (b)

Figure 6: Pictorial illustration of weld cracks. (a) Hot crack in a fillet weld. (b) Cold crack in the heat-affected zone of a fillet weld [3]

1.3 Natural Frequency

Recently, modal analysis has become a widespread means of finding the modes of vibration and the natural frequency of a structures and their subsequent use of these modal parameters for evaluating the structure's integrity. In every development of a new or improved mechanical product, structural dynamics testing on product prototypes is used to assess the real dynamic behavior. From the many non-destructive test now available, dynamic methods has grown in importance when compared to conventional diagnostic methods, like that based on visual inspection or ultrasonic analysis[12]. Many researchers have employed dynamic Non-Destructive Testing (NDT) to investigate the viability of structure system. The shift in the position of the natural frequency has been the key factor for evaluating the viability of structures. Welding process no doubt induces defects and residual stresses in the welded region and structure respectively. These eventually affect the flexural characteristics of the welded material. The presence of defects developed in a component changes its flexural characteristics, e.g. a reduction in the stiffness, increase in the damping and a reduction in the natural frequency[13]. This change in the natural frequency results from the changes in material properties of the structure during welding. During an experiment on the vibration of welded steel boxes it was

noticed that there were frequency changes of up to 20% for certain modes of a particular box when tested in the “as welded” condition and after stress relieving [14, 15].

The flexural motion of the system involves the to and fro oscillation between potential and kinetic energy. The system may also be subjected to energy dissipating or resistance source known as damping. Since the system is losing energy during the motion, free vibration will decrease and eventually become at rest. However the forced vibration can remain at the exciting frequency with requirement of energy to be supplied. The damping of the system also influences the natural frequency of system [16]. Vibration placed an important role in design and manufacturing as it may induce fatigue, wear and ultimate failure of the system. Therefore it thorough consideration in engineering practices.

1.4 The Research Motivation

Welds are often an essential part of engineering structures; therefore their contribution to the dynamic behavior cannot be neglected. Residual stresses and microstructural changes near the weld and in the welded regions due to the nonlinear thermal processes during welding, will most certainly influence the mechanical and hence the dynamic properties of the structure as a whole. Though extensive research that investigates the microstructural properties, temperature distribution and residual stresses of welded steels as a result of welding has been conducted, but little literatures exist about the study of the dependency of the mechanical and metallurgical properties on laser welding parameters of 316L ASS and the influence of the samples geometry on these properties.

In addition, the scarcity of work in understanding the effect of weld runs on the modal parameters of 316L steel blanks, despite their wide applications especially in petrochemical and

marine industries[11] is another motivation for this work. This study is aimed at filling this literature gap and investigates a new method for characterizing welded joints.

Modal analysis is employed in this study to characterized laser welded 316L steel blanks.

1.5 Objectives and Approach

1.5.1 Objectives

The main objectives of this research are to:

1. Characterize the flexural response of the welded samples
2. Characterize the microstructure and morphology of the welded section
3. Simulate mechanical response of the welded region through predicting the stress states

1.5.2 Approach

1. Conducting the modal analysis to capture the natural frequencies of the samples with the aid of data acquisition setup interfaced with LabVIEW software.

2. Enumerating numerically the natural frequencies of the unwelded samples for comparison with the modal analysis experimental results.

3. Characterizing the welded samples using the following techniques:- (a) Optical light microscopic (b) SEM (c) EDS (d) XRD (e) Micro-hardness indentation test.

4. Using the FEM ANSYS code to:

a. simulate the temperature distribution and residual stresses of laser welding of 316L Steel blanks

b. simulate the effect of the weld runs on modal parameters

CHAPTER TWO

2.0 LITERATURE REVIEW

The review of literatures in this research has been categorized into three sections based on the area of study that will be carried out. The first section of this chapter reviews modal testing for flexural analysis during laser welding while the second section presents the microstructural investigation of laser welded materials. The third section includes numerical study of laser welding and post-weld stress analysis.

2.1 Modal Testing for Flexural Analysis

Several authors have studied the effect of welding and heating on the modal parameters and flexural behavior of mechanical structures. In 1966, Dickinson observed that there was up to 20% changes in the frequency when a rectangular plate was welded [15] and Kaldas et al performed a theoretical and an experimental study of the effect of weld runs on the flexural characteristics of a rectangular plate[14]. They utilized finite difference method for the prediction of residual stresses in centrally welded plate to evaluate the induced in-plane stresses, including shear and both components of normal stress. The plates were of different configuration with respect to location of the weld: the central welds, the single edge weld and two parallel edge welds.

AlZaharnah investigated the flexural motion of a cantilever assembly heated at the fixed end and the effect of the size of heat affected zone (HAZ) in the flexural motion was simulated by correlating it with the frequency and amplitude of the motion employing the finite element method[17]. He assumed a temperature heat source with varying size at the fixed edge while an

impulsive load is applied at the cantilever free end. He found that because of the temperature field in the plate during heating which modifies the modulus of elasticity of the plate, the maximum amplitude difference increases with the size of the heat source. This increase is steep for a small heat source size and as the heat source increases it becomes gradual, though the thermal non-linearity was not included in this analysis. In another study the same author et al examined the flexural motion of a cantilever plate heated at the fixed end with a moving laser heat source[18]. The Finite Element software ANSYS was used to examined the effect of the moving laser heat source on the flexural characteristics by computing the displacement difference for heating and no-heating situations and the time shift between peaks while considering different heat source speeds. They simulated the moving laser heat source by dividing the total time for heating into equal time steps. Then all the nodes at the fixed end were fixed to the melting temperature of the plate for time duration equal to a single time step. Only the mechanical non-linearity was considered during the simulation process. They found out that due to increase in energy transfer time as a result of low heat source speed, the magnitude of displacement increases for low heat source speed and similarly reduce with increasing heat source speed. They also examined variation of amplitude of the flexural motion with the moving heat source speed and found that at low speed (1cm/sec) of the heating source, the amplitude remain high while it reduces as the speed increases to 3cm/sec. They observed that this behavior is affected by temperature distribution particularly in the near region of the moving heat source and that the flexural characteristics of the plate changes significantly once the large variation occurs in a narrow region next to the heat source as it speed increases.

In a separate study, AlZaharnah et al presented how the flexural wave characteristics at the free end during the welding of one end of a bar depends on the heating duration. The finite element

software ANSYS was used to compute the wave characteristic as a function of time[19]. The temperature of the heat source was maintained at the melting temperature of the bar material and with the temperature dependent elastic modulus, the process was simulated. It was found that temperature decays rapidly in the region next to the heated zone in the early period and gradually as the heating progresses. Also, by increasing temperature in the heated region of the bar lowers the modulus of elasticity and this becomes significant as the heating extend towards the free end of the bar with progressing heating period. The characteristics of flexural waves (amplitude and frequency) due to heating and no heating situations is almost the same at time 0.05s when the impulse force is applied, i.e. slight variation in amplitudes is observed for both flexural waves corresponding to heating and no heating conditions. The flexural wave amplitude is smaller for no-heating situation than that of heating situation due to the change in the modulus of elasticity with temperature. However, difference in amplitude of both waves is more pronounced for heating periods of 0.1s and 0.25s, this is because of the variation in modulus of elasticity, which results in change of flexural wave characteristics. It was as well found that sharp decay in the temperature in the region close to the heated zone results in sharp changes of the modulus of elasticity, hence the large difference in the maximum amplitude difference.

Investigation into the effect of heat source location on the flexural characteristics of a bar subjected to welding-liked process was carried out [20]. They adopted a temperature heat source along the width of the bar with temperature-dependent mechanical properties and constant heat source to predict the flexural characteristics using ANSYS finite element code. Their results show that temperature attains high values at the location of the heat source and decays steeply as the distance in the vicinity of the heat source increases along the x-axis with an evenly temperature gradient around the region consequent upon constant heat source. They considered

the displacement of the plate due to flexural motion while changing the location of the heat source along the axial distance with heating and no-heating situations. They found that the flexural displacement is maximum at the free end of the plate and with little difference for heating and no-heating cases. This difference diminishes where location of the heat source is moved two-third of the length. The effect of the heat source location on the plate deflection is obvious in that the amount of deflection changes as the heat source location along the x-axis of the plate changes and the maximum amplitude difference changes with the location of the heat source and reaches the maximum value for the heat source location at one-third of the length of the plate. Variation of the maximum amplitude difference was found to be associated to the change in elastic modulus as it reduces with increasing temperature. They concluded that the amplitude difference variation with heat source location is not in a simple form due to the variation non-linearity. Hyder et al used the finite element method to investigate the flexural motion consequent upon high magnitude of recoil pressure acting on the plate and the resulting stress field inside a cantilever plate during laser evaporative/non-conductive heating[21]. They also found that the magnitude of the displacement is highest at the free end and lowest at the fixed end due to the cantilever arrangement with a frequency oscillation and maximum displacement in the order of 0.2Hz and 20μm respectively. The equivalent stress resulting from the flexural motion reaches peak at about 2ms as a result of the large displacement from the excessive bending force acting normally at the free end of the plate. A decrease was observed in this stress towards the fixed end of plate owing to lesser bending force in this region. The inclusion of copper as a seventh element in the analysis gives a maximum stress difference in the order 800KPa while the frequency of the stress difference is almost twice the displacement, hence considerably influence of the workpiece stress field and frequency result due to addition of copper. The equivalent stress in the transverse direction is similar to that obtained in the axial

direction (along x-axis) except the initial peak. It was noted that the magnitude of equivalent stress in the transverse direction is less because of lower displacement in the transverse direction than its counterpart corresponding to axial direction.

Another study analyzed the thermal stresses developed in a substrate subjected to laser heating process and the flexural wave propagation due to axial stress component in the surface vicinity of the substrate [22]. Analysis of the wave behavior using Fast Fourier Transformation (FFT) showed that the displacement vector of each uniform element was transformed from time domain into frequency domain. Responses from the transformations were then solved using Finite Element Method (FEM) and an inverse FFT was used to recover the response. They found that the wave amplitude varies with time though no dominant pattern was observed because the initial wave form at the centre of the workpiece is modified as it travels along the workpiece due to: i. the dispersion effect of the workpiece material ii. overlapping of the wave modes, and iii. the reflected wave from the free ends of the workpiece that interfere with the traveling wave. They stated that amplitude of the traveling wave vanishes as it travels towards the free end of the workpiece though the wave appears at the free end as a high frequency mode. This is because the traveling wave has low amplitude in these location and reflected waves modify easily the travelling pattern. The stress normal component was shown to vary with time and it has two maxima, one is the heating cycle and the other is the cooling cycle, and it takes a value as high as 20MPa less than the yield stress of the workpiece material at the surface vicinity.

The stress field developed during the flexural motion of workpiece when ablated by a laser beam was considered by Yilbas et al[23]. Both the normal pressure force and the resulting amplitude and frequency of the flexural waves as well as the stress levels in the substrate material were computed using the finite element method (FEM). In the study, third element aluminum was

introduced to understand its influence on flexural properties while adopting two geometrical arrangements. The displacement of the surface at the central position of the workpiece was found to be higher for the cantilever case than for the case where both ends are freely supported due to the cantilever arrangement, in which case the workpiece moves freely from one end thereby enhancing the amplitude of the surface displacement. When both ends of the workpiece are simply supported, the amplitude of displacement dies out with time, resulting from the simply supported system; this forces the displacement to decay rapidly. They found out also that the additional element only influence the displacement difference at the early stage, while this difference decays with time for both cantilever and both-ends-supported arrangement. The equivalent stress (stress component) was also study; it was observed that it attain a high value in the early period and decreases to zero before reaching it second peak. The zero equivalent stress corresponds to when the workpiece straighten i.e. displacement decreases to zero. In a similar study, the authors carried out a 3D flexural wave analysis for a locally imbedded single aluminum cell in steel substrate, to study the effect of the location of this impurity element on the flexural wave motion of the substrate by varying its location[24]. The displacement was found for the sixth location to attain high value at certain periods provided that it reaches its peak value at about 3ms after the laser pulse ends. In the transverse direction, flexural motion does not change significantly due to lesser displacement in that direction. The time at which the highest values for displacement and displacement difference occur does not coincide since the displacement difference reaches its peak at about 4ms after the pulse ends. After observing the flexural behavior of seven different locations for the third element, they concluded that the displacement difference is influenced significantly by the axial locations of the additional element and that this behavior reduces as the additional element location moves close to the free end.

Laser induced flexural wave propagation due to recoil pressure at the vapor-liquid interface of the evaporated surface was investigated by analytically formulating the temperature rise during heating in [25]. Both ends free-supported, both ends fixed and cantilever workpiece configurations were considered. The researchers realized that flexural wave characteristics change noticeably as the configuration varies. Damping was high i.e. flexural wave dies rapidly when both ends were fixed and except for the cantilever configuration the amplitude decreases considerably close to the workpiece ends.

2.2 Material Characterization of Laser Welding

The metallurgical studies of laser welded materials received lots of research interest over the past years. The research in his field investigated mainly the microstructural properties for different material after exposure to laser beam during welding.

Mai et al researched the laser welding of dissimilar metals without filler materials using a pulse Nd:YAG laser with 30W power[26]. They investigated material interaction during melting, microstructure, defects, hardness and the residual stresses at the weld zone. They stated that in laser welding where no filler materials are used the problem of intermetallic phases formation (during fusion of metals) which are often hard and brittle are abated for due to high cooling and solidification rates. They performed an EDX element analysis with FE-SEM instrument for point counting and line-scan intensity elemental profile to determine the dilution rate and the size of the weld pool. Also X-ray imaging was used to study the joint porosity and morphology. When the porosity of the weld was examined, it showed that an increase in the welding speed decreases the pores while increasing the pores' average size. Pearlite and martensite fine grain structures were as well observed in the weld pool due to high cooling rates. On conduction of the pool hardness test, there was a sharp increase in hardness when compared to base material in the

different welds and also the residual stresses at the weld pool increases in all situations to the tone of its yield strength at the center in the case of steel-kovar weld.

In a related research, the authors presented an investigation of the intermetallic compound (IMC) layers formed in a defocused laser beam welded low carbon steel and aluminum alloy in a lap joint[27]. X-ray diffraction analysis and Transmission electron microscope with EDX analyzer (TEM-EDX) were used for the characterization of the IMC layer, the use of TEM-EDX was due to the thin IMC layer compared to the beam diameter. They found that the IMC layer at the weld lack a band-like morphology and that higher percentage of the IMC layer is mainly Al_5Fe_2 at the central region while $Al_{13}Fe_4$ was observed at the interface. Also the interface between IMC layer and the solidified A6111 was found to have average grains size of about 500 nm and an ultra fine grain size at the SPCC interface while at the central region of the layer grain size reaches 1mm. Some authors had previously investigated the tensile strength of the lap joint using an Instron-type tester under a cross-head speed of $1.7x10^{-5}ms^{-1}$ at room temperature and the relationship between the morphology of the IMC and the joint strength[28].

Yao et al developed a new method for the laser welding of copper and low carbon steel by controlling the dilution ratio of Cu to be lower than 7.2 wt% to solve the problems of material mismatches inherent in welding these dissimilar metals, the dilution ration of Cu was controlled by carefully monitoring the laser beam interaction with Cu plate[29]. Optical microscopy (OM) was used to study the weld morphology while the elemental distribution at microstructural level of the interface were characterized by using scanning electron microscopy (SEM) with an embedded energy dispersive spectroscopy (EDS). They found that the joint was defect-free and hence had good strength due to limited amount of copper that dissolved in the steel. Also the microstructural analyses of the interface shows a transition zone having huge amount of gradual

phases at upper part of the copper interface. Taban et al studied the joints achieved by laser welding of chromium modified stainless steel by observing the microstructural and mechanical properties of the joint, as well the impact toughness, fatigue and corrosion resistance of the joint[30]. They found out that in all, the joints were defects-free and that the fatigue strength was similar to that of the base material. The only set-back observed was the stainless steel tendency to grain coarsening at high temperature heat affected zone though without any deleterious effect on the strength but properties like impact toughness that depends on the grain size number might be affected negatively. They additionally observed that better welds can be achieved if the grain coarsening could be restricted to ASTM grain size numbers of 6 or higher. They also found that the weld shows promising resistance to environmental corrosion.

In a related research by Kell et al, they carried out the microstructural characterization of laser welded 316L stainless steel. By combining electron backscatter diffraction (EBSD) and energy dispersion spectroscopic (EDS), they studied different phases formed on solidification as a consequence of varying welding procedures[4]. With the use of EBSD and EDS they found out that during solidification process, the welds have larger grains (approx. 200μm) than the grains of base metal (approx. 20μm). Similar grain size of (approx. 200μm) is still noticed when uniform irradiance distribution method were used which was provided by a diffractive optical element, though with little regions of δ-ferrite. An investigation was carried out to evaluate microstructural change after laser welding and its consequent effect on the tensile and fatigue properties of steel (type: DP600 steel) with more attention on the failure mechanism [31]. They determined that the formation of large amount of martensitic structure was responsible for the hardness; this martensitic structure was attributed to rapid cooling. There also exists a soft zone within HAZ causing reduction in ductility, this soft zone was due to the tempering of the pre-

existing martensite in the DP600 steel. They observed no considerable changes in the ultimate tensile strength after welding though with higher yield strength. Regarding the fatigue limit and the fatigue ratio of the joints, they were lesser than that of the base material though it shows higher fatigue life at large stress amplitudes which were comparable to base metal in spite of the soft zone.

Studies were carried out by Liu et al to investigate the laser welding of K418 and 42CrMo steels [2, 32, 33]. They characterized the microstructure of the phases present in the seam zone using X-ray diffraction (XRD) analysis, scanning electron microscope (SEM), transmission electron microscope (TEM) and energy-dispersive spectrometer (EDS). TEM was specifically used for structural analysis to overcome the difficulties of strong reflections of these phases being superimposed on one another and the very complex nature of the heavily alloyed laves phase. Results showed that the weld had non-equilibrium solidified microstructures consisting of mainly γ-FeCrNiC austenite solid solution dendrites as the matrix and (Nb, Ti) C type MC carbides, some fine and dispersed Ni_3Al (γ') phase and laves particles together with little amount of particle-like carbides distributed in the welded seam. Yilbas et al carried out a study to investigate the mechanical and metallurgical properties of electron beam welded austenitic 321 stainless steel. Analysis of the first and second law of thermodynamics of the welding process was carried out. It was found that the heat-affected zone increased as the work piece thickness increased and micro cracks were present at the fusion [34].

2.3 Numerical Study of Laser Welding

Several authors had investigated numerically the laser welding process. Among the research are the numerical studies of the heating process of a gas-assisted laser heating by Shuja et al[35]. In their study, they assumed a moving workpiece while the source of heat was fixed. They observed

that the movement of the workpiece is related to the temperature distribution inside the workpiece, as its speed increases the temperature contour becomes more non-uniform unlike at lower workpiece speed where the temperature extend further inside the substrate. They also found that during the cooling cycle, the rise and the decay of the surface temperature becomes rapid at low workpiece speed and vice visa. This is due to the fact that the workpiece movement enhances the heat conduction in the direction of motion and the convective cooling increases in the direction of motion because of no-slip condition generated at the workpiece surface due to the workpiece motion. A numerical analysis was performed to study residual stresses of a butt-weld of two plates using ABAQUS and ANSYS software packages [36]. In order to increase the accuracy and efficiency of the welding process analysis, a shell/3D modeling capability were adopted using the sequential thermal-stress solution procedure. Solid elements were used close to the weld where the temperature gradient are high while shell element were used for areas of less prominent temperature gradient further from the welding area. Mechanical and thermal non-linearities were incorporated in the model. It was observed that combination of the three-dimensional and the shell model could be applied very efficiently for a detailed study of welding processes. They therefore conclude that this modeling technique which involves the transition from the shell model to the 3D model discretization with a finer mesh of elements is very efficient for this purpose, in which case show no significant deviation when the residual stress in the weld were modeled with the full 3D elements in both packages. Also it was found that the temperature field in ANSYS model gives a slightly higher value in the root of the weld which quickly disappears by moving towards the plate ends.

The electron beam welding process was numerically simulated using the finite element method[37]. The authors analyzed the thermal field generated by the process, determined the

heat-affected zone and the residual stresses in the joint. They modeled the heat source using the disk heat source and a hemi-spherical heat source which assume the symmetry of the weld pool with respect to the axis going through the middle of the heat source. They found that the temperature gradient in the area corresponding to heat source causes increase of effective thermal stresses and that the maximum value of the stresses occur beneath the area of the heat source and depend on the yield stress of the welded material at given temperature. Turaa et al conducted the numerical simulation of the thermal and stress fields during the laser welding of a stainless CrNi steel type AISI 304 using a pulsed Nd: YAG laser[38]. A 3-dimensional finite-element model employed in ANSYS program was used for simulating the welding while the heat source was parameterized by the combination of a circular disk source with a Gaussian distribution of thermal flux with center on the top surface and a line source through the thickness of workpiece. They found that for the weld pool formation 23.4 % power transferred from the total laser beam power is needed.

Kazemi and Goldak developed a very simple 3-dimensional finite element method model for laser full penetration welding[39]. The heat source was modeled in relation to the time stepping such that when the heat source moves to the next load step, the former load step is deleted. After the first load step, the heat source moves forward to the next position in a distance equal to the element length. They showed that the heat source model developed can predict the weld cross section in deep penetration laser welding, especially in the case of full penetration welding, though with certain limitation of failing to predict the weld width in depth near the top surface. Also noted that the most sensitive parameters to the model in predicting weld shape are Peclet number, the conductivity of material and absorption coefficient of material used for the circular disk source. Osamah performed numerical heat transfer analysis during a laser spot welding

process aimed at using the double ellipsoidal representation of the laser beam, thereby including volumetric heat input from a heat source[40]. He considered temperature dependence of the material properties, phase change phenomena, and convective and radiative heat losses from all the surfaces of a sheet during the welding process. The FEM software ANSYS 10.0 was utilized. He realized that the temperature gradients during laser welding are usually very large and a very high temperature at the center of the workpiece was observed. Also, that the thermal residual stresses around the laser spot due to plastic strains were very small and localized within 1.0 mm range.

Andrea et al investigated the numerical procedure for the thermal and mechanical simulation of the welding process using a 3D FEM model in ANSYS[41]. In this report a non-uniform gap is considered for laser and TIG welding of INCONEL 625 and AISI 316 respectively. Temperature dependent material properties, radiation and convention effects were considered and the birth and death procedure were used. They performed during the thermal simulation a sensitivity analysis of the parameters and found that the welding speed is one of the most important parameters. The mesh size seems to have a minor effect and to ensure that same maximum temperature is attained for all welding process a good analysis of the power becomes important.

Literatures on numerical studies of the flexural analysis of a laser welded steel considering the post-weld effects like residual stresses and possible defects within the weld zone are not well developed. Few works were found in this area. Some works on the modeling of the flexural analysis of an unwelded sample were done to show that the problem of the deflections of a cantilever beam in both the case of large and small deflections can be handled using simple, easy-to-assemble and low-cost experiment, a study was performed to analyzed these deflections using a simple physical system [42, 43]. They initially obtained the differential equation

governing the deflection curve for large deflection along with the Cartesian coordinate's equation that depicts each point on the elastic. They considered the geometrical nonlinearity of the beam by numerically and experimentally analyzed the large deflections of the cantilever beam. The beam has a linear elastic material property, under the action of perpendicular tip load at the free end and a uniformly distributed load of its own weight along its length. While the large deflections of the cantilever beam were simulated using the ANSYS program, they compared the experimentally measured elastic curves with the numerically calculated ones, and found that they were satisfactorily in agreement.

From the review, most of the research work (both experimental and numerical) presented in the open literature have been focused on the parametric study of laser welding process, and some of them have been directed to flexural analysis during the welding and heating processes while the remaining concentrated on effect of welding parameters and weld runs on the modal parameters. The study of the effect of welding parameters and weld runs on the modal parameters is less researched into and further investigation in this area will improve the non-destructive testing techniques. Hence, this study has been carried out to examine the post-weld modal analysis and the subsequent characterization of the welded joint properties using the modal parameter - the natural frequency. This work contributes to fill the research gap and also enhances understanding of the effects of welding parameters and geometric configurations on the microstructural and mechanical properties of autogenous laser welded 316L austenitic stainless steel.

CHAPTER THREE

3.0 EXPERIMENTATION AND METHODOLOGY

In this section, the experimental procedure and approach of the study is presented.

The following sections outline the laser welding process, modal testing for flexural analysis and the characterization of the samples conducted in this study.

3.1 Laser Welding Experimental Setup and Welding Parameters

The CO_2 laser (LC-ALPHAIII) delivering nominal output power of 2kW at pulse mode with different frequencies is used to irradiate the workpiece surface. The nominal focal length of the focusing lens is 127mm. Argon assisting gas emerging from the conical nozzle and co-axially with the laser beam is used. The welding conditions are given in Table 1.

Several commercial 316L austenitic stainless steel (ASS) blanks were laser welded with different geometrical and welding parameters. Table 2 shows the chemical composition of 316L steel. Rectangular machined surface samples were prepared with dimension **40*mm*** × **22*mm*** × ***thickness mm*** and butt jointed autogenously using a carbon dioxide laser with the continuous wave mode. Figure 7 shows some of the laser welded samples. It should be mentioned that these samples were welded without filler material.

Table 1: Laser Welding Conditions

Laser Power [W]	Scanning Speed(mm/min)	Nozzle Gap[mm]	Nozzle Dia. [mm]	Focus Setting[mm]	Focus Dia. [mm]	Argon Pressure[KPa]
2000 – 4000	100 – 400	1.5	1.5	127	0.8	600

Table 2: 316L Steel chemical composition

Element	C	Mg	P	S	Si	Cr	Ni	Mo	N	Fe
Composition (wt%)	0.03	2.00	0.045	0.03	0.75	16.00	10.00	2.00	0.10	Balance

The welding parameters considered in this study are the feed rate (or welding speed) and the welding power while thickness of the blanks were varied. Other laser welding parameters not stated here were kept constant throughout the welding process. Tables 3 – 6 respectively illustrate the parametric variation for the feed rate, laser welding power and thickness of the blanks.

Table 3: Samples with varied beam feed rate only

Sample #	Thickness	Power (W)	Feed(mm/min)
10	1.5	3000	200
11	1.5	3000	300
12	1.5	3000	400

Table 4: Samples with varied beam feed rate only at higher power

Sample #	Thickness	Power (W)	Feed(mm/min)
142	2.5	4000	200
143	2.5	4000	300
144	2.5	4000	400

Table 5: Samples with varied power only

Sample #	Thickness	Power (W)	Feed(mm/min)
8	1.5	2000	400
12	1.5	3000	400
16	1.5	4000	400

Table 6: Samples with varied geometry only

Sample #	Thickness	Power (W)	Feed(mm/min)
Set A			
12	1.5	3000	400
76	2	3000	400
140	2.5	3000	400
Set B			
15	1.5	4000	300
143	2.5	4000	300
207	3	4000	300

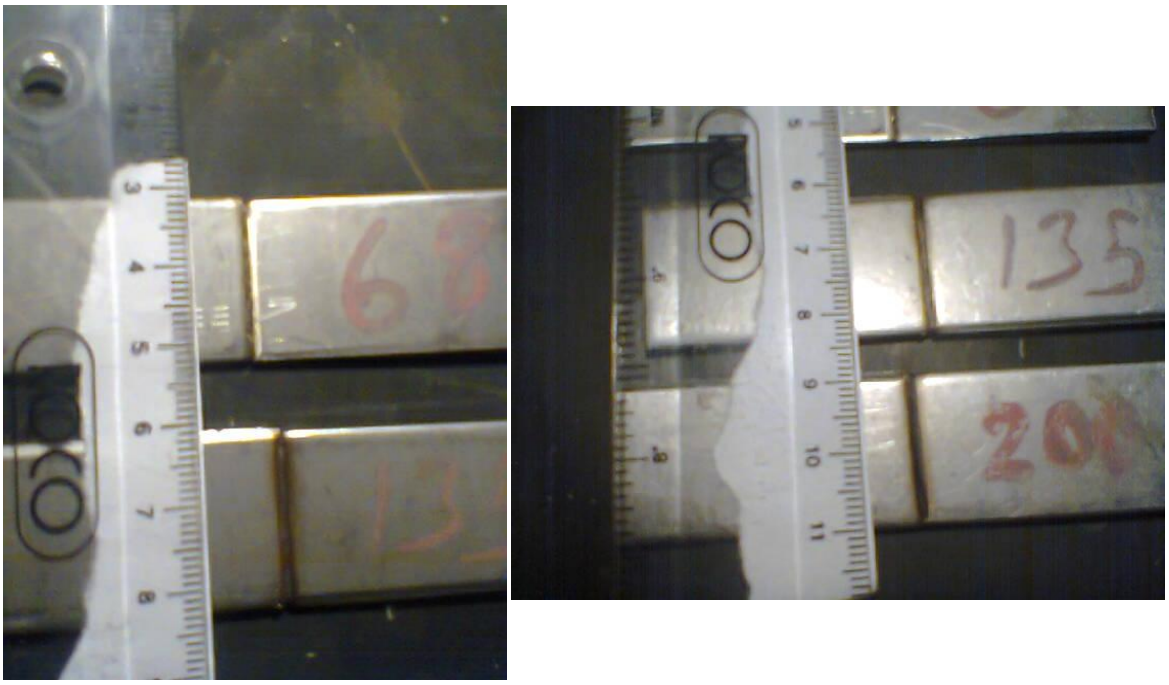

Figure 7: Laser Welded Samples of 316L steel plates

3.2 Modal Testing for Flexural Analysis

In order to investigate the flexural behavior of the welded 316l blanks, a first order modal analysis was carried out to determine modal parameters like natural frequency and stiffness. This section presents the mathematical formulations governing the analysis.

3.2.1 Theoretical Modal Analysis

The analysis of the response of a vibrational system relies on constructing a mathematical model or an equation of motion in order to calculate natural frequencies and mode shapes [16]. The vibration is characterized by amplitude, speed, acceleration and frequency spectrum. The measures which characterize the movement (vibration) of the system that is the displacement (*d*), speed (*v*) and acceleration (*a*) can be defined. Figure 8 shows schematics diagram of laser welded plates and the coordinate system. The acceleration of a bar resembling the plate can be written as [44]:

$$d = Dsin\omega t \tag{1}$$

$$v = dd/dt = D\omega cos\omega t \tag{2}$$

$$a = \frac{dv}{dt} = \frac{d^2d}{dt^2} = D\omega^2 sin\omega t \tag{3}$$

where D is the amplitude, ω is the angular velocity and *t* is the time.

A cantilever beam can be considered as two-dimensional, since it has a uniformly distributed mass and stiffness across the length of the beam with finite thickness, which is significantly less than its breadth and length. When the beam is subjected to a free flexural motion the geometry equation can be expressed as [20]:

$$\frac{d^4z}{dx^4} - \left(\frac{{\omega_{nf}}^2 m}{EI}\right) y = 0 \quad (4)$$

where ω_{nf} represents the natural frequency values. *E* is the modulus of elasticity of the plate material, *I* is the moment of inertia, *m* is the mass per unit length of the plates and *x*, *y*, *z* are the distances in the *x*, y, z coordinates system (Figure 8). The general solution of the differential equation presented in Eqn. (4) and describing the flexural motion of a blank without welding can be written as [20]:

$$z = Acosh\left[\left(\frac{m{\omega_{nf}}^2}{EI}\right)^{1/4} x\right] + Bsinh\left[\left(\frac{m{\omega_{nf}}^2}{EI}\right)^{1/4} x\right] + Ccos\left[\left(\frac{m{\omega_{nf}}^2}{EI}\right)^{1/4} x\right] + Dsin\left[\left(\frac{m{\omega_{nf}}^2}{EI}\right)^{1/4} x\right] \quad (5)$$

where A, B, C, and D are the integration constants and can be found after substituting the following boundary conditions in equation (5). The boundary conditions can be expressed as:

At the clamped end of the uniform bar where x = 0:

$$y|_{x=0} = 0 \; and \; \frac{dy(x)}{dx}|_{x=0} = 0 \quad (5a)$$

And at the free end where $x = l$:

$$\frac{d^2y(x)}{dx^2}|_{x=l} = 0 \; and \; \frac{d^3y(x)}{dx^3}|_{x=l} = 0 \quad (5b)$$

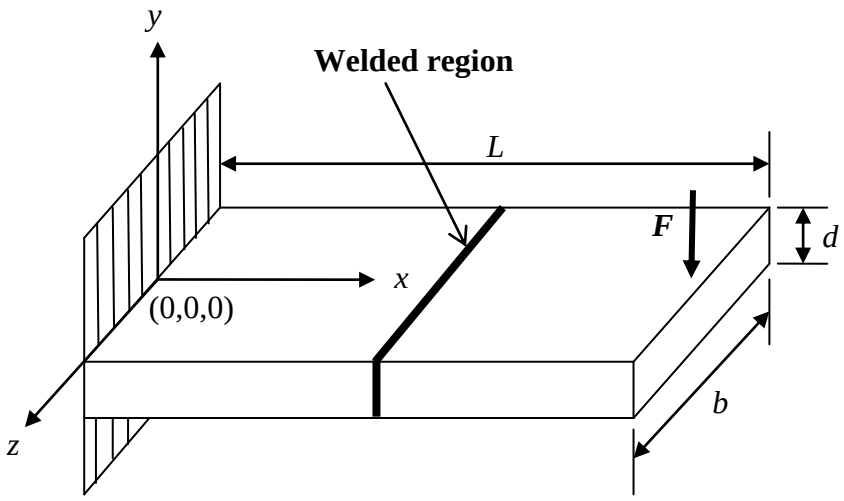

Figure 8: Schematic diagram of the cantilever configuration of a plate

Therefore equation (5) reduces to

$$cosh\left[\left(\frac{m\omega^2}{EI}\right)^{1/4} l\right] cos\left[\left(\frac{m\omega^2}{EI}\right)^{1/4} l\right] + 1 = 0 \qquad (6)$$

According to previous studies [45, 46], the resulting fundamental natural frequency corresponding to the first mode of motion for the uniform blank is

$$\omega_{\boldsymbol{nf}} = 1.875^{\mathbf{2}}\sqrt{\frac{EI}{ml^4}} \qquad (7)$$

The flexural properties of a cantilever beam are shown in the Figure 8. The damped natural frequency is calculated according to the well known formula [47, 48]:

$$\omega_d = \omega_{nf}\sqrt{1-\xi^2} \qquad (8)$$

where $\boldsymbol{\xi}$ is the damping coefficient of the uniform blank.

From eqn. (7), natural frequency of the first mode in radian is given by [45]:

$$\omega_{\boldsymbol{nf}} = 1.875^{\mathbf{2}}\sqrt{\frac{EI}{mL^4}} \tag{9}$$

In this case of equation (9), $m = \rho bLd$ (10)

Where *b* is the breadth, *d* is the width (thickness) and *L* is the length of the blanks

For rectangular blanks the moment of inertial *I* is given by [49]:

$$I = \frac{bd^3}{12} \tag{11}$$

The circular natural frequency in hertz is related by [47, 48]:

$$f_n = \frac{\omega_{nf}}{2\pi} \tag{12}$$

The natural frequency, ω_{nf} of undamped system is related to the stiffness, K of the system by [48]:

$$\omega_{nf} = \sqrt{\frac{K}{m}} \tag{13}$$

However the above frequency has to be modified since there is a mass in the form of an accelerometer at the free end of the continuous blanks. By continuous approach the solution is difficult since with tip mass the boundary condition at free end is now time dependent. A simpler approach will be to include the accelerometer mass in the total mass of the blank. A procedure for the calculating the first mode natural frequency by considering the total mass is illustrated

below. With the total mass, $M_1(kg)$, the natural frequency could be measured as accurate as possible.

Considering the blank as a mass-less specimen with stiffness *K* and a discrete effective (concentrated) mass, m_{ef} (kg/m) at the free end, this produces the same frequency as a continuous blank specimen without any tip mass. Hence, the natural frequency of discrete model of the blank without an accelerometer can be written as:

$$\omega_{nf1} = \sqrt{\frac{K}{m_{ef1}}} \tag{14}$$

Where the stiffness of the cantilever beam at it end is $K = \frac{3\mathrm{EI}}{\mathrm{L}^3}$ [47, 50] (15)

From which the effective mass m_{eff1} at tip can be written by combining eqns. (14) and (15) as:

$$m_{ef1} = \frac{3EI}{\omega_{nf1}{}^2\mathrm{L}^3} \tag{16}$$

Comparing eqn. (9) with eqn. (14), then the effective mass becomes:

$$m_{ef1} = \frac{3EI}{L^3}\frac{L^3 m}{1.875^4 EI} = \frac{33}{140}m \tag{17}$$

Therefore, the effective mass at the tip of the blank is about 0.236 times the mass per unit length of the blank.

So, considering the mass of accelerometer, m_a, at the free end of the blank, the total mass at free end will be:

$$M_1 = m_{ef1} + m_a \tag{18}$$

Hence, for the discrete blank with accelerometer, the theoretical fundamental natural frequency considering the mass of accelerometer will be:

$$\omega_{nf1} = \sqrt{\frac{K}{M_1}} \tag{19}$$

3.2.2 Experimental Modal Analysis

The Components of the System Used For Data Acquisition and Data Processing

A. Data Acquisition Board NI 9234

NI 9234 is 4-channel dynamic signal acquisition (DSA) modules for making high-accuracy measurements from IEPE sensors (Figure 9). This C Series analog input module delivers 102dB of dynamic range and incorporate IEPE (2mA constant current) signal conditioning for accelerometers and microphones. The four input channels simultaneously acquire at rates from 2 to 50 kHz or, with the NI 9234, up to 51.2 kS/s. In addition, the modules include built-in antialiasing filters that automatically adjust to your sampling rate. NI 9233/9234 modules are ideal for a wide variety of mobile/portable applications such as industrial machine condition monitoring and in-vehicle noise, vibration, and harshness testing. NI 9234 module use a method of A/D conversion known as delta-sigma modulation. If, for example, the data rate is 25 kS/s, then each ADC actually samples its input signal at 3.2 MS/s (128 times the data rate) and produces samples that are applied to a digital filter. This filter then expands the data to 24 bits, rejects signal components greater than 12.5 kHz (the Nyquist frequency), and digitally re-samples the data at the chosen data rate of 25kS/s. This combination of analog and digital filtering provides an accurate representation of desirable signals while rejecting out-of-

band signals. The built-in antialiasing filters automatically adjust themselves to discriminate between signals based on the frequency range, or bandwidth, of the signal.

B. Brüel & Kjær Impact Hammer —Type 8206

Type 8206 B & K impact hammer (Figure 10) has been designed to excite and measure impact forces on small to medium structures such as engine blocks, car frames and automotive components. An accelerometer (or laser velocity transducer) is used to measure the response of the structure.

Figure 9: NI 9234 Data Acquisition Board

Figure 10: B & K Impact Hammer —Type 8206

By using a multichannel fast fourier transformation (FFT) analyzer, such as the PULSE™ system, the frequency response function and mode shapes of the test structure can then be derived. Contrary to using an electrodynamic exciter, an impact hammer does not apply additional mass loading to the test object and it provides a very portable solution for excitation. The output sensitivity is expressed in terms of voltage per unit force (mV/N or mV/lbf). The hammer also has built-in acceleration compensation that removes unwanted noise from the resonance of the hammer from the output signal. This results in a clean, smooth output signal representing the excitation in both amplitude and phase.

C. B & K Accelerometer Type- 4371

The piezoelectric accelerometer (Figure 11) converts the acceleration into an electric measure which is proportional with the force applied on the internal ceramic element (piezoelectric), the mechanic variable (acceleration) being obtained by a measurement of the force[44].

The assembly is composed of a central shaft, a ceramic piezoelectric element, a seismic body and a pre-load arrow. During operation, the unit sends a perpendicular movement

towards the basis. When the accelerometer is attached to a vibrant structure, the seismic mass exacts a force on the ceramic piezoelectric element. This applied force determines the piezoelectric material to produce an electric measure. The force is equal to the mass multiplied by acceleration (Newton's second law: $F = m*a$), the result obtained is proportional to the acceleration as long as the mass m is constant[44].

D. B & K Charge Amplifier - Type 2635

Charge Amplifier Type 2635 (Figure 12) is a comprehensively equipped charge conditioning amplifier. The output can be routed to portable tape recorders and level recorders, electronic voltmeters, measuring amplifiers and frequency analyzers. It can be powered from internal batteries or an external DC power supply, making it useful both in the field and in the laboratory. Other features of this amplifier are charge input, digit conditioning to transducer sensitivity, unified output ratings for simplified system calibration, high sensitivity up to 10V/pC, built-in integrators for displacement and velocity among others.

Figure 11: B & K Accelerometer Type- 4371

Figure 12: Charge Amplifier - Type 2635

E. Computer System

The laptop PC with the configuration below is used as an interface where the other devices are linked to the labview software installed on the PC.

Brand: DELL, Inspiron N4030

CPU : Intel® Core™ i5 M480 @ 2.67GHz 2.66GHz

RAM : 3.00GB (2.87 GB usable)

Weight: 2.1-2.5 kg

Screen Size: 14-14.5 in

F. Labview Software

In the processing of the acquired data through the medium of the acquisition board of the SCXI 1600 module the LabView development medium is used through which the used module is controlled with the help of the NI-DAQmx[44]. The use of DAQ Assistant can simplify the development of the application. National Instruments recommends the creation of the tasks through the medium of DAQ Assistant at the use of sensors (paper cited in [44]). In Figure 13, the block diagram of the virtual instrument

achieved for the proper acquisition of data is presented. The acquired data are written in a text file from which later they are read in order to be processed.

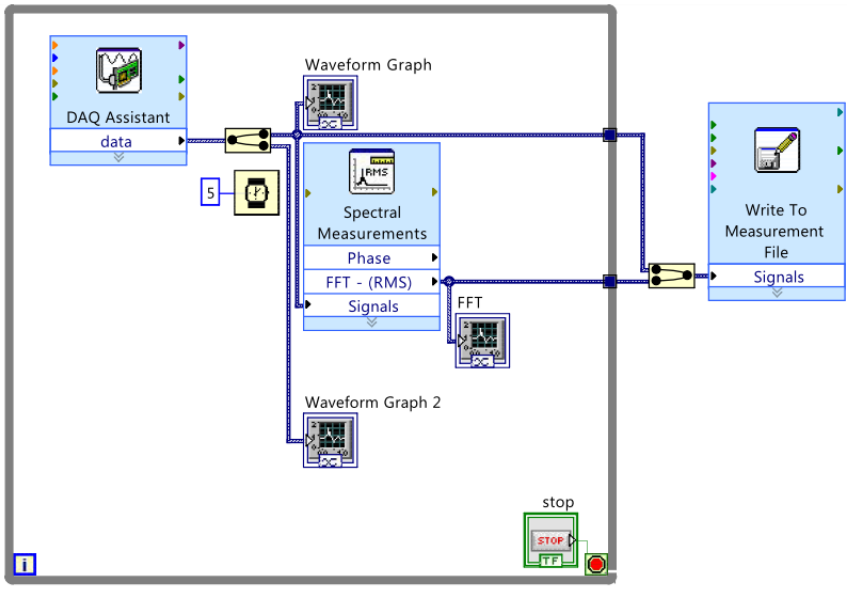

Figure 13: The block diagram of the virtual instrument achieved for data acquisition

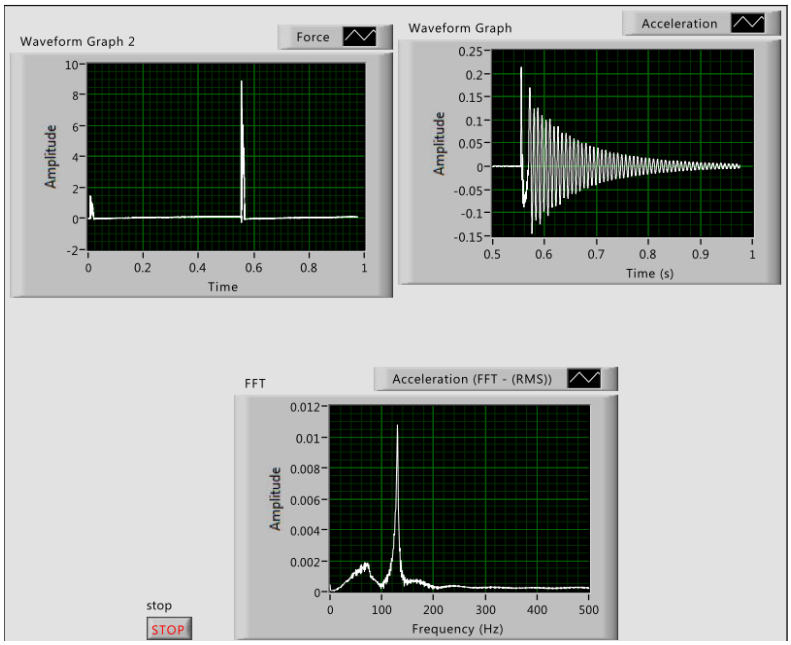

Figure 14: Window of Labview software with three different plot displays

The front panel of Labview software with three different plot displays is shown in Figure 14. The input force (N) and output acceleration (in/sec 2) responses are shown on the top row of the main display. The frequency response function is shown on the bottom row of the main display. The frequency response function represents the ratio of output over input signals. The frequency response is a function of frequency and reaches its maximum value at natural frequency.

To obtain the natural frequency of the cantilever plate experimentally, a setup, as shown in the schematics in Figure 15, is used. The impact hammer (Brüel & Kjær Impact Hammer —Type 8206) was used to set the sample into flexural motion. The accelerometer (B & K Accelerometer Type- 4371) attached to the sample relays this flexural signal of the sample (due the impact) to the DAQ (Data Acquisition Board NI 9234) system which converts this analog signal to digital based signal. The signal from accelerometer was amplified by a charge amplifier (B & K Charge Amplifier - Type 2635) to increase the signal to noise ratio before reaching the DAQ. The DAQ's combination of analog and digital filtering provides an accurate representation of desirable signals. The filtered digital data are then transfer to the LabView software for further processing. The interfaced system (DAQ and virtual instruments – VIs) allows real time monitoring of the signals from the experimental setup. The time history (Displacement-Time), and Fast Fourier Transformation (FFT) plots of the data can be programmed in Labview software. The natural frequencies of the system were obtained directly by observing the FFT plot. The location of peak corresponds to the natural frequencies of the system.

The data acquisition system includes a data acquisition box (DAQ) and a host computer which displays the data in real-time and provides a graphical-user interface (Labview software).

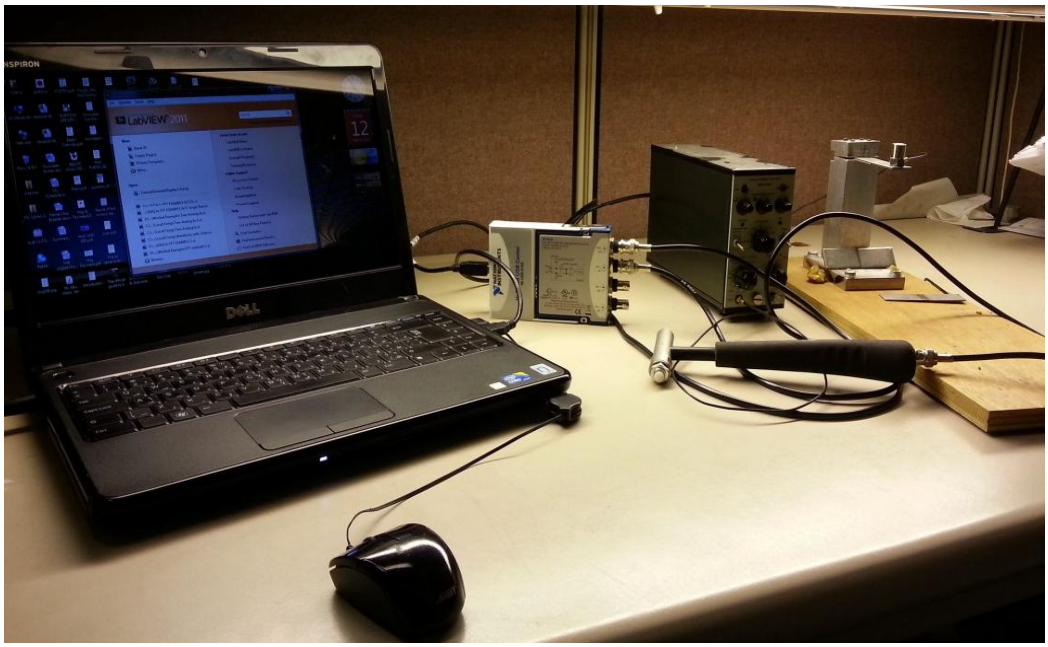

Figure 15: Modal Analysis experimental set-up

3.3 Material Characterization

After welding, the samples were visually inspected then sectioned across the width parallel to welding direction to reduce the sample into a square like sample to ease further preparation for material characterization and mechanical testing.

3.3.1 Sample Preparation

These samples (square-like) were again sectioned transversely i.e perpendicular to the welding direction resulting into two parts labeled X and Y for each sample. All samples (X of each sample only) were then hot-mounted using Buehler transoptic powder (polymer) in a mounting machine (Evolution, IPA 40 Remet, Bologna, Italy) at temperature of 200^0C for about 35min including cooling time, to enable handling during grinding and polishing. The samples were then grinded using Buehler roll grinder (Handimet 2 Roll Grinder Buehler, Japan) with 240, 320, 400 and 600 grits and polished on Buehler grinding and polishing table until a mirror-like plane

surface is achieved. The samples were sonicated for 10min then etched with aqua regia solution (ratio HCL to HNO_3 = 3 to 1) for 3 to 4 minutes for microstructural micrograph imaging. Metallurgical optical microscope (MEIJI Techno MX7100, USA) was utilized to observe the shape and microstructure of the fusion zone. FIB-FESEM (LYRA3XM, Tescan, Germany) was also used to substantiate the images from optical microscope and to better understand the solidification nature and resulting microstructure during cooling across the heat affected and fusion zones. The Y section of each samples were prepared for X-Ray Diffraction (XRD).

A XRD D8 Advance (XRD D8Advance Bruker AXS, Germany) machine was used to reveal the interaction between the compositional elements of the material during welding and the resulting compound(s) formed at the fusion zone. For mechanical characterization, MMT-3 Digital Microhardness Tester, Buehler (Lake Bluff, Illinois, USA) was used for the hardness scan across the welded region including the heat affected zone. Figure 16 – 20 shows the machines employed for the preparation, testing and characterization of the welded samples.

Figure 16: IPA 40 Remet Mounting Machine

Figure 17: Vickers Microharness Tester

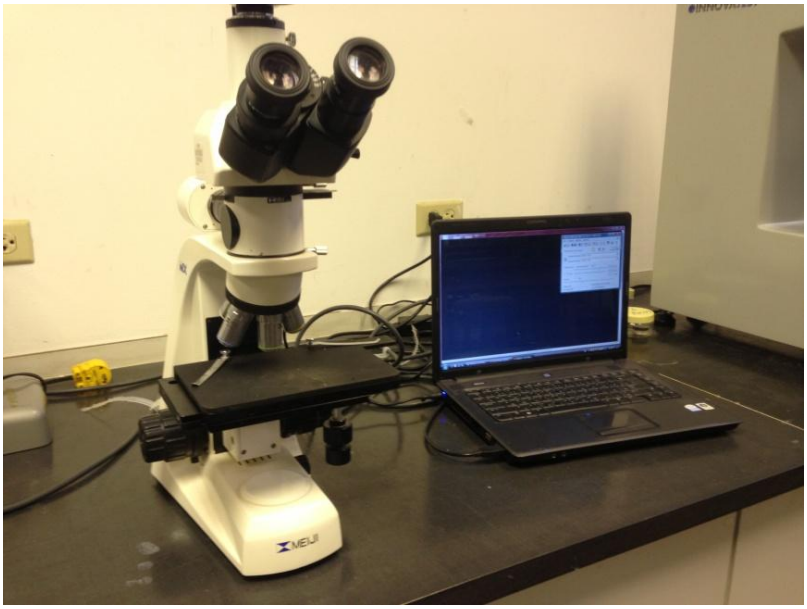

Figure 18: Metallurgical optical microscope used for optical micrograph

Figure 19: LYRA3 XM FIB-FESEM used for the Characterization

Figure 20: XRD D8 Advance

CHAPTER FOUR

4.0 HEATING AND STRESS ANALYSIS

The FE modeling of the welding process, temperature distribution and the subsequent stress analysis is discussed in this section

4.1 Numerical Simulation of the Welding Process

In the section, the numerical study of the work is presented. Numerical simulation of technological processes including welding is permanently a subject of research and practical applications [38].

In this work, the simulation is of two types; the thermal and the stress analysis. The thermal analysis for temperature distribution and residual stress due to laser welding will be performed. The sequential couple procedure in which the transient heat transfer analysis is followed by the thermal stress analysis will be adopted.

4.1.1 Thermal Analysis

To determine the thermal field during the welding process, a thermal analysis is required, incorporating the moving heat source. The most significant factors affecting the analysis are the heat input rate, the moving speed of the heat source and the thickness of the plate material[51].

4.1.2 Heating Analysis

The fundamental behavior of heat conduction is that of a flux[52], q, of energy flows from a hot region to cooler regions, which is linearly dependent on the temperature gradient, (∇T), i.e:

$$q = -k\left(\frac{\partial T}{\partial x} + \frac{\partial T}{\partial y} + \frac{\partial T}{\partial z}\right) \quad (20)$$

Where k is the thermal conductivity and it should be noted that the minus sign is necessary in order to keep q positive. The energy required to change the temperature of the materials is defined by specific heat c_p or enthalpy H. The conservation of energy is expressed in a differential form having the terms for specific heat, thermal flux and a distributed volume heat-source term S_0 (W/m^3) and it is given as[51]:

$$\rho c_p \partial T/\partial t - \nabla(k\nabla T) - S_0 = 0 \tag{20}$$

where $\boldsymbol{t}$ is the time parameter and ρ is the density of the material.

The thermal boundary conditions at all surfaces of the plate are assumed to be the same for the numerical simulation. Convection and radiation losses from the surfaces are considered and the heat transfer coefficients h are divided to include radiation and convection effects. Given a body temperature T, radiation to the surrounding medium at the temperature T_0 follows the Stefan–Boltzmann law, so the resulting temperature difference causes a flux (power loss) defined as[52]:

$$\dot{q}_{rad} = \sigma\varepsilon(T^4 - T^4{}_0) \tag{22}$$

$$= \sigma\varepsilon(T^2 + T^2{}_0)(T + T_0)(T - T_0) \tag{23}$$

$$= h_{rad}(T - T_0) \tag{24}$$

Where $h_{rad} = \sigma\varepsilon(T^2 + T^2{}_0)(T + T_0)$ (25)

Where ε is the emissivity, σ is the Stefan–Boltzmann constant and h_{rad} is the resulting temperature dependent heat transfer coefficient for radiation. Given a body with temperature T, surrounded by a fluid or gas at temperature T_0, heat convection assumes that a thermal layer

exists with the heat transfer coefficient h_{conv}, so the resulting temperature difference across the boundary layer causes a flux, $\dot{q}_{\text{conv}}$, given by

$$\dot{q}\_conv = h_{conv}(T - T_0) \tag{26}$$

where h_{conv} is the heat transfer coefficient for convection (W/m^{2}K), σ is the Stefan-Boltzmann constant for radiation (5.67 × 10^{-8} W/m^{2}K^4), ε is the emissivity, T is ambient temperature (K). Initially the sample material is assumed to be at a reference temperature, $T_{0,}$ hence, the initial condition is $T = T_0$ at t = 0

However, the convection heat transfer coefficient incorporating emissivity as proposed by Frewin and Scott is used in this analysis given by Eqn. (27). The temperature dependent mechanical and thermal properties of the 316L steel blanks are given in figures 21 and 22 respectively.

$$h_{conv} = 2.4 \times 10^{-3} \varepsilon T^{1.61} \tag{27}$$

Figure 21 shows the schematic diagram of the simulation model and coordinates. The following thermal boundary conditions were applied to the surfaces:

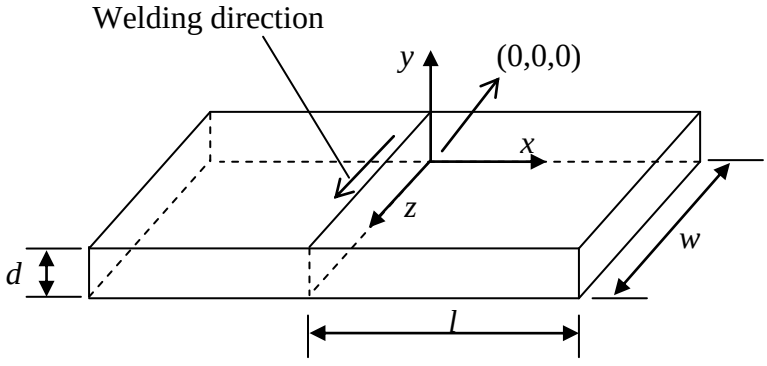

Figure 21: Schematic diagram of the Simulation model and cordinates

At x = $\pm l$, y = 0, z =w:

$\dot{q}_{\text{conv}}$ and $\dot{q}_{\text{rad}}$ at the surfaces are considered

At $x = \pm l$, $y = d$ and $z = 0$:

$\dot{q}_{\text{conv}}$ and $\dot{q}_{\text{rad}}$ at the surfaces are considered

At $x = \pm l$, $y = 0$ and $z = w$:

$\dot{q}_{\text{conv}}$ and $\dot{q}_{\text{rad}}$ at the surfaces are considered

At $x = \pm l$, $y = d$ and $z = w$:

$\dot{q}_{\text{conv}}$ and $\dot{q}_{\text{rad}}$ at the surfaces are considered

At $x = 0$, $y = d$ and $z = w$:

$\dot{q}_{\text{conv}}$ and $\dot{q}_{\text{rad}}$ at the surfaces are considered

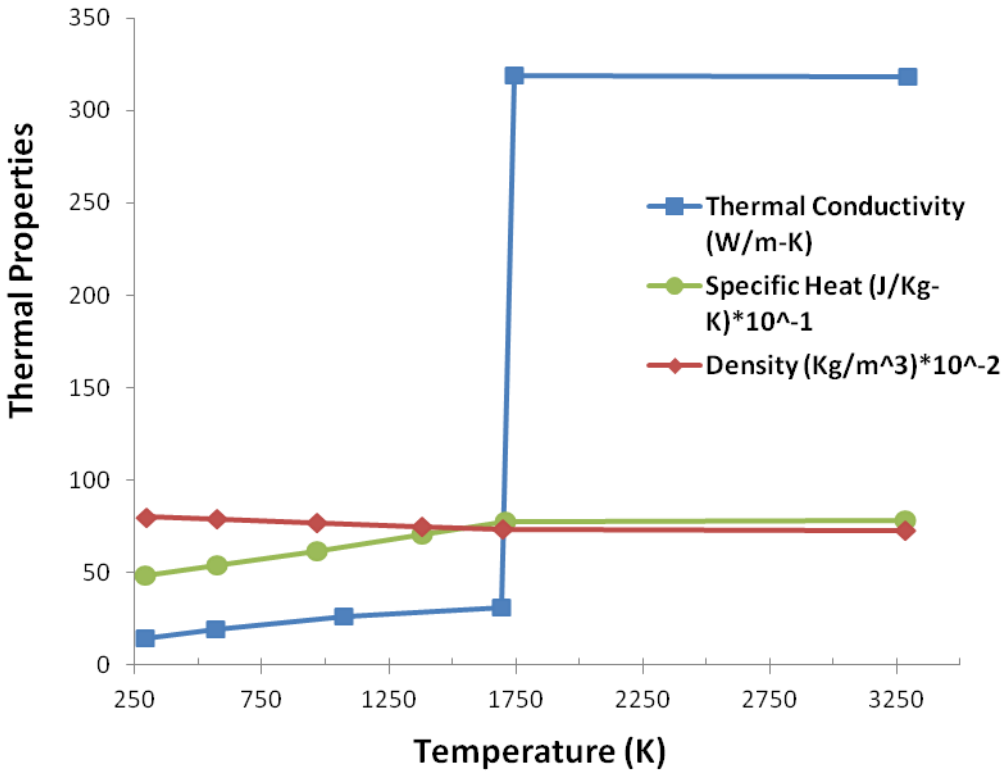

Figure 22: AISI 316L Temperature Dependent Thermal Material Properties[11]

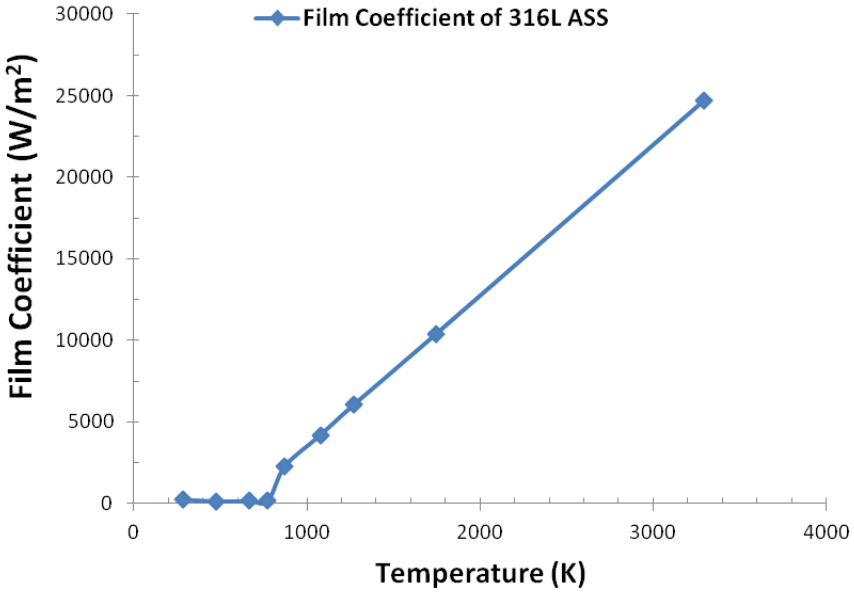

Figure 23: Film Coefficient[11]

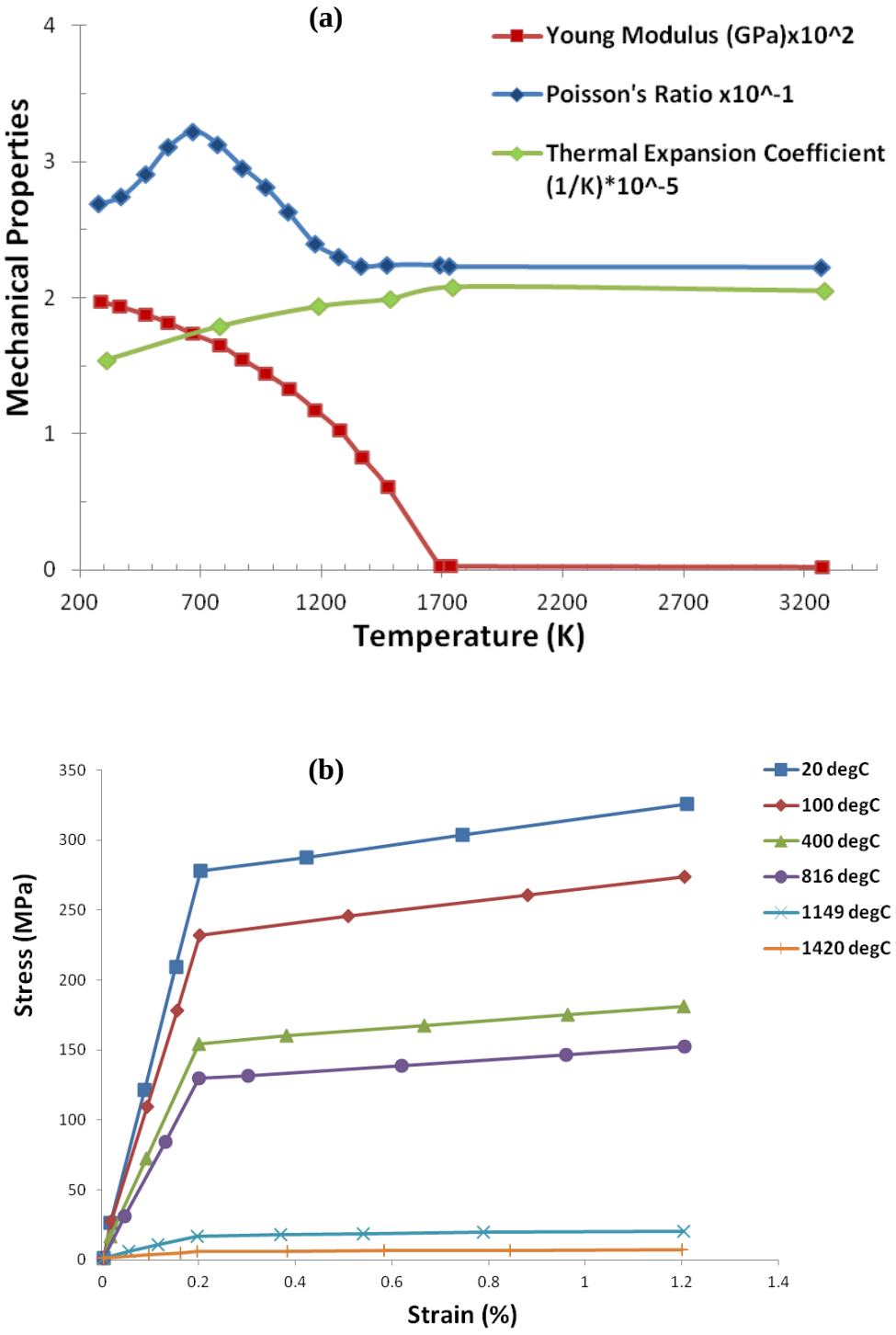

Figure 24: (a) AISI 316L Temperature Dependent Mechanical Material Properties (b) 316L Stress – Strain Curves[53]

4.1.3 Heat Source Model

From the review of literatures, it is noticed that research is in progress focused at developing an accurate heat source model for laser welding process. Knowledge of the heat transfer from the welding source to the base material is essential for determining the molten pool or bead shape and the subsequent solidification pattern[51]

Researchers have employed different heat source model; the Gaussian distribution of heat flux (W/m^2) deposited on the surface of the workpiece as shown in Figure 25, 3D conical Gaussian profile as shown in Figure 26 and the double-ellipsoidal heat source model (Figure 27) [37, 40, 51, 54-56]. A recent study concentrated on the modification of these heat source model to accurately account for the physical phenomenon[57]. In this study, the double ellipsoidal heat source model was used due to its capability of simulating laser beam welding on a thin plate [58, 59].

Definition of the Double Ellipsoid Heat Source Model

The double ellipsoidal heat source model entails two dissimilar power sources of the same geometrical shapes but of different dimensions. These two different components of the model define the front and the rear of the heat source, respectively. The mathematical equation that describes the front of the heat source models its steep shape, resulting from the movement of the heat source while that of the rear heat source is adapted to the smooth gradients of the heat flux [53]. In essence, the heat source is a combination of two different semi-ellipsoids described by separate equations:

For a point (x, y, z) in the front semi-ellipsoid of the model, the governing equation of the power density (W/m^3) is:

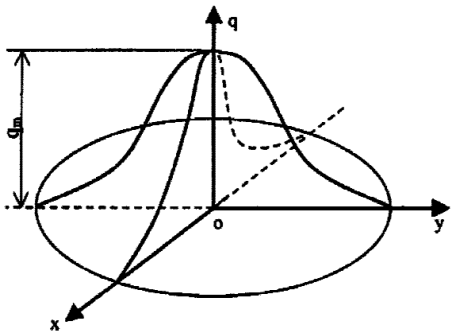

Figure 25: Gaussian distribution of heat intensity[55]

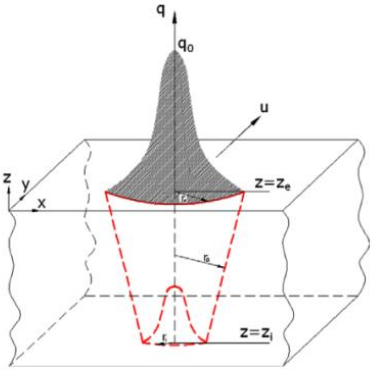

Figure 26: 3D Conical Gaussian distribution of heat source[51]

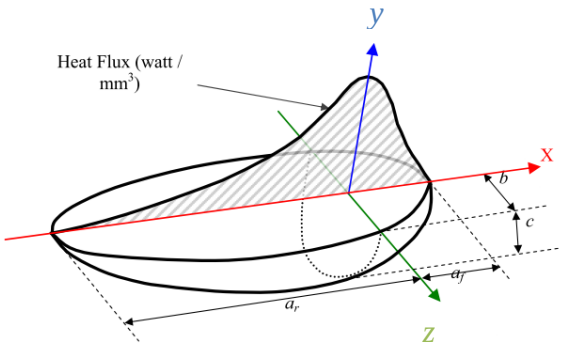

Figure 27: double Ellipsoidal representation of the heat source[56]

$$Q_f(x,y,z) = \frac{6\sqrt{3}f_f Q}{a_f bc\pi^{3/2}} exp^{\left(\frac{-3x^2}{a_f{}^2}\right)} exp^{\left(\frac{-3y^2}{b^2}\right)} exp^{\left(\frac{-3z^2}{c^2}\right)} \quad (27a)$$

While for a point in the rear semi-ellipsoid model, the heat flux is described as:

$$Q_r(x,y,z) = \frac{6\sqrt{3}f_r Q}{a_r bc\pi^{3/2}} exp^{\left(\frac{-3x^2}{a_r{}^2}\right)} exp^{\left(\frac{-3y^2}{b^2}\right)} exp^{\left(\frac{-3z^2}{c^2}\right)} \quad (27b)$$

Where a_f, a_r, b and c are the ellipsoid heat source geometric parameters as shown in figure 25. Q is the laser beam power (W) which includes the efficiency of the beam power reaching at the surface. The parameters f_f and f_r are proportion coefficients representing heat apportionment in front and back of the heat source respectively[11]. The sum of the fractions (f_f & f_r) between the heat deposited in front and rear quadrant must equal two, that is:

$$\boldsymbol{f_f + f_r = 2} \quad (28a)$$

For the condition of continuity of the overall volumetric het source in equations 27a and 27b when $x = 0$ the following condition for coefficient must be satisfied:

$$f_f = \frac{2a_f}{a_f + a_r} \quad (28b)$$

or

$$f_r = \frac{2a_r}{a_f + a_r} \quad (28c)$$

4.1.4 Geometry of the Finite Element Model

The element chosen for the analysis is SOLID 70. It has 3D thermal conduction capability for three dimensional steady-state or transient thermal analysis. The element has eight nodes with a single degree of freedom; temperature, at each node. The element also can compensate for mass transport heat flow from a constant velocity field. The geometry of solid 70 is shown in Fig 27.

The FE models are shown in Fig. 28. Table 7 shows the number of finite elements and nodes for each FE model considered in this study. This number of elements and nodes were chosen after conducting the mesh independency test (mesh convergence test) in order to reduce the simulation run-time while maintaining its accuracy. The smallest element used in the FEA model is in the welded zone and has the dimension of 0.2mm × 0.5mm × 0.375mm, 0.2mm × 0.5mm × 0.5mm, 0.2mm × 0.5mm × 0.625mm and 0.2mm × 0.5mm × 0.75mm for model 1.5, 2, 2.5, and 3 respectively and they gradually increase in size away from the weld region. Along the thickness direction four (4) elements were used in all the FE models. The size and type of the element are crucial to obtain accuracy of the result and reduction of solution time required for finite element analysis.

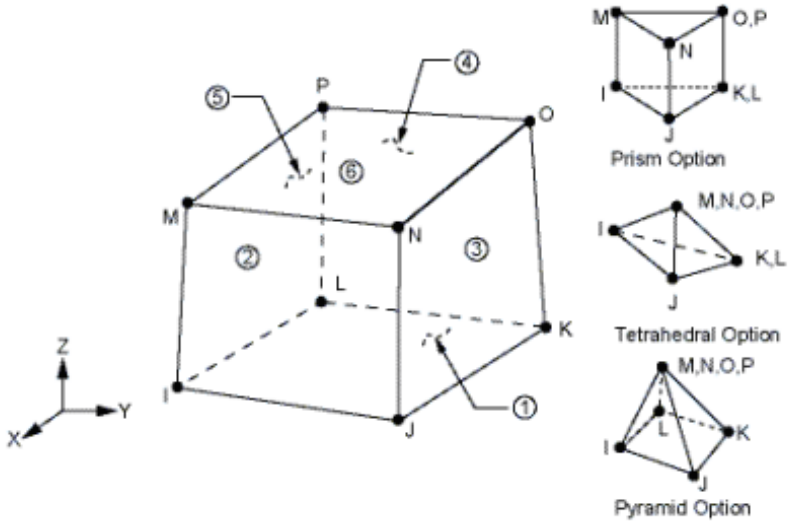

Figure 28: Geometry of Solid 70

Table 7: Number of Elements and Nodes of FE Models	
FE Model	Number of Elements
1.5	19712
2	21320
2.5	22880
3	22880

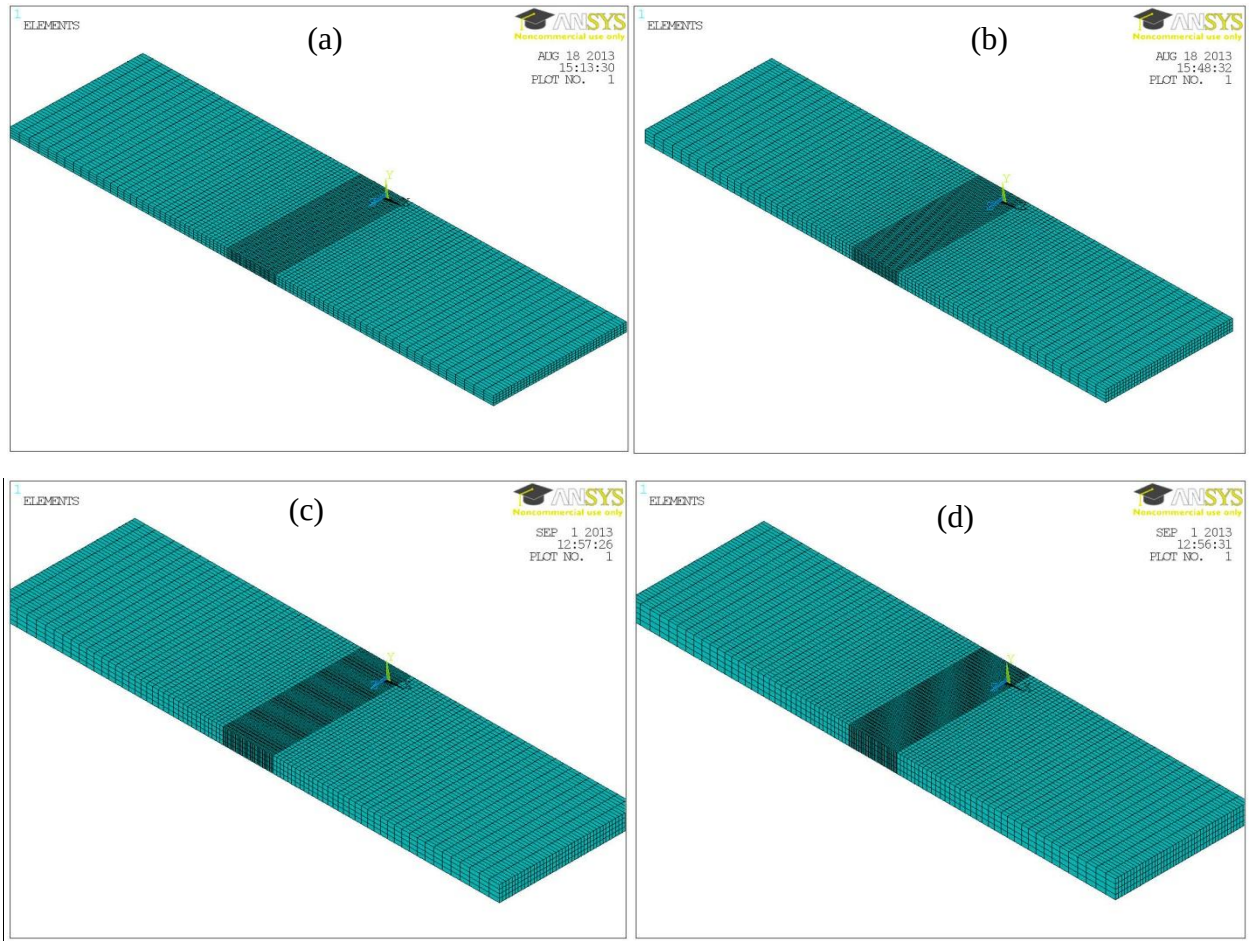

Figure 29: Finite Element Models (a) model 1.5 (b) model 2 (c) model 2.5 (d) model 3

4.2 Structural Analysis

The FEM structural analysis carried out in this study use the sequential thermal-stress solution procedure in which the transient thermal analysis is followed by the thermal stress analysis. Resulted temperatures distributions from the thermal analysis were used as loading for the thermal stress analysis. This means that at the end of the thermal analysis, all nodal thermal results, for every time-step, were written in the result file and inputted as the body load in the structural analysis. In a coupled field analysis, the accuracy of the structural analysis is rested on the correctness thermal analysis results, however the following important procedures must be implemented to achieve reliable structural results:

1. Must ensure geometrical compatibility by adopting the same FEM model and mesh used during thermal analysis for the structural part
2. A corresponding thermal element type must be used for the structural analysis.
3. Mechanical temperature dependent properties must be used and the optional deletion of the thermal properties, in order to free the solver unnecessary information
4. The transient structural analysis must be exactly the same with the transient thermal analysis, meaning that the exact number of time steps and time intervals must be used for both analyses in order to avoid confusion and erroneous results.
5. For each time step, the load is read from the thermal result file and inputted as body load in the structural analysis.

Also, Zhu and Chao[60] has indicated that the yield stresses at all temperatures are the most important parameter in welding simulation and that its value has significant effect on the residual stress.

The element type used in the current structural analysis is the ANSYS® SOLID185 element which is the corresponding element type for the thermal element type used. The temperature-dependent mechanical properties of 316L ASS was presented in Figure 23(a) and the Stress-Strain curves in Figure 23(b) from which the yield stresses where obtained. To effectively stimulate the phase change, temperature-dependent enthalpy reported here [41] were used.

During the welding process, because solid-state phase transformation does not occur in the stainless base metal and the weld metal, the total strain rate can be decomposed into three components as follows [61]:

$$\dot{\varepsilon} = \dot{\varepsilon}^{e} + \dot{\varepsilon}^{p} + \dot{\varepsilon}^{th} \quad (29)$$

Where the components on the right side of Equation (29) are the elastic strain, plastic strain and thermal strain respectively. The elastic strain is modeled using the isotropic Hook's law with temperature-dependent Young's modulus and Poisson's ratio. The thermal strain is computed using the temperature-dependent coefficient of thermal expansion. For the plastic strain, rate-independent plastic model is used with the following characteristics: the Von Mises yield criterion, temperature-dependent mechanical properties, and bilinear Isotropic (BISO) hardening model.

CHAPTER FIVE

5.0 RESULTS AND DISCUSSIONS

Findings of the modal parameters and experiments of welded 316L steel blanks are presented in this chapter.

5.1 Modal Analysis

The experimental set-up which consists of an interface between the data acquisition system and software package for signal processing - labVIEW 2011 SP1, was used to acquire the natural frequency of 316L steel blank samples. Figure 30 shows a set of the results obtained from modal testing using the data acquisition interfaced with the software package for "as received" (unwelded) samples. Peaks due to electrical noise where within the frequency range of 56 – 61Hz for all samples investigated. This is the electrical frequency of AC powered devices used during the experiment. The results indicate that as the sample thickness increases the obtained natural frequency also increases. This follows the fact that a large plate thickness increases the moment of inertia of the plate which in turn increases the resistance of the plate to flexure thereby increasing the natural frequency of the as received plate.

To validate the FFT results obtained from labVIEW 2011 SP1 which the natural frequencies are read from, comparisons is made with numerical results. Numerical modeling of the modal analysis is conducted using the FEM ANSYS software code for the same geometry of the "as received" 316L steel plates. Since the natural frequency of a system is influence by the geometry and is more or less an extrinsic properties, the effect of the attached accelerometer at the free end of the plates needs to be consider during the simulation. Because of this, the FE model of the

accelerometer was incorporated in the model of the tested sample as shown in Figure 31. Ansys finite element Solid 5 which is a 3-D element with eight nodes and up to six degrees of freedom with thermal and structural capability. A total of 197,107 elements were used, this number of elements satisfy the mesh independency test at reasonably computational time. Figure 32 shows the natural frequency plots from numerical modeling of unwelded plates for different sample thicknesses. It is found that the natural frequency increases as the thickness of the sample increases while the deflection decreases from 7.5 to 6.5mm as the thickness of the sample increase from 1.5 to 3mm respectively. This trend is consistent with theory of modal analysis presented in [47, 48]. This behavior is link to the sample thickness direct influence on the moment of inertia of the plate, which increment will cause the flexure resistance of the system to rise and thereby increasing the natural frequency as stated earlier.

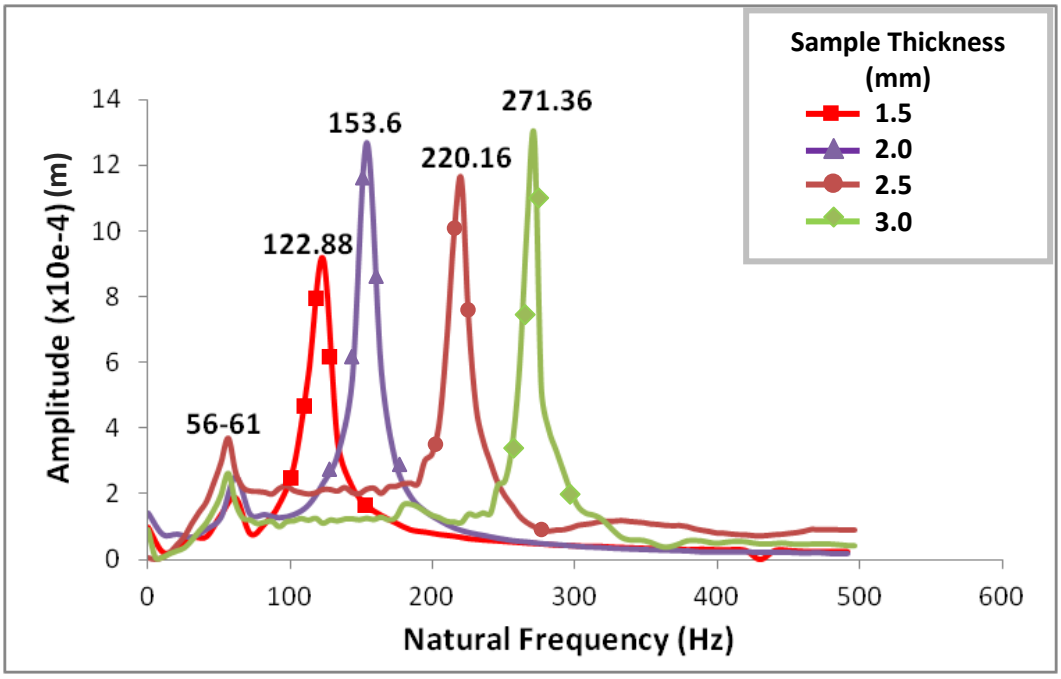

Figure 30: Natural Frequency of unwelded samples of different thickness

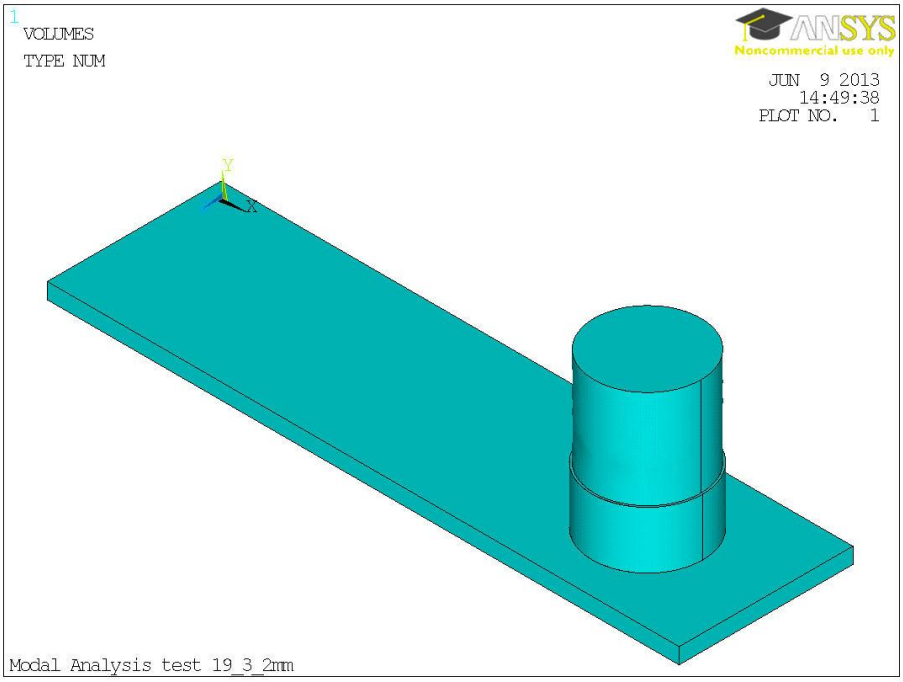

Figure 31: Geometrical model of unwelded sample and accelerometer

Therefore, larger sample thickness indicates higher natural frequency due to the subsequent effect of the sample thickness on the inertia of the system. Several readings of the modal testing of these samples were averaged to compare with results obtained numerically. Table 8 shows the comparison with 9.65% maximum percent difference for the 1.5mm thick blank. The comparison and variation are clearly shown in Figure 33. These differences are still within acceptable range to conclude that the numerical results are in agreement with the results acquired from the experimental test. Hence welded samples with different parameters as shown in tables 3 through 6 are then investigated.

Figure 34 shows the natural frequency peaks of a welded sample using different beam power while other welding parameters are kept constant (see table 5). It is noticed that the natural frequency of the welded samples are similar to that of the unwelded sample of the same thickness. This is an indication of defect-free weld and less distortion of welded region

accompanying laser welding process. It is also observed that the natural frequency increases as the laser beam power increases as shown in Figure 35 in which variation of the natural frequency as a factor of the beam power is shown. This behavior is associated with the fact that as the beam power increases, the coarser the microstructure becomes [8, 62], and the more coarse the microstructure of a material is, the more easily deforming the material becomes. This results in large grains and less grain boundaries that aid in hindering deformation.

Effects of welding speed (feed rate) of the beam on the natural frequency peaks are shown in Figure 36. It is found that at a lower feed rate (200mm/min) the natural frequency is 122.88Hz. An increase in the welding speed (feed rate) to 300mm/min results in a decrease of the natural frequency (107.52Hz). Accordingly, El-Batahgy [62] reports that the higher the welding speed, the finer the microstructure. This is attributed to an increase in both solidification and cooling rates due to the low heat input that results from a higher welding speed. Fine microstructure indicates more resistance to deformation and increased material stiffness, hence the lower natural frequency. Similar trend is also observed as shown in Figure 37 where different set of parameters are investigated. This seems to be true for first two results but on further increase in the weeding speed the natural frequency increased rather than decrease as expected. Further increase of the welding speed to 400mm/min results in a natural frequency of 117.76Hz. This behavior can be attributed to the fact that at a higher welding speed attenuation of beam energy by plasma is less significant. This results in relatively more exposure of the laser beam on the sample which in turn increases the heat dissipation on the workpiece. It is also worth mentioning that natural frequency is again within the range of the unwelded sample of same thickness indicating the absence of distortions and defect-free welds. These variations of frequency with welding speed are illustrated in Figure 38 for both cases.

Effects of the variation of the thickness of welded samples on the natural frequency were examined and shown in Figure 39, where other welding and geometry parameters (welding speed, beam power etc and length, breadth respectively) are held constant. Figure 40 shows the variation of the natural frequency of investigated samples with sample thickness. The sample thickness varies directly as the natural frequency. This can be explained thus; an increase in the sample thickness results in an increase in the moment of inertia of the system, which directly relates to the natural frequency.

The natural frequencies obtained from modal analysis testing are then used to calculate the stiffness and elastic modulus of the welded blanks. Table 9 shows the calculated stiffness and elastic modulus of all samples. It is found that the values of the calculated elastic modulus are similar to that of the base material. Considering the welding and geometry parametric influence on the elastic modulus, the noticed difference may be due the modification of the material microscopic properties during the welding process.

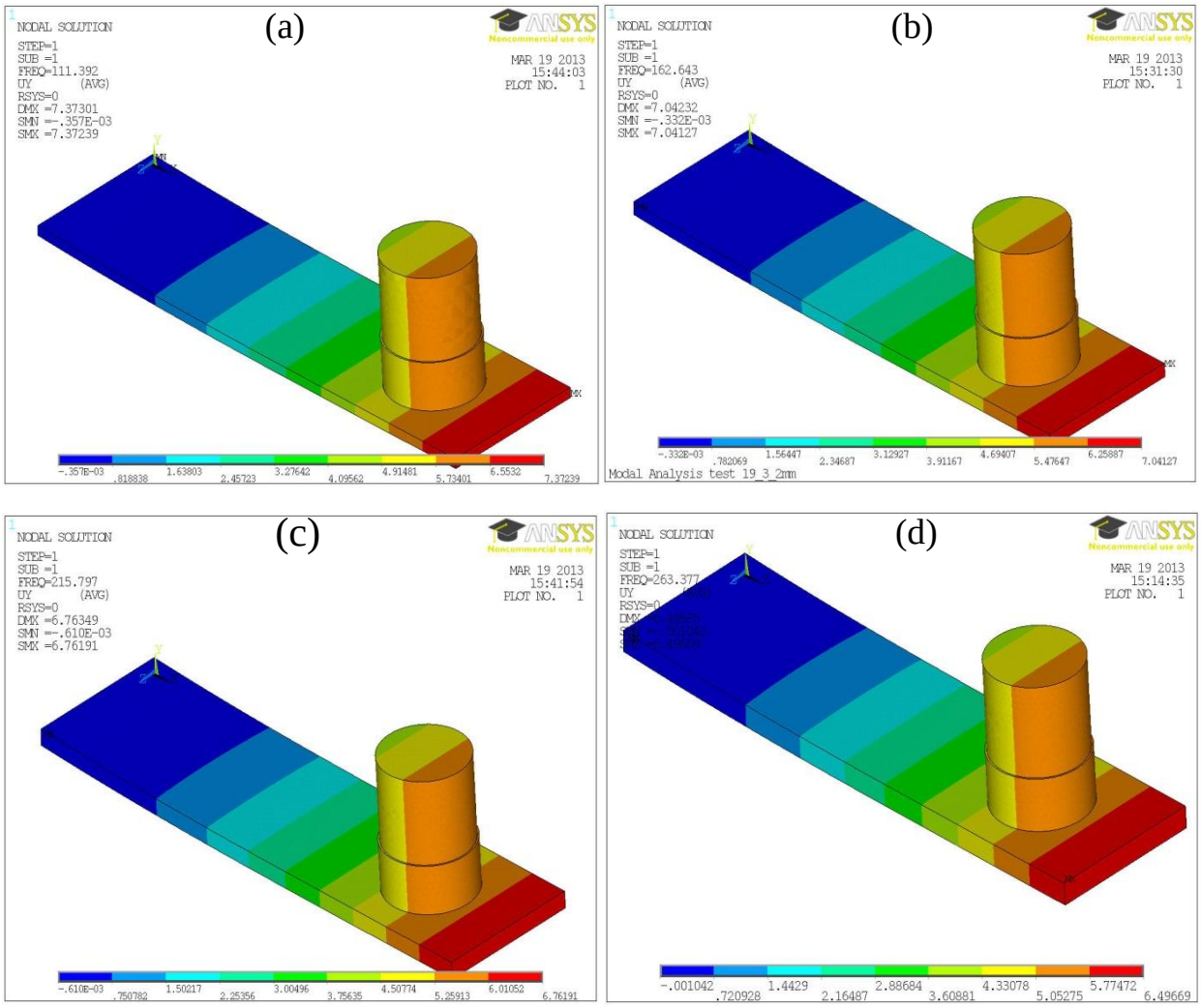

Figure 32: Numerical plot of the Natural Frequency of unwelded samples for different sample thickness:(a) 1.5mm (b) 2mm (c) 2.5mm (d) 3mm thick

Table 8: Comparison of the Natural frequency of modal test and numerical results of unwelded Samples			
Sample Thickness	Modal Test f_n (Hz)	Numerical f_n (Hz)	% Difference
1.5	122.88± 6.14	111.39	9.81
2	153.60± 7.68	162.643	5.72
2.5	220.16± 11.00	215.91	1.95
3	271.36± 13.57	263.38	2.98

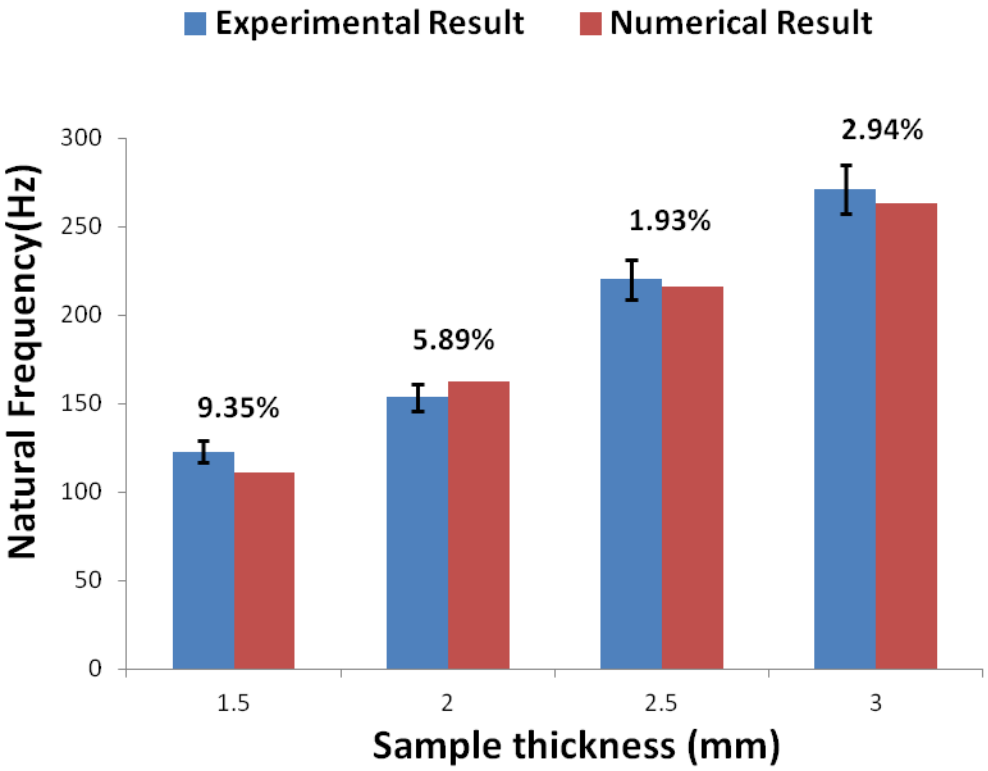

Figure 33: Comparison of the Natural frequency of modal test and numerical results of unwelded Samples

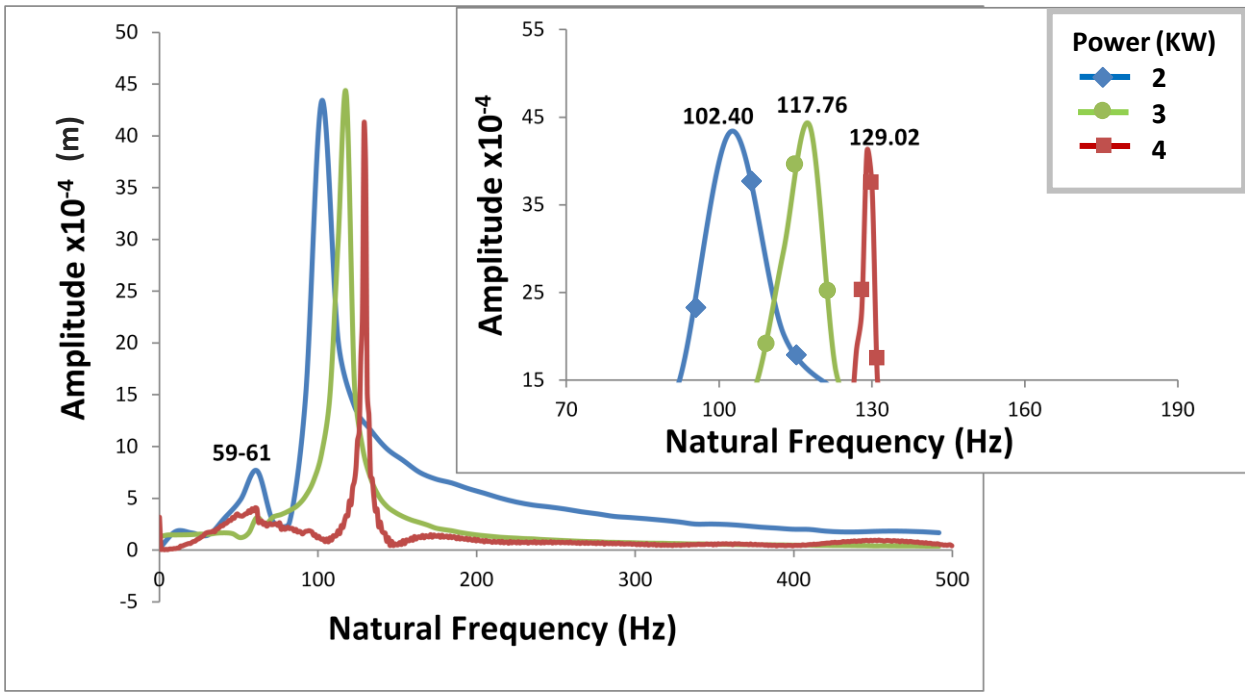

Figure 34: Natural Frequency of 1.5mm thick samples welded with 400mm/min using different Beam Power

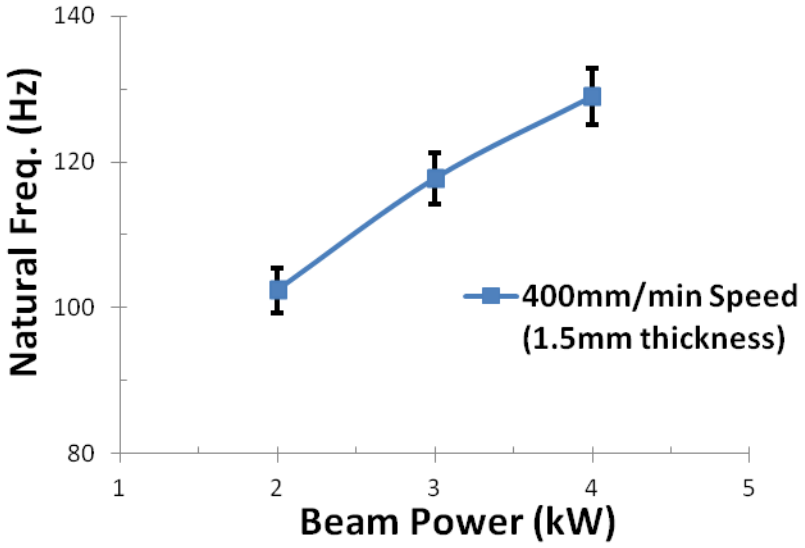

Figure 35: Natural Frequency variation with Beam Power

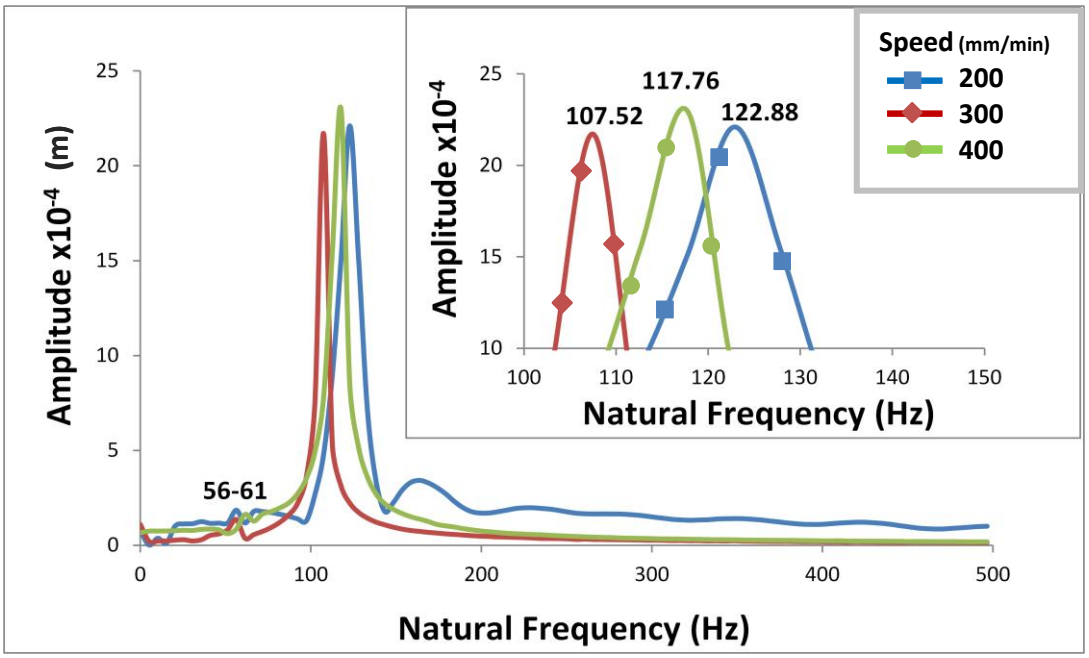

Figure 36: Natural Frequency of 1.5mm thick samples welded with 3KW using different feed rate

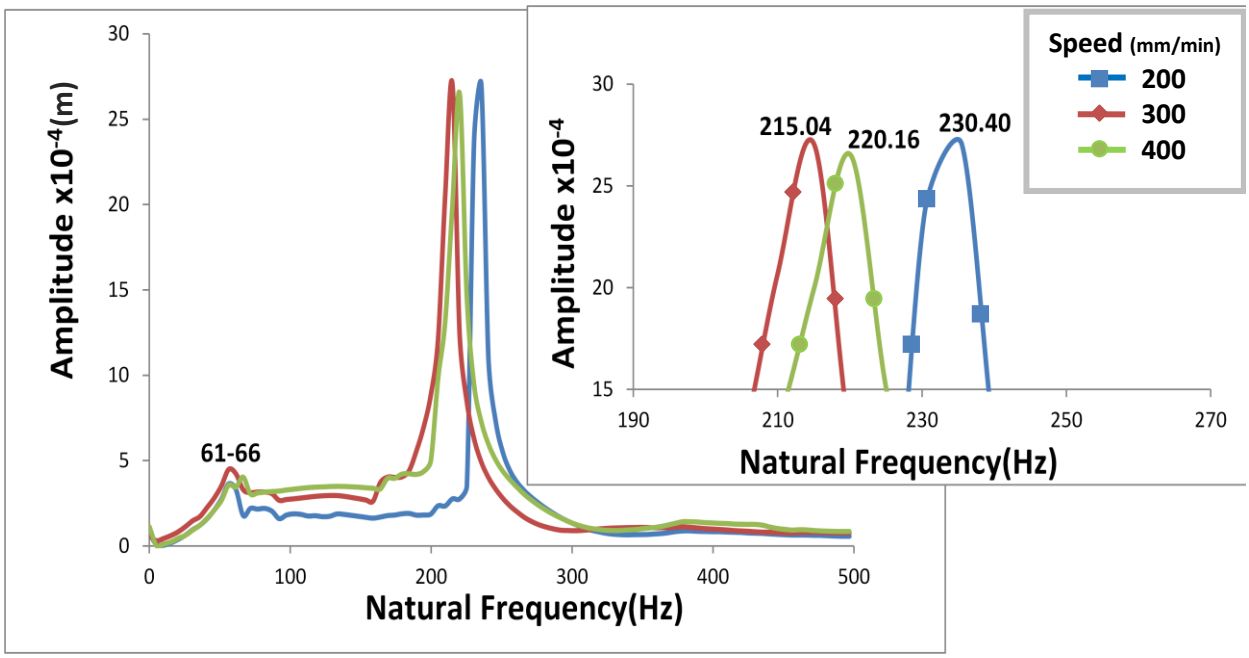

Figure 37: Natural Frequency of 2.5mm thick samples welded with 4KW using different feed rate

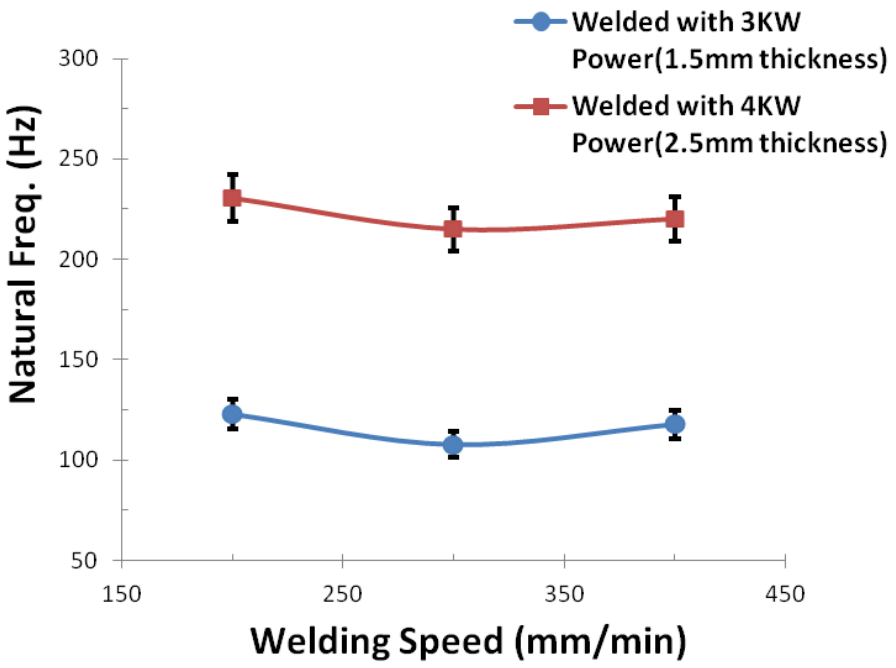

Figure 38: Natural Frequency variation with welding speed

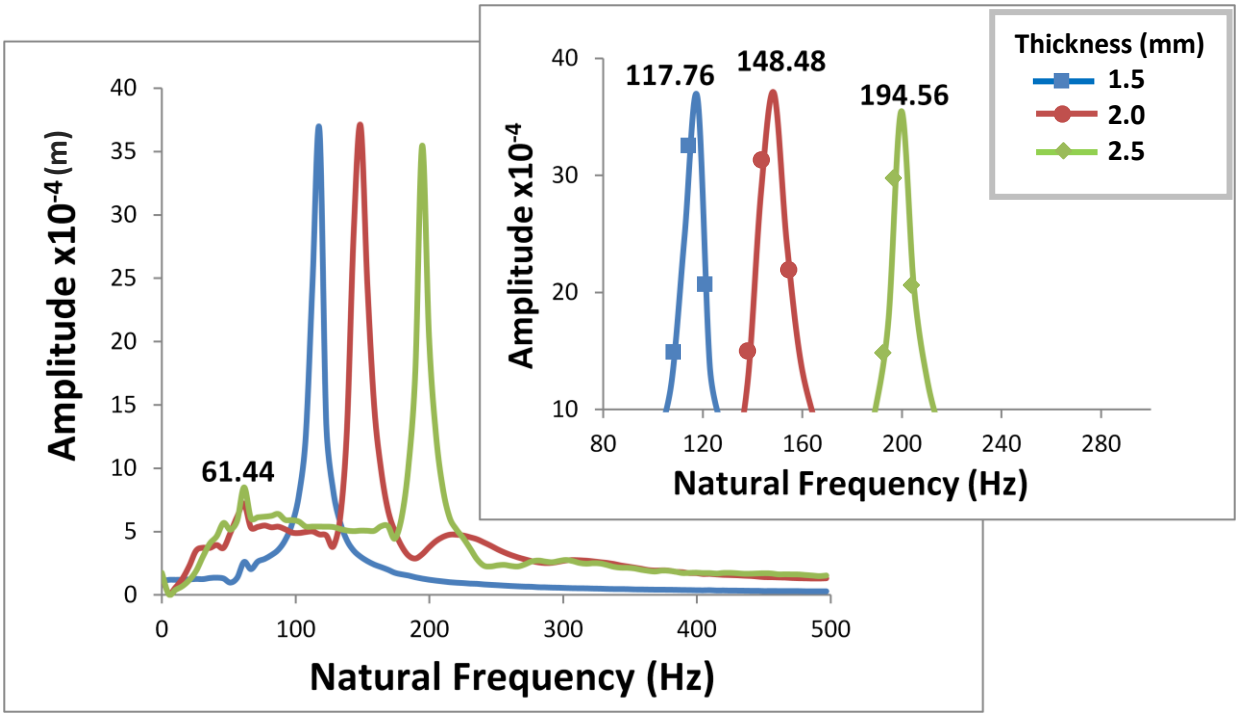

Figure 39: Natural Frequency of samples welded using 3KW power and 400mm/min welding speed for different thickness

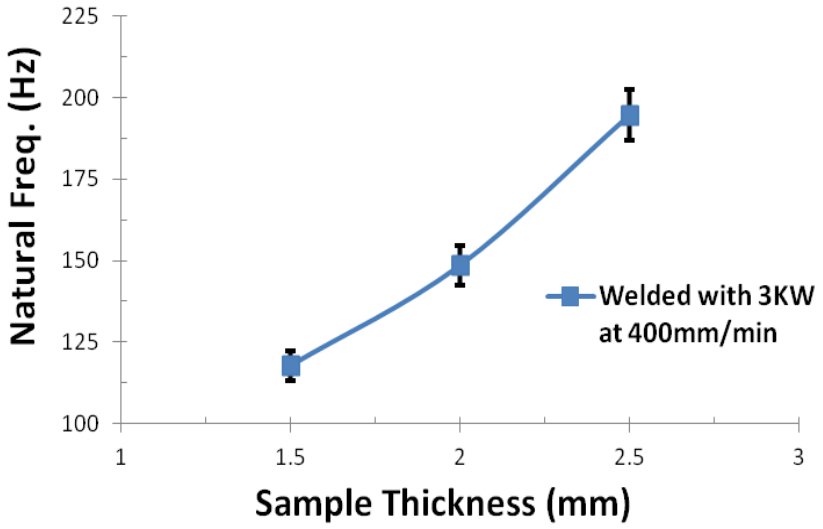

Figure 40: Natural Frequency variation with sample thickness

Table 9: Calculated Stiffness and Elastic Modolus of welded sample			
Power (W)	F_n (Hz)	K (N/m)	E (GPa)
2000	102.40	6679.0963	184.13
3000	117.76	8833.1048	243.64
4000	129.02	10603.076	292.26
Speed (mm/min)	F_n (Hz)	K (N/m)	E (GPa)
200	230.40	41519.479	247.16
300	215.04	36168.08	215.35
400	220.16	37910.872	225.31
Speed (mm/min)	F_n (Hz)	K (N/m)	E (GPa)
200	122.88	9617.8987	265.07
300	107.52	7363.7037	203.10
400	117.76	8833.1048	243.64
Thickness (mm)	F_n (Hz)	K (N/m)	E (GPa)
1.5	117.76	8833.1048	243.64
2	148.48	15554.188	180.26
2.5	194.56	29606.977	176.16

5.1.1 Analysis of the Acquired Data

To predict the variation of welding speed (WS), laser beam power (LP), and sample thickness (ST) with data obtained from experiments, a step-wise regression analysis is carried out (see Appendix), where the insignificant model terms can be eliminated. Table 5 shows the natural frequency obtained from the experimentation and the corresponding variable matrix. Statistical software Minitab 16 was used to analyze the data. Variation inflammatory factor (VIF) check was conducted to test the collinearity and the interaction terms (WS*ST, WS*LP and ST*LP) of the parameters considered. The VIF test reveals that the interaction and the second order terms do not contribute to the significance of the model. Hence, linear model were fitted to the experimental data so as to derive the regression equation and the fit summary output shows that this linear model is statistically favored for the natural frequency. The best subset regression (table 6) analysis reveals that the three independent parameters are essential for the best prediction of the model. All the adequacy measures are close to 1 which indicate adequate model, except for WS which indicates the less significant effect on the natural frequency. The analysis of the variance, t-test and p-values show that the main effect of the sample thickness (ST) and the laser beam power (LP) are the most significant model terms associated with the natural frequency. However, the sample thickness is the most significant term influencing the model. The resulting mathematically model from the regression in terms of these parameters is;

$$\textbf{Nat. Frequency (NF)} = -47.4 - 2842*(WS) + 85678*(ST) + 0.0168*(LP) \quad (30)$$

The accuracy related to the measured R-sq value of Eqn. (30) is in the order of 98.7%, the adjusted R-sq value is 98% and the predicted R-sq value is 96.61%.

Figure 41 compares between the measured and predicted variation of the natural frequency with the laser power and the samples thickness respectively. The predicted natural frequency is

follows similar trend and is in agreement with the measured natural frequency. The little deviation observed result from the effect of the welding speed, which has less contribution to the accuracy of the model. If ST and LP are held constant, the deviation of the model from the measured natural frequency becomes high as illustrated in Figure 42. The sample thickness been the major influencing parameter of the natural frequency is another indication of the defect-free weld joint resulting from the laser welding process.

Table 10: Best Subsets Regressions

Best Subsets Regression: NF versus WS, ST, LP							
Response is NF							
Vars	R-Sq	R-Sq(adj)	Mallows Cp	S	WS	ST	LP
1	93.9	93.1	21.3	13.314		X	
1	49.1	42.8	220.1	38.338			X
2	98.1	97.5	4.6	7.998		X	X
2	95.3	94	16.7	12.405	X	X	
3	98.7	98	4	7.2106	X	X	X

Table 11: Regression Equation

The regression equation is					
NF = - 47.4 - 2842 WS + 85678 ST + 0.0168 LP					
Predictor	Coef	SE Coef	T	P	VIF
Constant	-47.43	17.74	-2.67	0.037	
WS	-2842	1759	-1.62	0.157	1.06
ST	85678	5782	14.82	0	1.43
LP	0.016753	0.004367	3.84	0.009	1.5
S = 7.21063 R-Sq = 98.7% R-Sq(adj) = 98.0%					
PRESS = 784.224 R-Sq(pred) = 96.61%					

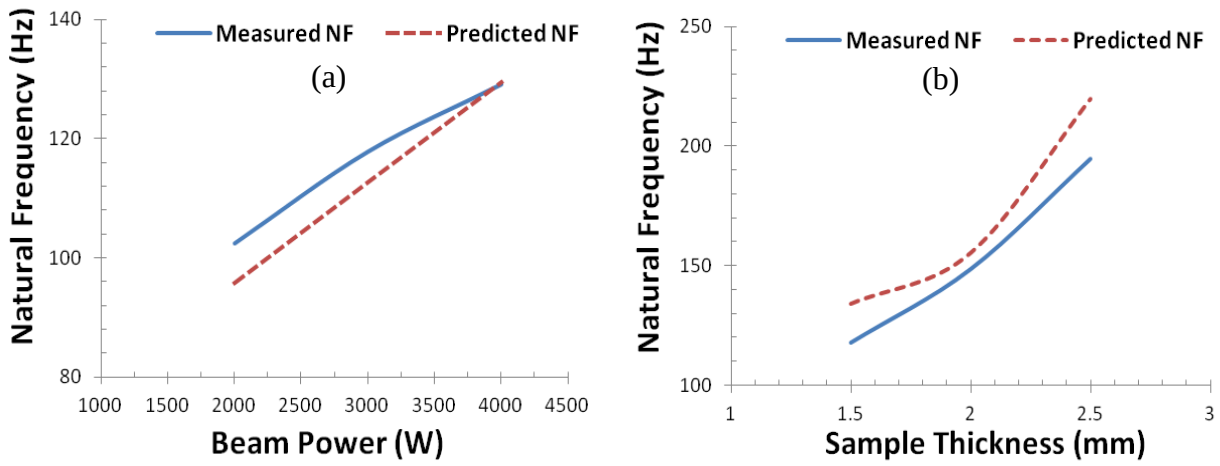

Figure 41: Measured and Predicted Natural Frequency variation with (a) Laser Beam Power (b) Sample Thickness

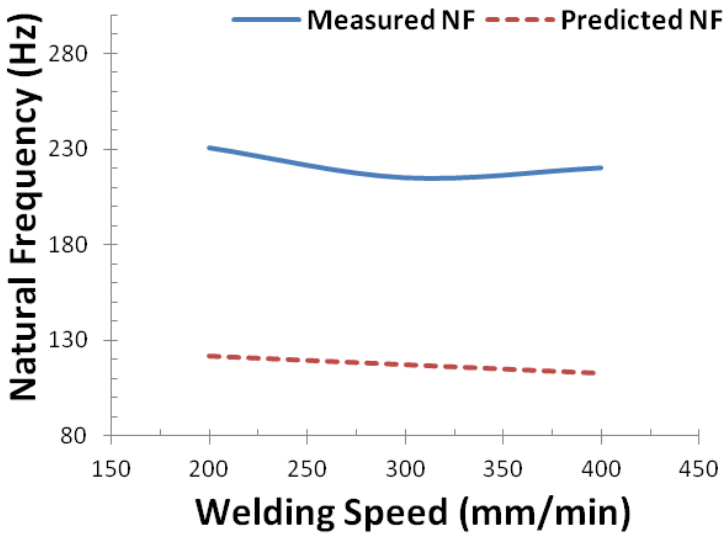

Figure 42: Measured and Predicted Natural Frequency variation with welding speed

5.2 MATERIAL CHARACTERIZATION

The macrograph and micrograph of the cross-section of each sample were examined using a metallurgical optical microscope (Meiji MX7100, USA) and scanning electron microscope SEM (LYRA3 XM, TESCAN, Germany) to reveal the shape of the fusion zone and the weld bead width.

5.2.1 Macrostructure of the Welded Samples

The macrograph of the weld is examined to observe the shape of the fusion zone, the weld bead width and the full penetration weld across the sample thickness. Combination of the optical microscope and SEM are utilized in this examination. Due to non-uniformity in the shape of the fusion zone, a mean value of weld bead widths at the top, the centre and the bottom is reported as the weld bead width for all the examined samples.

It is seen from the micrographs showing the weld inlets and outlets that some materials loss occurs from the top and bottom surfaces respectively. This loss is associated to the evaporation of the workpiece's material due to exposure to the laser welding beam so far that this removal of material from the surface is not substantial enough to significantly reduce the sample thickness. However, significant material loss at the top surface which leads to the formation of cavity (Figures 43(a) & 45(c)) is observed at higher beam power which allows for quick evaporation of the material at the present of high intensity laser beam. This behavior is also noticed at lower welding speed as in figure 43(a). This is because of the increased dwell time of the laser beam power on the irradiated area which provides the evaporation at the surface and the recoil pressure developed in between the vapor front and the molten surface enhances the cavity formation in the irradiated region as observed in[63]. Material removal at the bottom surface is however

inconspicuous indicating that there is no excessive heating across the workpiece material during welding.

(a) Effect of welding speed

The parameters of tables 3 & 4 were used for demonstrating the effects of the welding speed. Figure 43 shows the optical micrograph of the three fusion zones welded with 4kW laser beam power. The fusion zones were almost symmetrical along the weld line except for some enlargement at the upper part of the weld. This enlargement can be due to any or a combination of the following reasons as stated in [63]: i) temporal fluctuations in the laser output power, ii) arbitrarily varying in the scanning speed, iii) changes in the assisting gas pressure (argon) during the welding process, and iv) inhomogeneity of the material such as elemental concentration variation in the welding section. It is observed that the initial intermittent variation of the process parameters e.g. laser power and welding speed, are most influential factors responsible for the irregular weld width variation at the top portion.

It is also noted that the weld bead width is indirectly related to the welding speed. Therefore, as the welding speed increases from 200 to 400mm/min, the weld thickness/width ratio increases from 4 to 6 and from 1.5 to 2.3 for 4kW and 3kW powers respectively. These relationships are clearly plotted in Figure 44 (a – b), where the linear behavior between welding speed and weld bead width, and between the welding speed and the thickness/bead width ratio is depicted. An increase welding speed reduces the laser beam dwell time on the workpiece. Consequently, the sample experiences less heat absorption and coupled with a high temperature gradient associated with laser welding translates to a narrow weld seam at higher welding speed. This is in agreement with reported studies in literatures [8, 62].

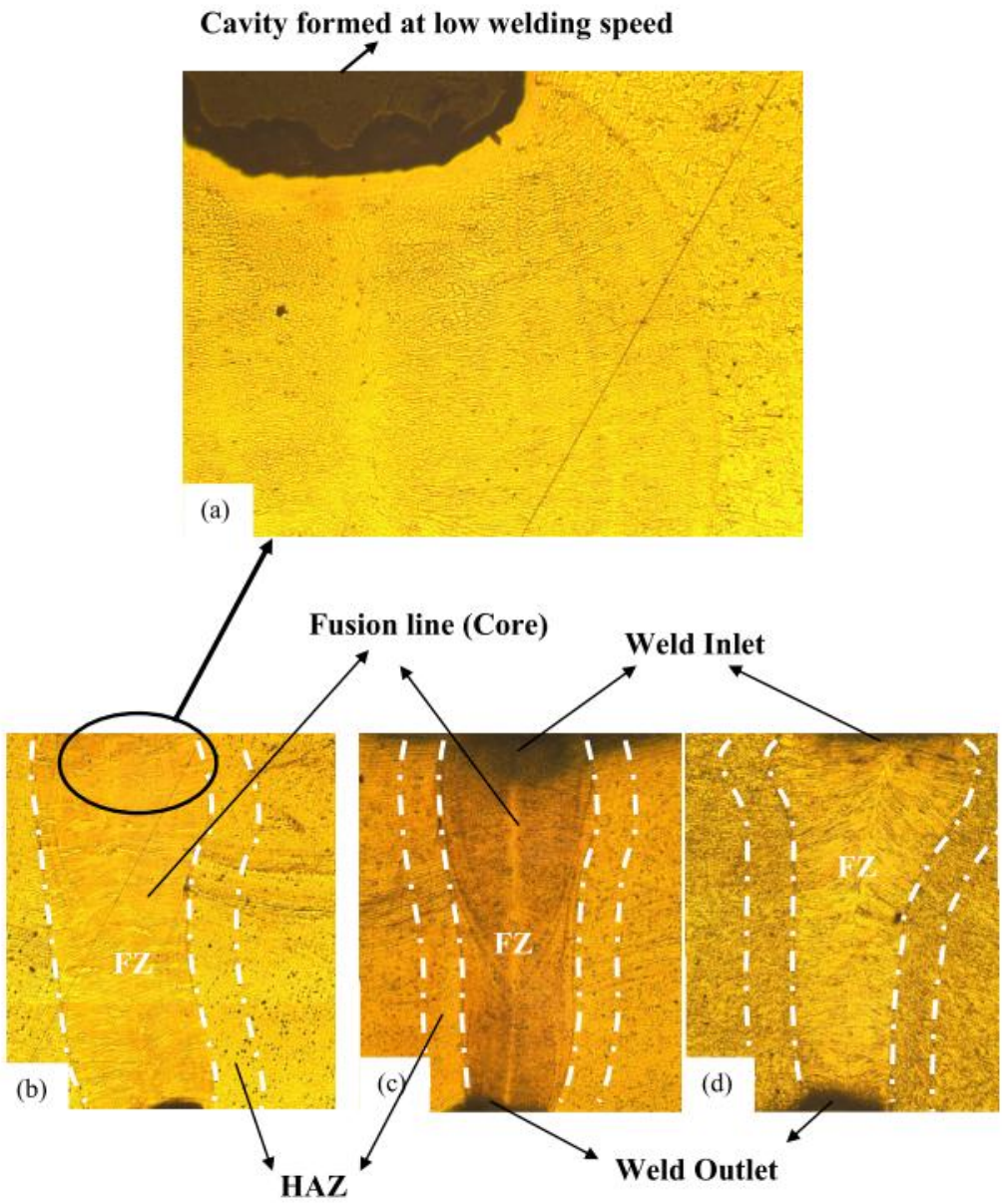

Figure 43: Optical Micrograph of the cross-section welded samples with varied feed rate (a) & (b) 200mm/min (c)300mm/min (d) 400mm/min (X5) (Laser beam Power = 4kW, Sample thickness = 2.5mm)

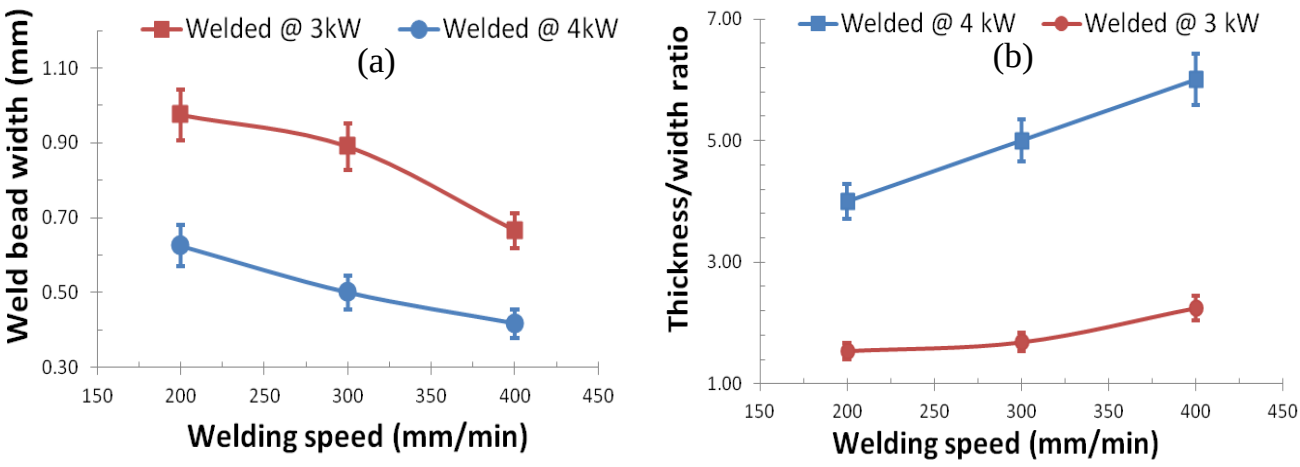

Figure 44: Variation of (a) Weld Zone width (b) Depth/Width ratio of the weld zone, with welding speed

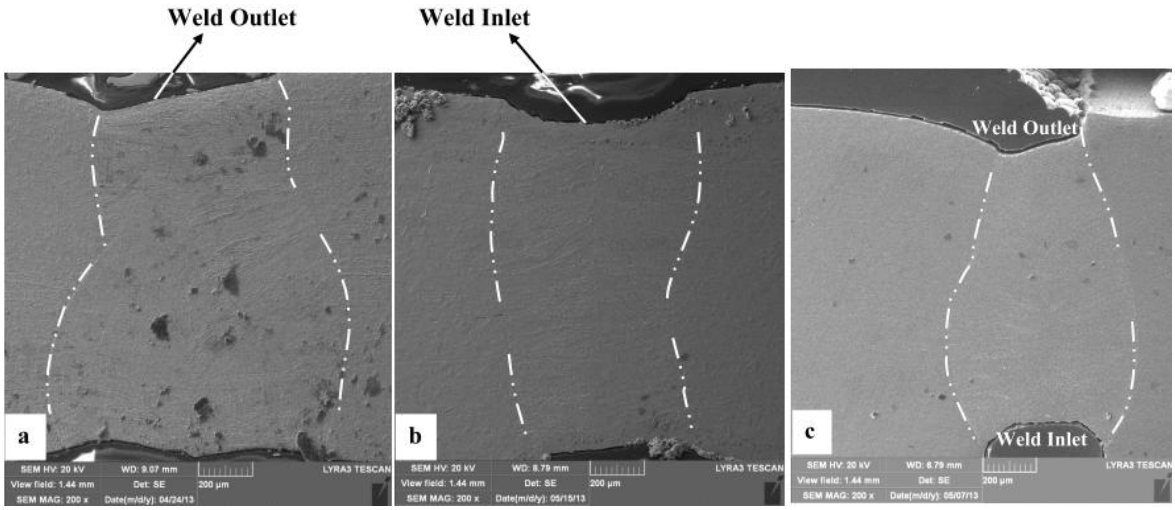

Figure 45: SEM micrograph of welded samples with varied power (a) 2kW (b) 3kW (c) 4kW

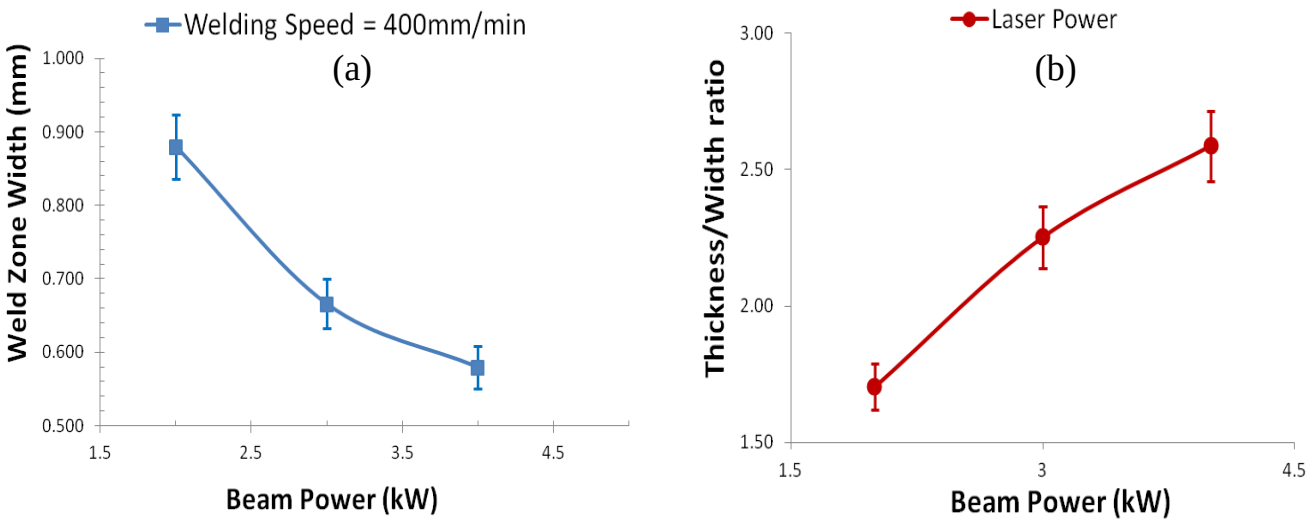

Figure 46: Variation of (a) Weld Zone width (b) Depth/Width ratio of the weld zone, with Laser Power

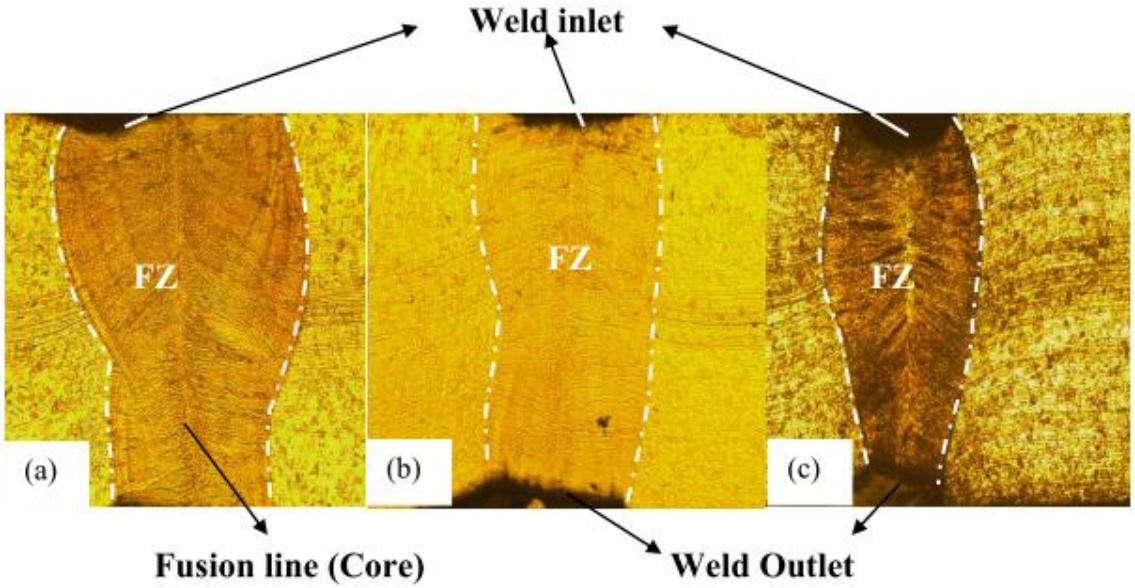

Figure 47: Optical Micrograph of the cross-section of samples welded with varied Power (a) 2kW (b) 3kW (c) 4kW (X5)
(Welding speed =400mm/min, Sample thickness = 1.5mm)

(b) Effect of laser power

Figure 45 shows the SEM micrograph of welded samples with varied laser power while other parameters were held constant (see table 5). It was observed from Figure 46 that the measured width of the welded zone decreases while the thickness/bead width ratio increases as the laser power increases. This behavior is associated to the amount of heat absorbed by the surface, solidification and cooling rates. Thereby, as the surface is irradiated with a higher power, more heat is absorbed especially at a low welding speed, leading to higher temperature gradient across the welding line. This in turn results into a higher solidification rate with a reduced weld-affected area (weld zone). Although in previous studies [8, 62], it was observed that the laser power has less significant influence on the fusion zone shape and on the depth/width ratio. But since the welding in this study was done at low scanning rate (400mm/min), it might be responsible for the significant contribution noticed. The optical images of these welded samples are shown inFigure 47 revealing clearly the decreasing nature of the weld width as the beam power increases.

(c) Effect of blank thickness

The geometrical thickness of the welded plate also influences the fusion zone size during welding as previously illustrated in [34]. Table 6 shows the blank thickness variation examined. Figure 48 shows the bead width and the thickness/bead width ratio variation with thickness, a sharp decrease in the width of the welded zone was noticed as the thickness increases from 1.5mm to 2.5mm. This is caused by the decrease in the power per bulk material which consequently decreases the peak temperature while also reducing the temperature gradient. In addition, the solidification and cooling rates thus increases thereby reducing the interaction of the affected area with the beam power which then results in the observed reduction in the bead width size. However, investigating all samples reflects that the width decrease was less significant after

2.5mm (as shown in Figure 48(a)). This could be as a result of higher thermal efficiency accompanied by increase in the thickness of the workpiece as stated in [34], which is required for a sound weld. As the thermal efficiency increases, the power per bulk material increases thereby more materials are interacted with due to the increase efficiency. Hence, the smaller the effect of the beam power on the bead width size at a large sample thickness. The optical micrograph of fusion zone shape of different thickness is shown in Figure 49 for samples welded using 4kW laser beam power at 300mm/min welding speed. The symmetry along the welding line is obvious except for some irregular enlargement noticed due to the aforementioned possible reasons.

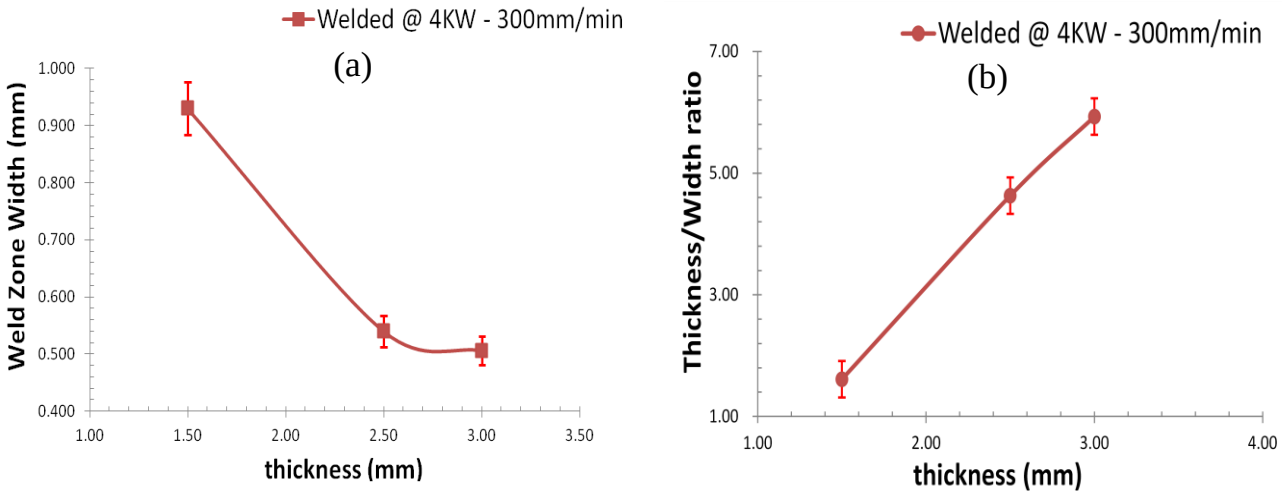

Figure 48: (a) Weld zone width and (b) Depth/width ratio variation with sample thickness

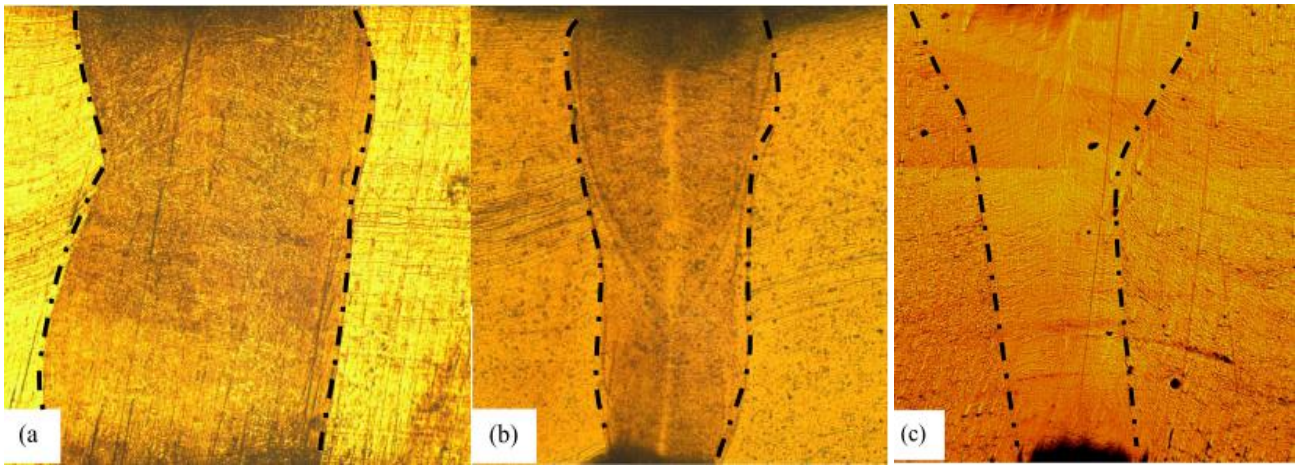

Figure 49: Optical Micrograph of the cross-section of samples with varied thickness welded with 4kW – 300mm/min (a) 1.5mm (b) 2.5mm (c) 3mm thickness (X5)

5.2.2 Microstructure of the Welded Samples

SEM micrographs showing different regions of weld cross section are obtained to analyze the post-welding microstructures. For all investigated samples, it is observed from the micrograph as shown in figures 50 and 51, that there are microstructural variations within the fusion zone. It was noticed that dendritic microstructures are formed in the near neighborhood of the fusion zone because of the relatively higher cooling rate than in the fusion zone.

The SEM micrographs in figures 51 and 52 show clearly the fusion and heat affected zones respectively. The weld section displays both cellular and dentritic microstructures, which contains the austenitic phase. This behavior is primarily due to variation in the solidification rate and temperature gradient across the fusion zone. The solidification rate is lowest (almost zero) along the fusion boundary (boundary between solid-liquid interface during welding) and maximum along the centerline due to its high temperature and very low temperature gradient. As the solidification process moves towards the fusion boundary, the temperature gradient decreases, while the solidification rate increases. This variation in temperature gradient and solidification rates towards the center line result in an increased tendency toward cellular growth, i.e., a transition from planar to cellular growth occurs, resulting in columnar grains that are noticed close and around the center line. Further towards the centerline, there are increase reduction in the temperature gradient and increases in the solidification rate. This results in subsequent transition of some of the cellular structures to dendritic structures around the centerline in the fusion zone. However, the absence of microcracking during solidification of the fusion zone and fusion boundary indicates that the solidification strains are well below the ductility of the weld material.

The HAZ of the welded samples were also examined using the SEM. The grain coarsening in the HAZ due to self annealing as a result of high temperature and low cooling rate is clearly depicted in figure 53. Moreover, in the neighborhood of the heat affected zone and fusion zones, the partial decomposition of the ferrite takes place through the growth of the austenite phase in line with Widmanstatten-type mechanism inside the ferrite grains. Figure 50-1 is the X-ray diffractogram of the welded surface. It is observed from the x-ray peaks that δ–Fe and γ-Fe are present. This is attributed with the high cooling rates at the surface, due the incomplete transformation of the δ- and γ-phases and metastable δ–Fe phase.

Effect of the welding speed on the microstructure was also examined. It was noticed that the microstructure becomes finer as the welding speed increase as evident from figure 54. This is due to increase in the solidification and cooling rates due to less heat input which is a consequence of the increase in welding speed.

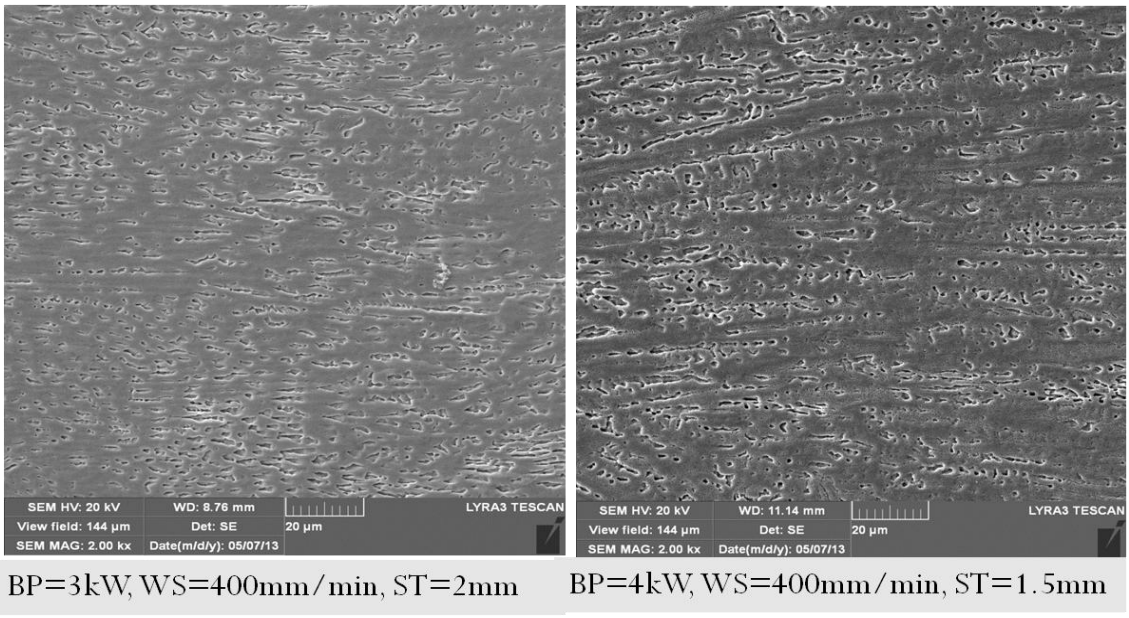

Figure 50: SEM cross-section at the neighborhood of HAZ

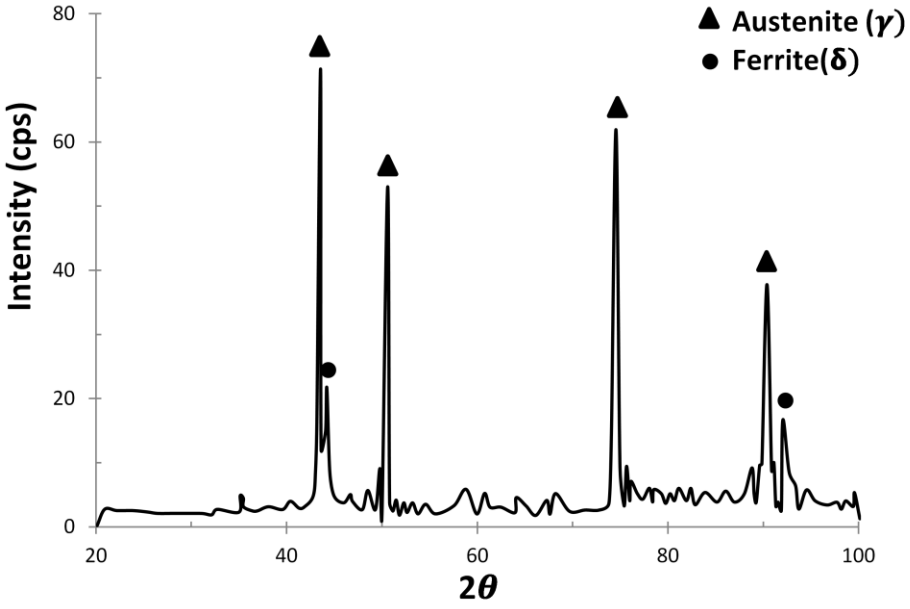

Figure 50-1: XRD diffractogram

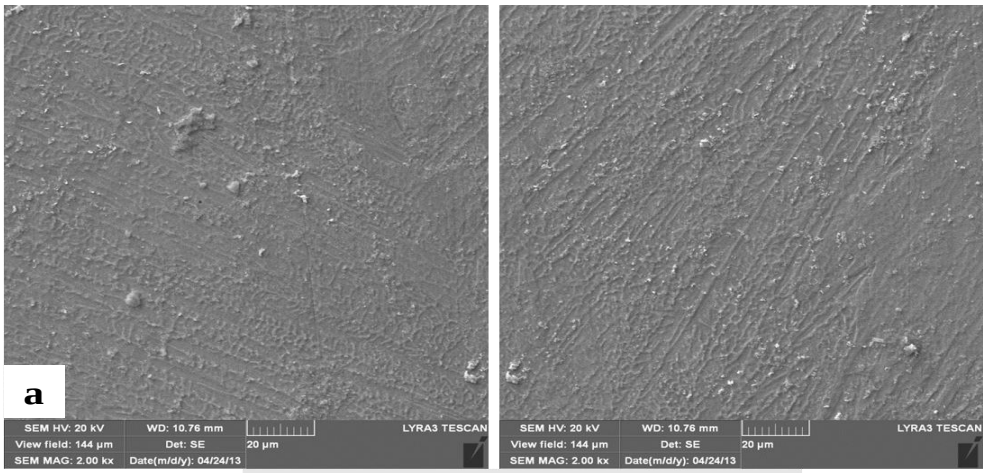

BP=3kW, WS=200mm/min, ST=1.5mm

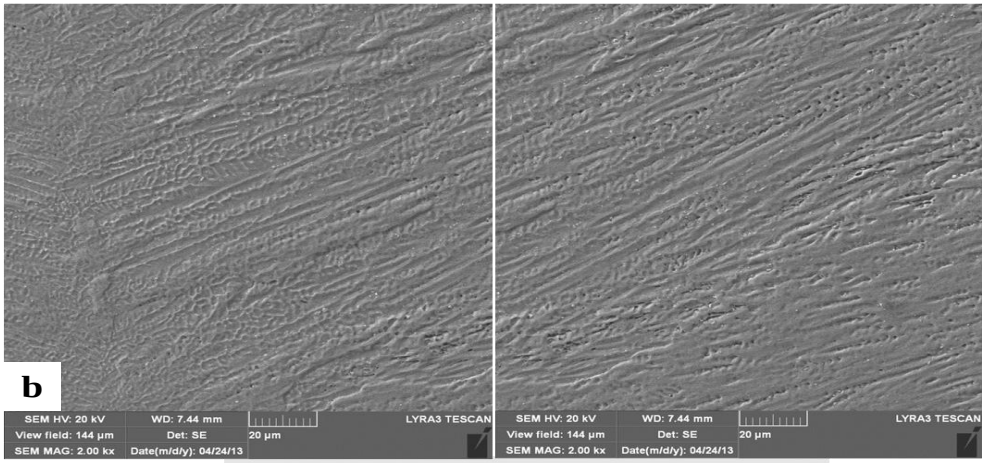

BP=3kW, WS=300mm/min, ST=1.5mm

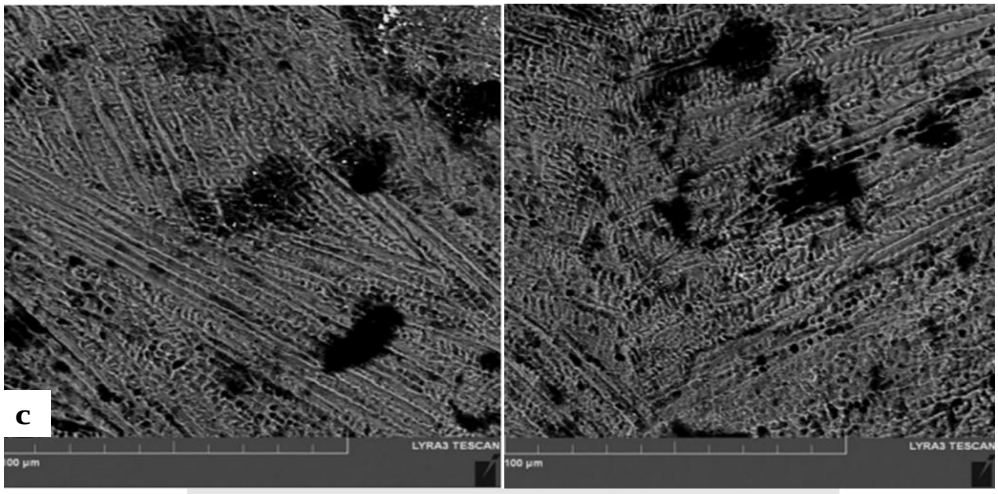

BP=2kW, WS=400mm/min, ST=1.5mm

Figure 51: SEM cross-section across the weld zone from (a) to (c) showing both the columnar and dentritic microstructures

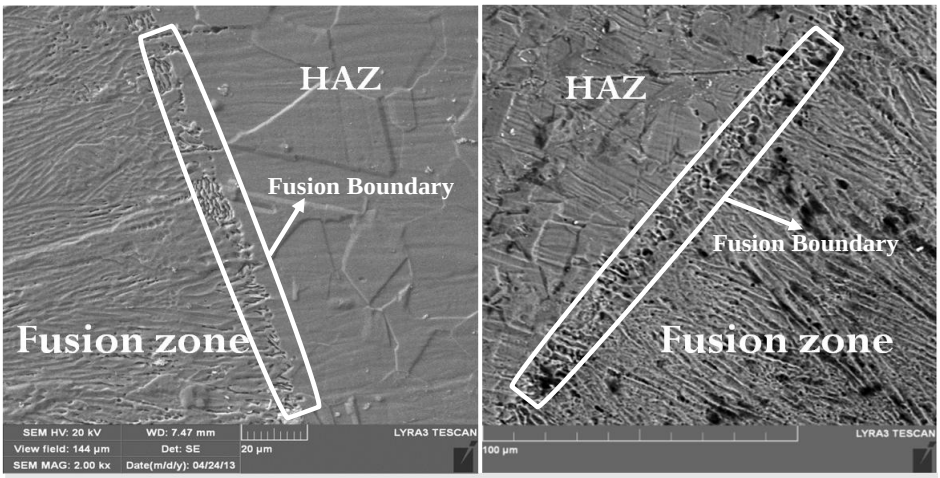

Figure 52: SEM micrograph showing fusion boundary and HAZ of welded samples

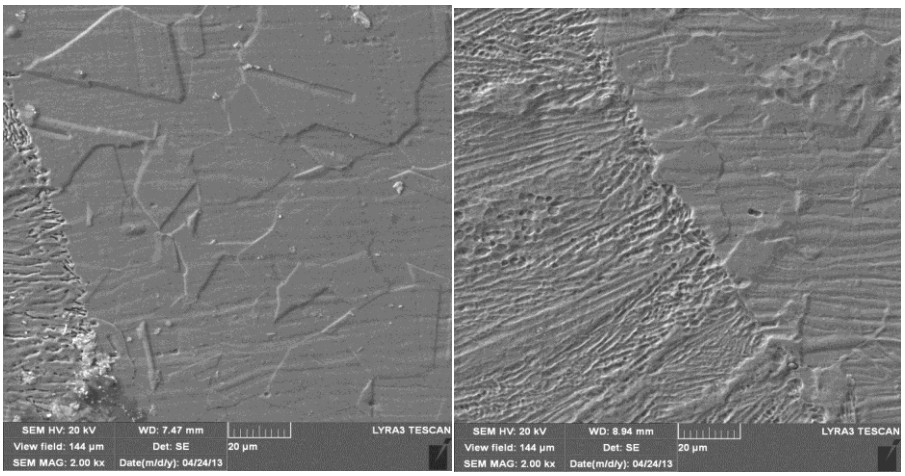

Figure 53: SEM micrograph of showing grain coarsening in HAZ of welded sample

The microstructure of welded samples with different laser beam power indicates grain coarsening with an increase in laser output power (figure 55). This is also due to increase in the heat input subsequent to increase in the beam power which decreases the cooling and solidification rates. In addition, more heat input also favors grain growth which is attributed to the coarse nature of the microstructure at an increased beam power.

The effect of the thickness on the microstructure is shown in figure 56. The microstructure of the samples becomes coarser as the thickness of the blank increases possibly because the thermal efficiency increases as the blank thickness increases due to higher heat absorption rate. This consequently causes a higher temperature gradient and decreases the solidification rates, hence the resulting coarse microstructure at a higher sample thickness.

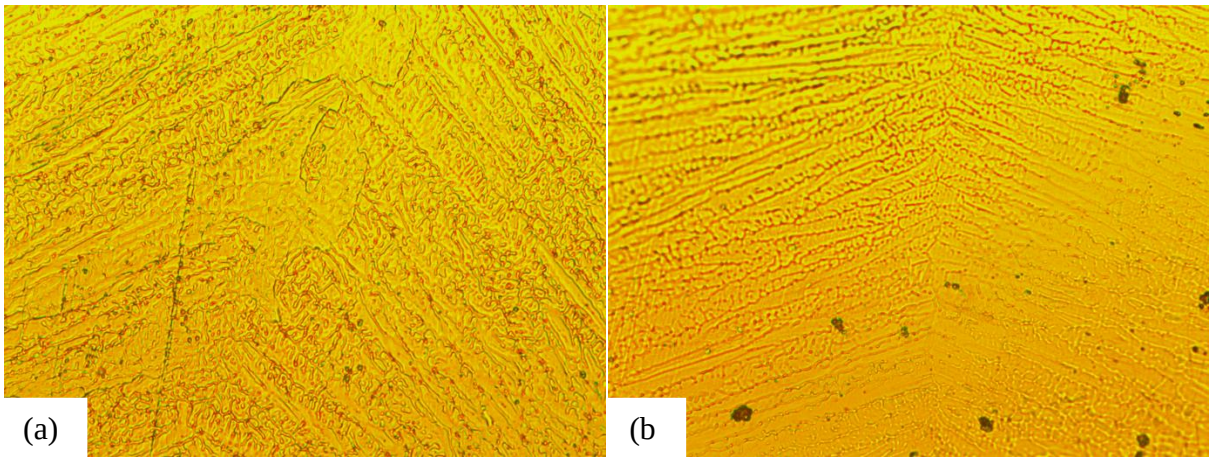

Figure 54: Microstructure of laser welded samples at 3kW laser power at different welding speed: (a) 200mm/min (b) 400mm/min (X50)

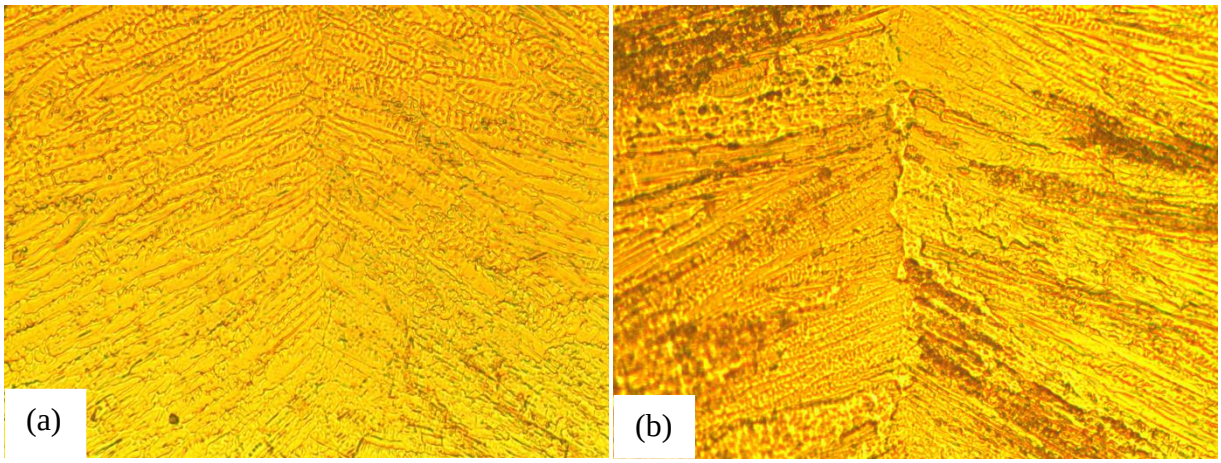

Figure 55: Microstructure of laser welded samples at 400mm/min welding speed with different laser power: (a) 2kW (b) 4kW (X50)

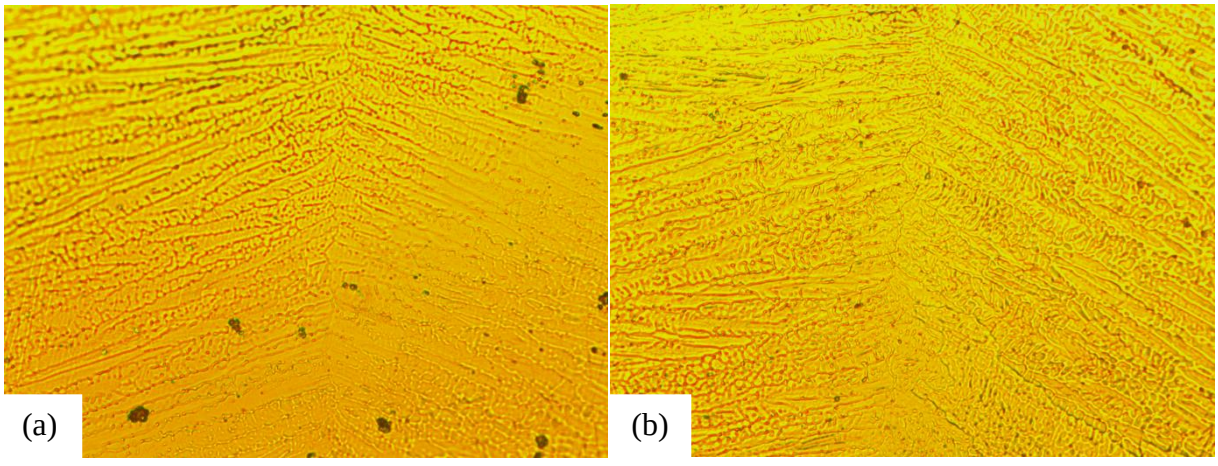

Figure 56: Microstructure of laser welded samples using 4kW beam power and 400mm/min welding speed with different blank thickness: (a) 1.5mm (b) 2mm thick (X50)

5.3 MICROHARDNESS OF WELDED SAMPLES

The microhardness distribution of the fusion zone was conducted using the Vickers HV (300g) microhardness testing machine. To account for possible errors, all measurement were express in the form $\bar{a} \pm s$ where $\bar{a}$ is the average value of three hardness measurements recorded for a given location and s is the standard deviation within the readings. Figure 57 shows the microhardness distribution of three welded samples across the fusion zone (FZ). Locations 5, 6 and 7 are on/around the fusion or center line; locations 3 and 10 were within 5μm from the fusion boundary into the fusion zone from both sides, locations 4, 8 and 9 were between the centerline and the fusion boundary on both sides, while other locations are on the base material. The hardness drops rapidly from the fusion boundary towards the fusion line for all samples investigated. The peak hardness is about 15% higher than the base metal (BM) hardness. This corresponds to the microstructural formation across the FZ, they consist of majorly fine microstructures.

Parametric effects on the microhardness were also investigated. Figure 58 and Figure 59 are histograms showing the variation of the microhardness with welding speed and beam power respectively. It is noticed that there no significant difference in the hardness of the FZ for the range of welding speeds investigated. However, the HAZ hardness is always lower than that of the BM while the increasing reduction in cooling rate at higher welding speed results in the slight reduction in the HAZ hardness with welding speed. Beam power has noticeable significant on the hardness. In addition, the BM hardness is seen to exceed the HAZ hardness in most of the hardness measurement; this is due to the tempering that occurs at the HAZ during the welding process. The hardness variation with sample thickness is shown in Figure 60. The hardness relatively decreases as the sample thickness increases; this behavior is due to the amount of heat

per mass density in the sample which plays an important role in the microstructural development at the fusion zone and the HAZ. It should be noticed that tempering at the HAZ necessitates the reduced hardness and it effect decreases with sample thickness which results in the higher hardness noticed for the sample with 2.5mm thickness.

In general, the microhardness falls between 198 HV and 211 HV for the fusion zone (FZ), between 186 HV and 199 HV for the heat affected zone (HAZ) and between 191 HV and 200 HV for the base metal (BM) for all samples investigated in this study. This illustrates that the welded joint has an improved mechanical property as compared to the base material; however, the high hardness in the FZ is attributed to both fine microstructure and the inherent stresses developed during welding process.

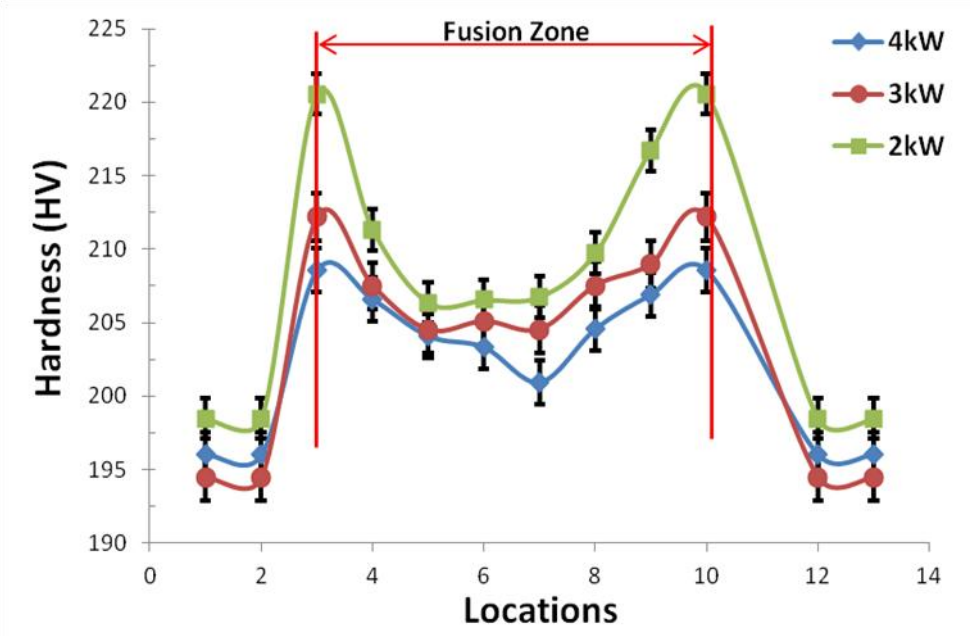

Figure 57: Microhardness at different locations across fusion zone (welding speed = 400mm/min, Sample thickness = 1.5mm)

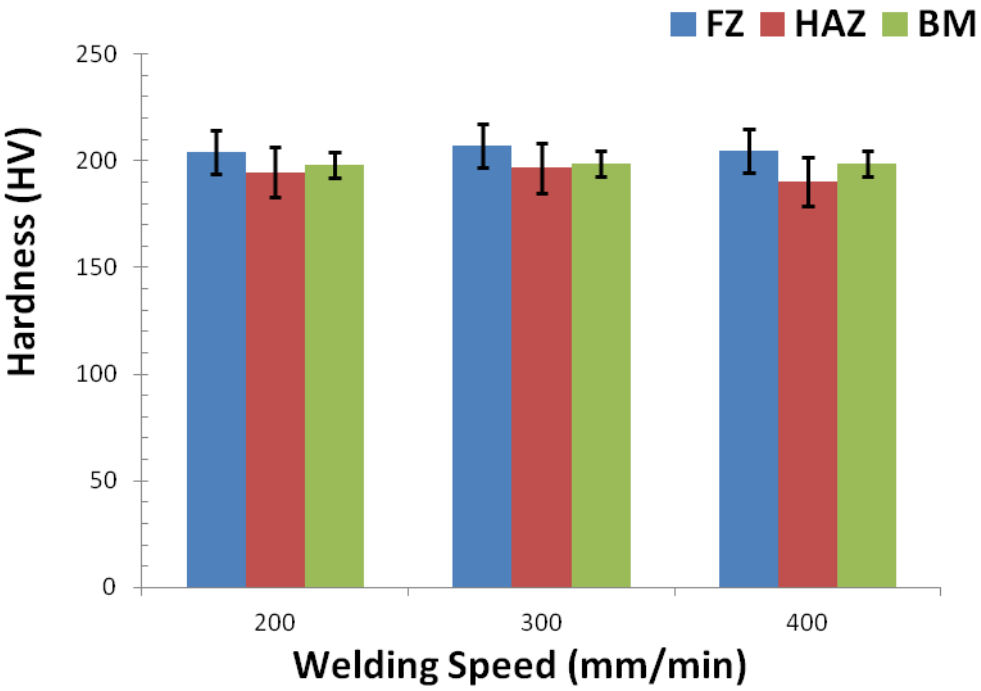

Figure 58: Vickers Micro-Hardness variation with Welding Speed for the FZ, HAZ and BM (BP=3kW & ST = 1.5mm)

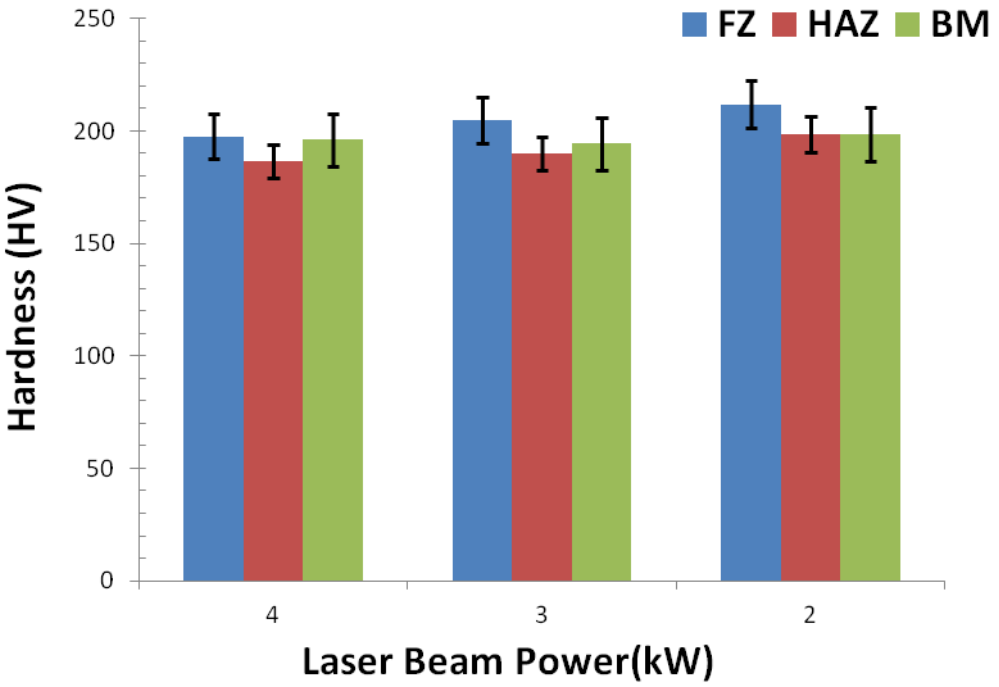

Figure 59: Microhardness variation with Beam Power for the FZ, HAZ and BM (WS = 400mm/min & ST =1.5mm)

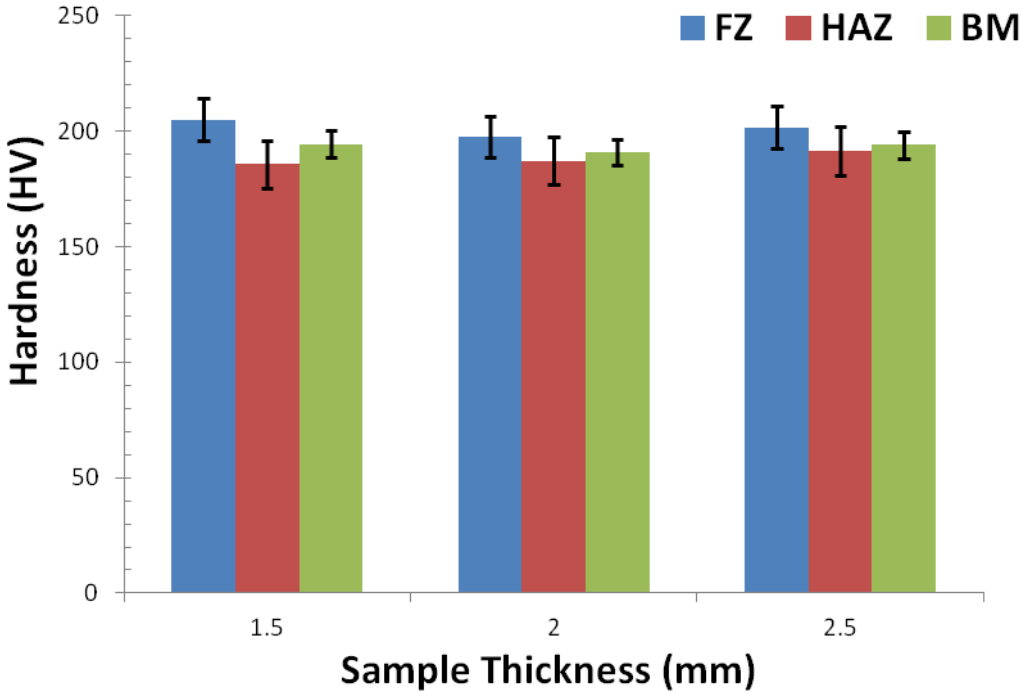

Figure 60: Vickers Micro-Hardness variation with Sample Thickness for the FZ, HAZ and BM (BW =3kW & WS = 400mm/min)

5.4 SIMULATION RESULTS

5.4.1 Thermal Analysis

The simulation of the temperature fields during laser welding were conducted using the heat source model described in section 4.1.3. Finite Element Software ANSYS 14.0 was used to perform the simulation. Heat flux is applied on element faces to simulate the moving heat source; this was achieved by using the ANSYS Parametric Design Language (APDL) module available in ANSYS software. When the current load is shifted to the next load step the previous one is deleted. Figure 61 shows the flowchart of the APDL module. The simulations were conducted with four different workpiece thicknesses while varying the beam power and welding speeds for each model. Three different beam powers and four welding speeds were considered during the simulation process. Figure 62 shows the temperature field on the workpiece at four different load steps during the welding process for one of the welding conditions: 2000W beam power and 200mm/min welding speed. It is observed that there is high temperature field along the welding direction and it also shows the cooling of the workpiece away from the heat source.

Temperature gradients during laser welding are usually very large, this is due to the high beam power density and the localized heating nature of laser beam[40]. Figure 63 shows the high temperature gradients across the weld line during the laser welding using 2000W beam power at 200mm/min welding speed. It can be seen clearly that the temperature is symmetrically distributed across the workpiece and it decays sharply in the surface region, and as the depth below the surface increases temperature decay becomes sharp and further increase in the depth results in gradual decay of temperature. The rapid temperature decrease to ambient temperature on the surface indicates a highly localized heating zone within a range of 1.52mm.

The heat source temperature of the top element reaches a temperature much above the melting temperature of 316L ASS; which is between 1371 – 1400^0C[64, 65]. Elements that reach a temperature above the melting temperature of the material is melted leading to the formation of molten pool which results in the formation and shape of the fusion zone. It is noticed that the shape of the molten pool is elliptical. We thus measured the weld bead width at the intercept of 1399^0C isotherm from the temperature field across the weld line plots. Figure 64 shows the temporal variation of temperature at different position along the weld line (*z*-axis) during the welding process, in which it can be seen that except for the temperature histories at start/end of weld location, the other three temperature histories at 5mm, 11mm, and 17mm locations along z-axis has similar profile. The temperature increase as the laser source progress along the z-axis is attributed to the pre-heating effect experience by the material ahead of the rear molten pool. The maximum temperature on the top surface is about 3700K during the welding with 3000W laser power at 300mm/min welding speed.

(a) Effect of Welding Speed on the weld bead width and temperature field

Figure 65 shows temperature profiles in the substrate material; it shows the effect of laser welding speed on temperature distribution. As the welding speed increases the narrower the temperature profile becomes. This is also illustrated in the temperature-distance plots across weld line in Figure 66. It found that the weld bead width is 0.82 ± 0.01, 0.52 ± 0.02, 0.36 ± 0.02 and 0.27 ± 0.01 for 200mm/min, 300mm/min, 400mm/min and 500mm/min respectively. This is behavior results due to the fact that as the welding speed increases for the same amount of beam power, the lesser the exposure time of the sample to the laser beam, which consequently means lower heat input. Therefore, the participating materials in forming the fusion zone reduces since small region is melted by the heat input.

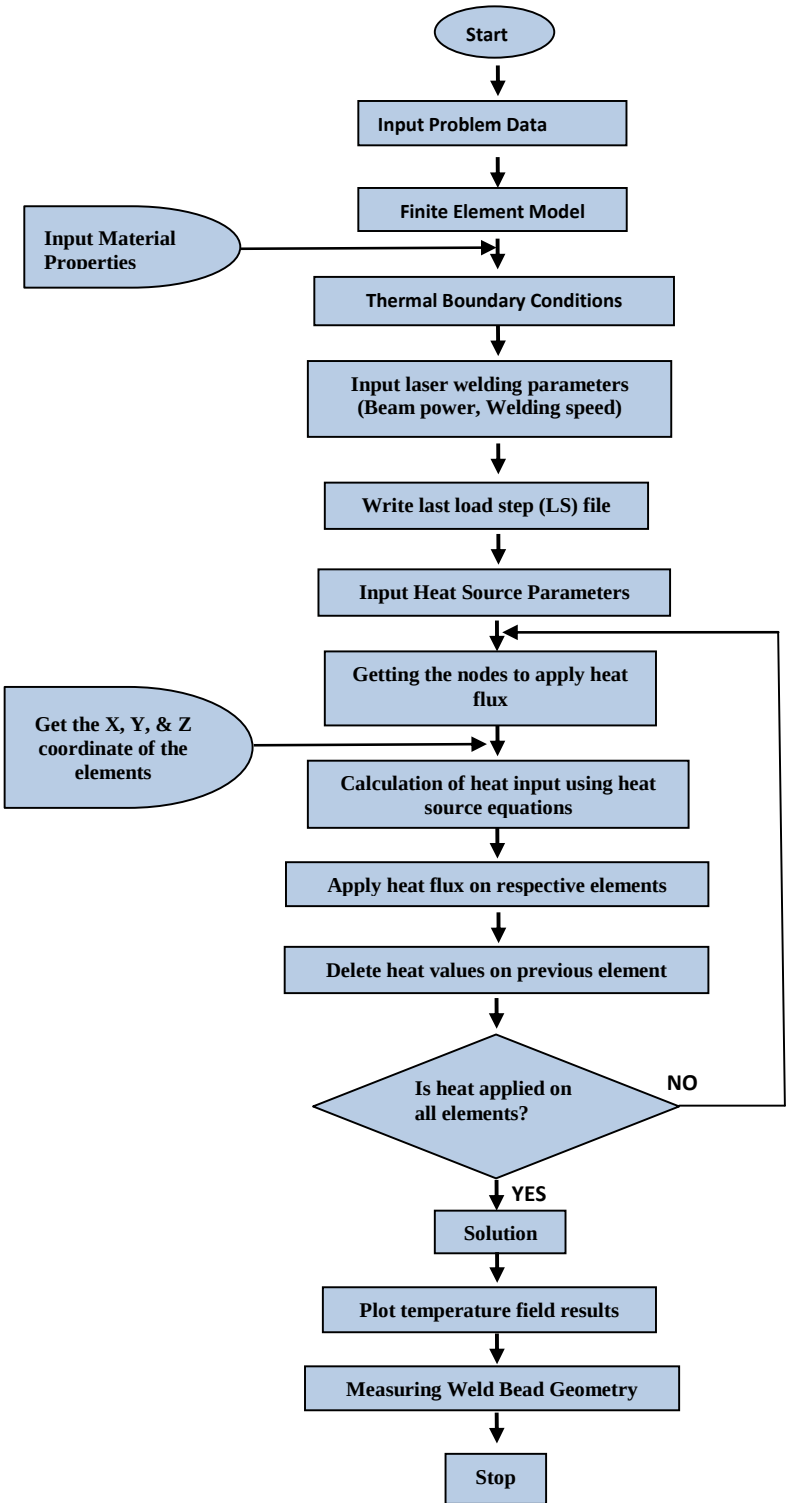

Figure 61: Flowchart of the APDL module for the thermal analysis

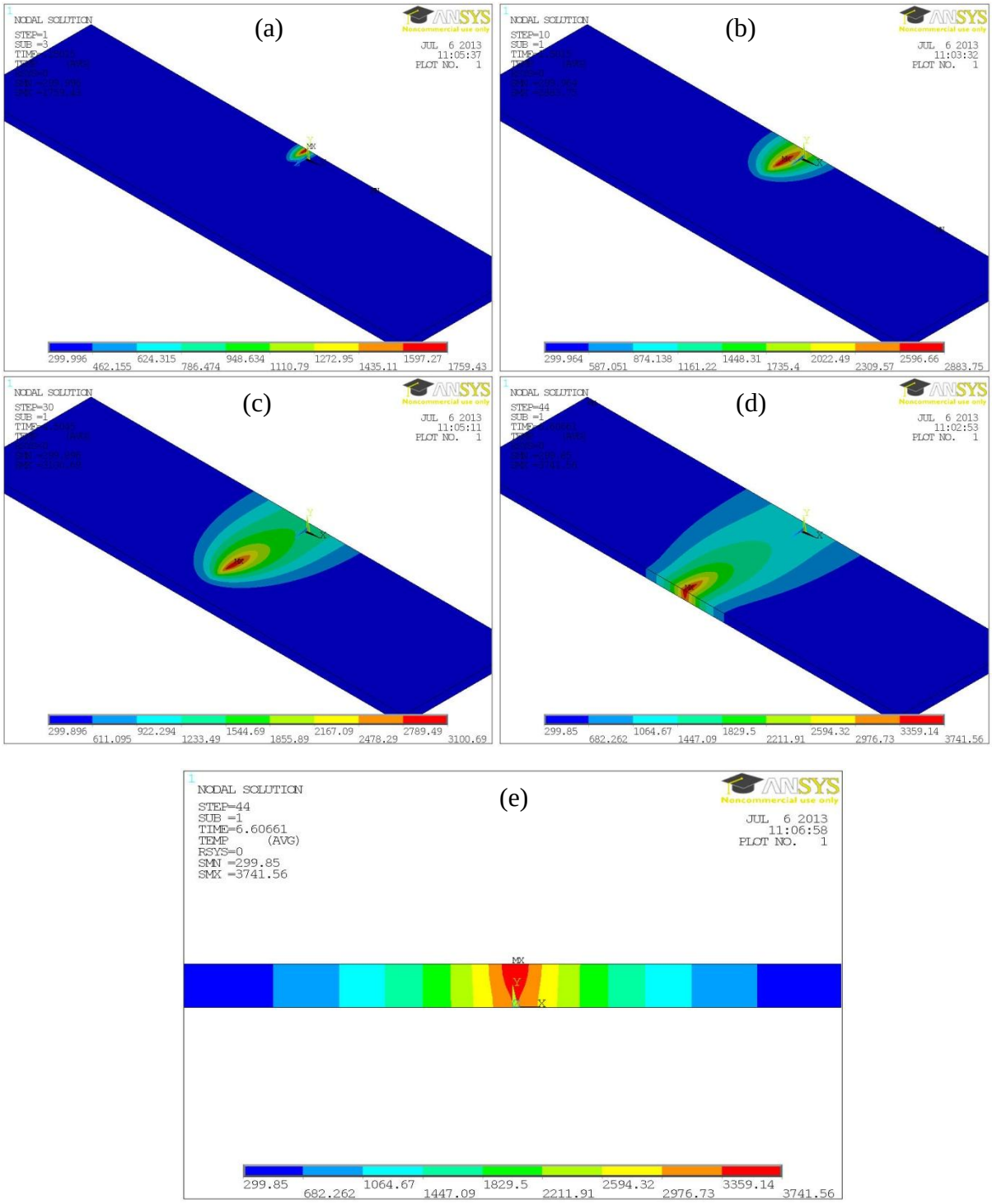

Figure 62: Temperature field for workpiece welded with 2000W at 200mm/min at different load steps

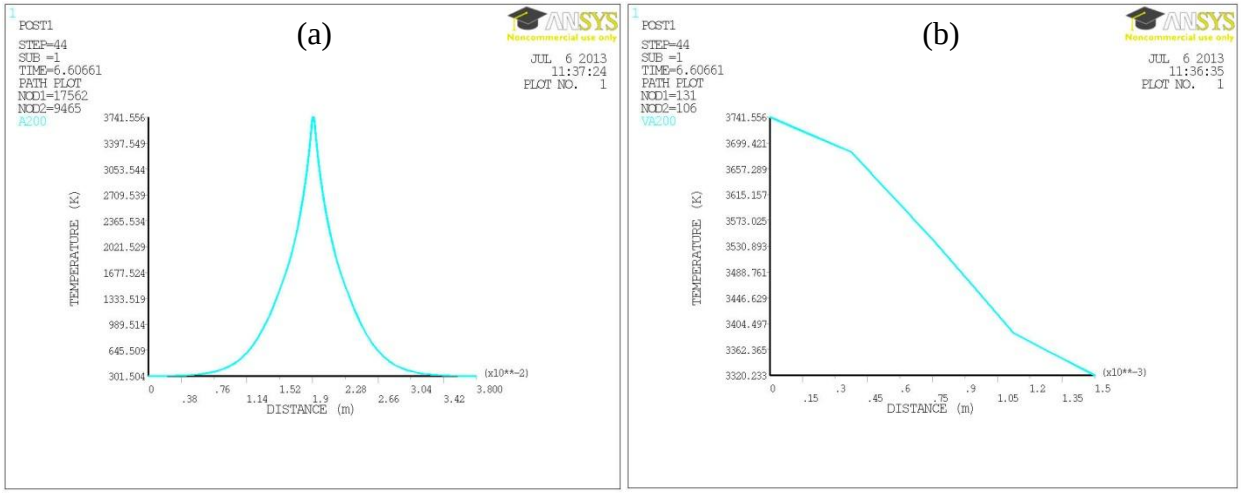

Figure 63: Temperature profile (a) across weld line (radial direction) (b) along the thickness (depth), for beam power 2000W at 200mm/min welding speed

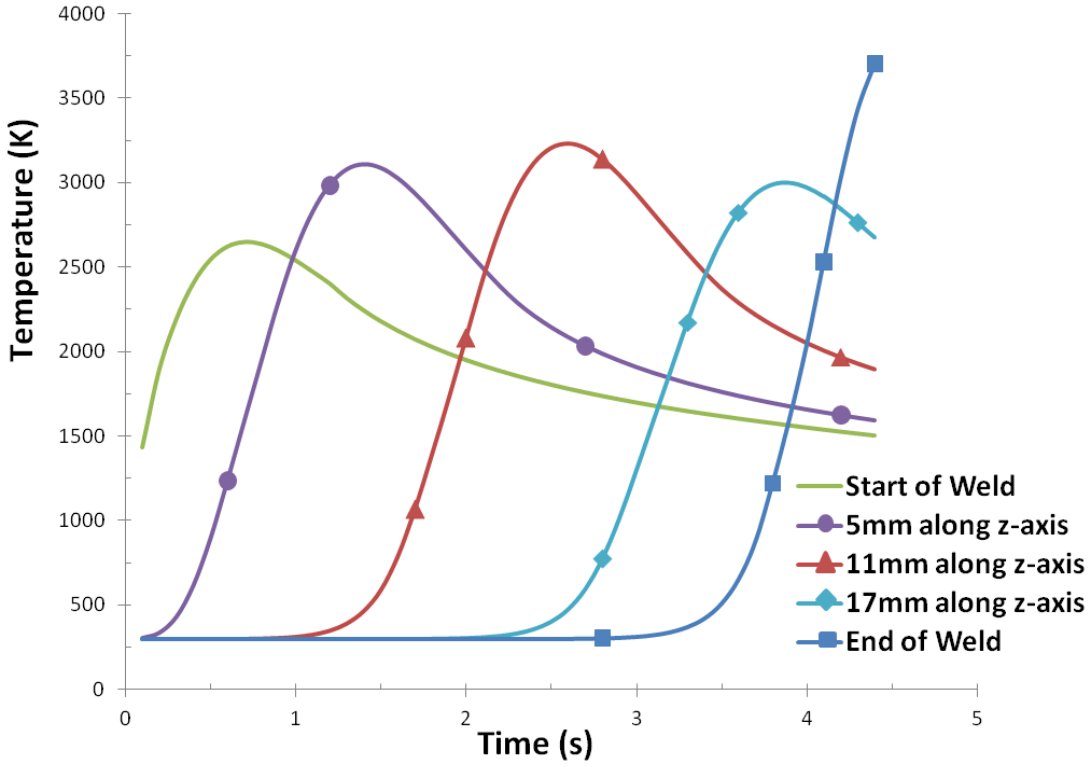

Figure 64: Temperature histories at the weld center on the top surface for sample welded with 3000W at 300mm/min

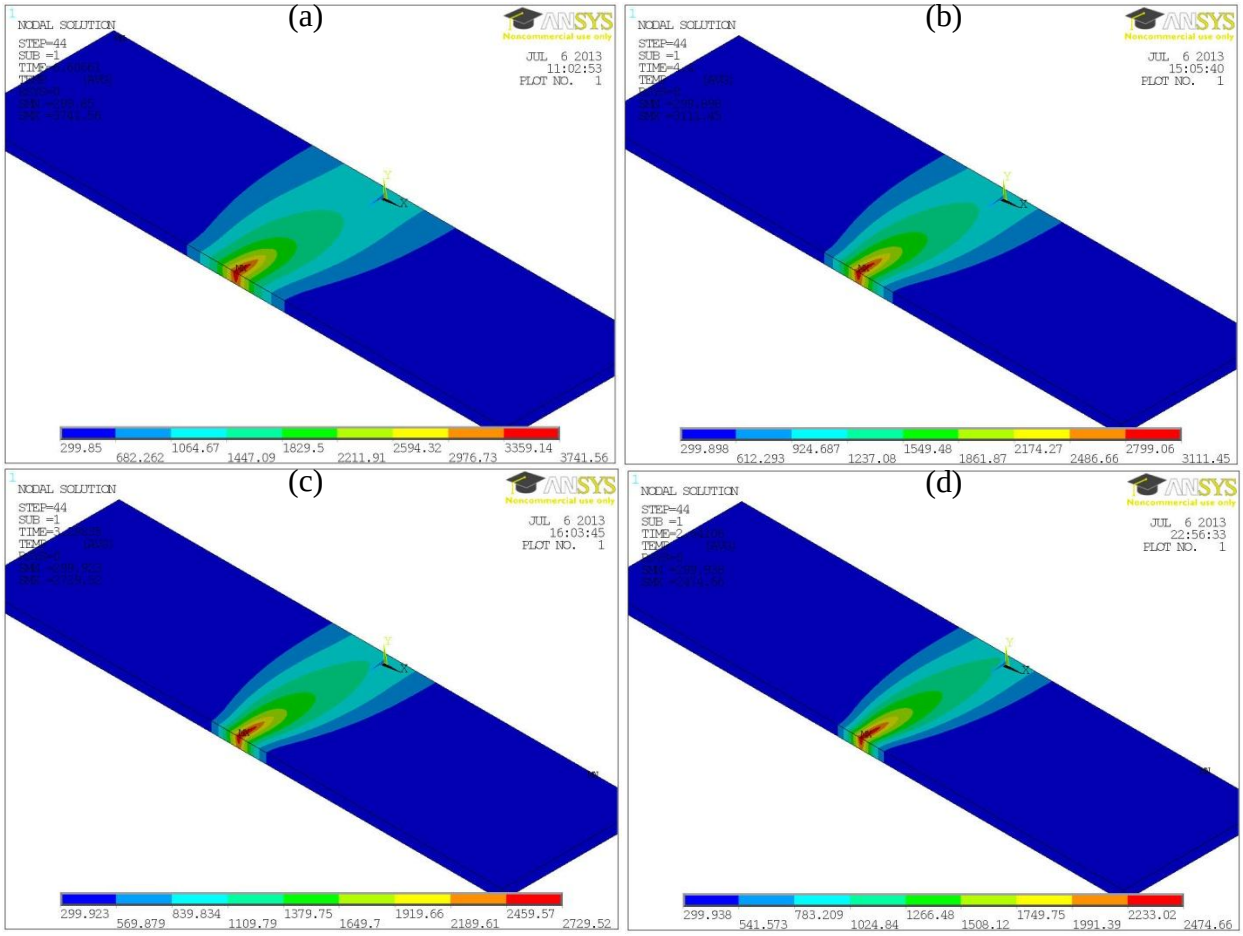

Figure 65: Temperature profile plots with 2000W beam power at welding speeds; (a) 200mm/min (b) 300mm/min (c) 400mm/min (d) 500mm/min

(b) Effect of Laser Power on the weld bead width and temperature field

Figure 67 shows the temperature distribution for different beam power welded at 400mm/min welding speed. The profile shows a wider temperature field as the laser beam power increases. This is so because as the beam power increase at the same welding speed, the workpiece absorbed more heat hence there is an increase in the conduction and interaction rate between the workpiece and the absorbed heat. Figure 67(d) shows the temperature-distance plots across the

weld line for the different power; the bead width from the 1399^{0}C isotherm were 0.77mm$\pm$0.03, 0.54mm$\pm$0.03 and 0.42mm$\pm$0.03 for 4kW, 3kW and 2kW beam power respectively.

(c) Effect of Sample Thickness on the weld bead width and temperature field

The effect of sample thickness on the temperature distribution is shown in Figure 68. The important variation is in the lateral distribution of the heat and the maximum temperature attained for the different thickness despite being welded with same welding parameters (Laser Power = 2000W, Welding Speed = 200mm/min). This variation results due the difference in energy absorbed per volume by each sample. As sample thickness increases the energy absorbed along depth direction (y-axis) increases, this consequently reduces the lateral distribution of the heat and hence the noticed reduction in the weld bead width with sample thickness.

5.4.2 Comparison of Experimental and Simulation Results

The validation of simulation results are done by comparing the bead widths calculated from simulation and bead widths measured from the SEM micrographs. Figure 69 andFigure 70 show the compared results for different welding speeds and laser beam powers respectively. As clearly shown in these figures (Fig. 69 & 70), the trends of the simulation results are in good agreement with that of the experiment with about 16% maximum percentage difference. This small discrepancy occurs because of the assumptions made in the simulations such as uniform structure, material properties considered and the irregularity of the actual weld bead width as observed from micrographs. However, the validated values are still within acceptable range.

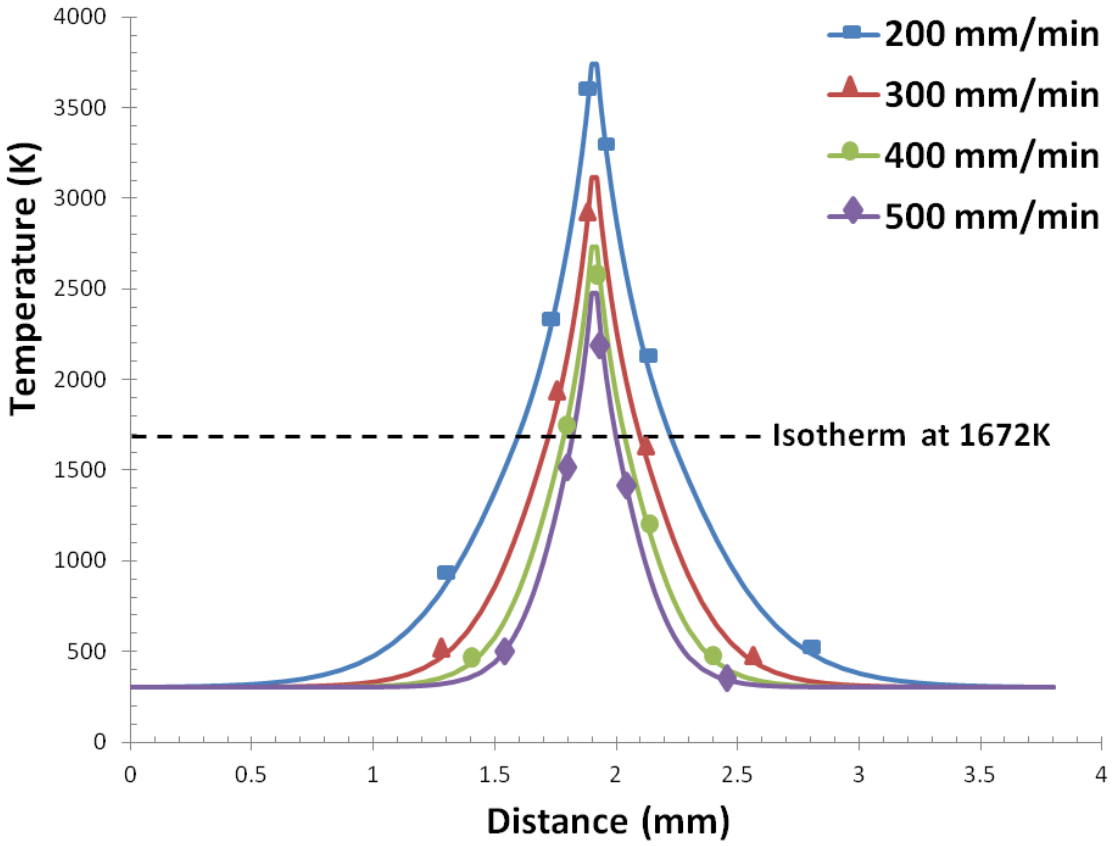

Figure 66: Temperature profile across weld line (radial direction) with 2000W beam power at different welding speed

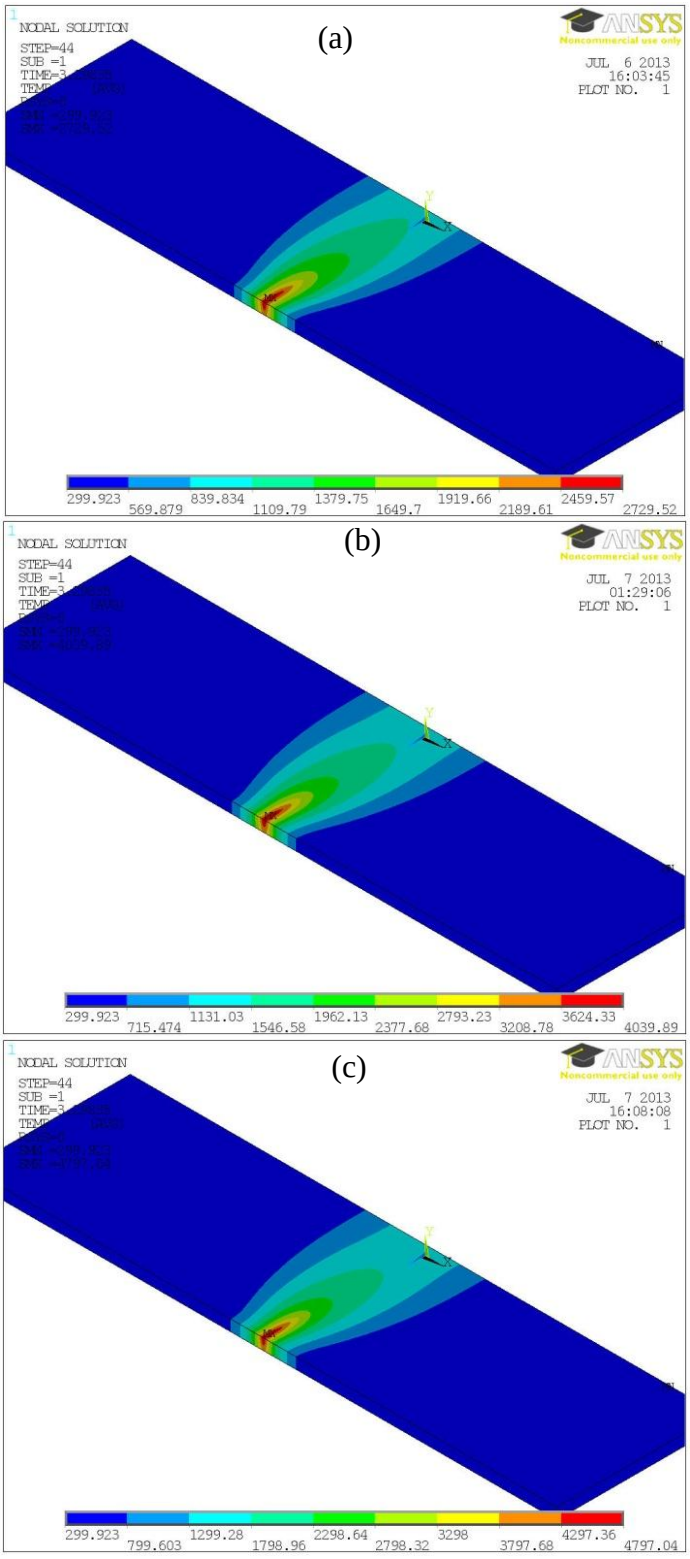

Figure 67: Temperature profile plots for workpiece welded at 400mm/min welding speed with different beam power; (a) 2000W (b) 3000W (c) 4000W (d) the temperature profile across weld line (radial direction) of a – c

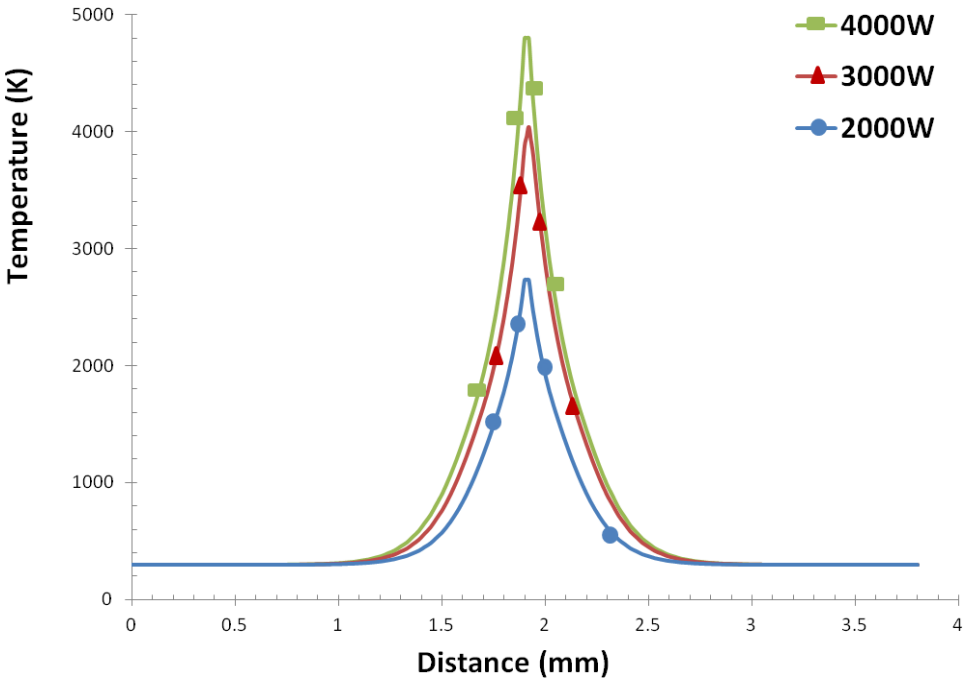

Figure 67 (Continue)

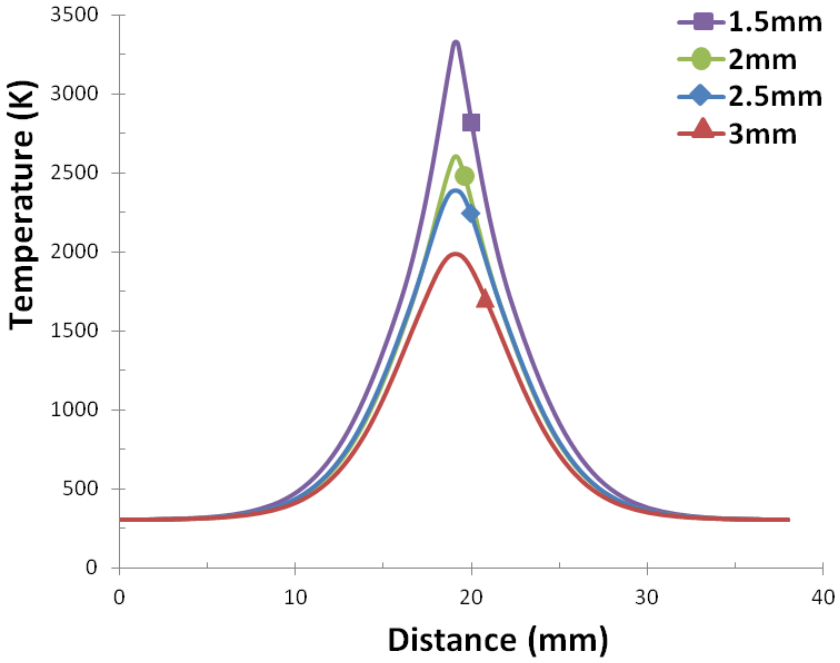

Figure 68: Temperature Profile variation with sample thickness welded using; Laser Power = 2000W, Welding Speed = 200mm/min

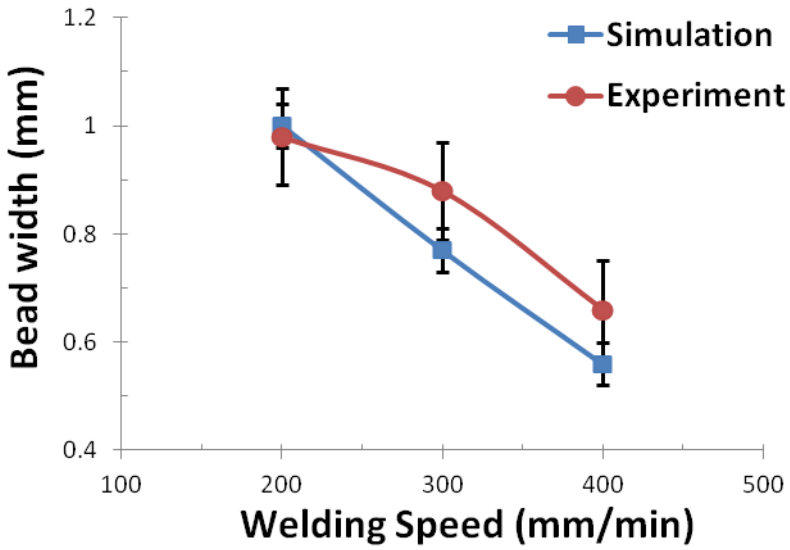

Figure 69: Comparison of the bead widths from simulation and experimental results for different welding speed

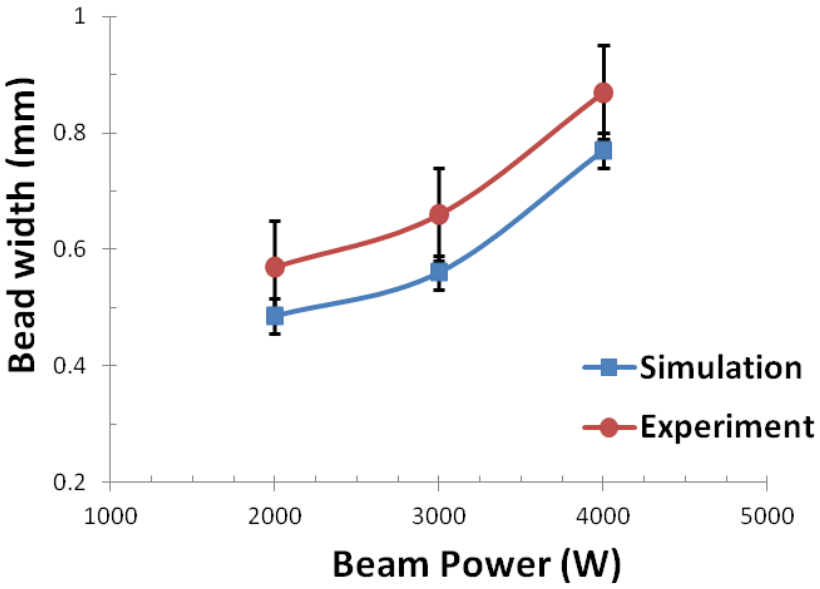

Figure 70: Comparison of the bead widths from simulation and experimental results for different beam power

5.4.3 Structural Analysis

A sequential-coupled analysis was adopted for the transient structural analysis during which the thermal results were inputted as body loads into the structural part. Figure 71 is a flow chart showing the sequence of modeling of the structural part of the simulation.

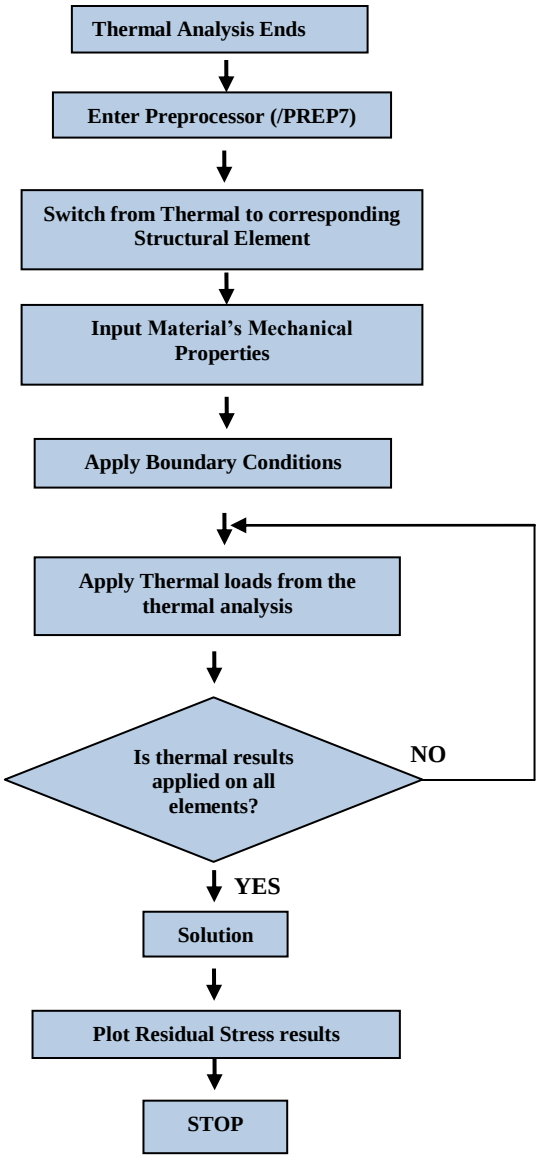

Figure 71: Flowchart of the Structural analysis

Non-Linear Transient Structural Results

The Von Mises Stress plots for samples welded using 3000W power at different welding speed is shown in Figure 72. The noticeable difference is in the distribution of the stresses as could be observed; the area with high stresses gradually increases with the welding speed. Also observed is the longitudinal and transverse shrinkage culminating in the bulging along the centerline. Figure 73 depicts the longitudinal stress distributions along the x-direction for sample welded with 2000W power at 300mm/min welding speed. High tensile stresses occur in regions near the weld due to a resistance contraction of the material as cooling commences, while compressive stresses dominate regions away from the weld line. In this case, the maximum stress value is about 180MPa, not up to 80% of the material's yield stress. Figure 74 shows the transverse stress field along the z-direction for sample welded with 2000W laser power at 300mm/min welding speed. The distributions of this stress are symmetrical along the weld line of the plate. In general, the tensile stresses occur within the fusion zone and the compressive stresses are in the bulk material. However, the magnitude of tensile stresses exceeds the compressive stresses for all samples investigated.

The effects of welding parameters on stresses

Due to the importance of stress evaluation to structures and manufacturers, the effects of welding parameters on the Von Mises stresses developed are hereby examined;

(a) Effect of welding speed on the Von Mises Stress

Figure 75 and Figure 76 show the variation of longitudinal stresses along the x-direction and transverse stresses along the z-direction with welding speed respectively. It is observed that as the welding speed increases, the stresses (tensile) near the weld also increase while the stresses (compressive) in the bulk material from the area near the fusion zone gradually decreases

towards both sides of the sample. This is because as the welding speed increases from 200mm/min to 500mm/min during welding, the heat absorption rate by the surface decreases. This consequently tends to limit the flow of material around the weld line due to the lesser dwell time of heat source; this account for the increase in the tensile stresses. In addition, the peak compressive stresses tend to rise with the welding speed. This can also be explained that since the portion that experiences material flow with increased welding speed is relatively small compare to that of lower welding speed, the stresses at the remaining portion of the workpiece could relatively be widely distributed, hence the reduction in the overall compressive stresses.

(b) Effect of Laser Power on the Von Mises Stress

The influence of laser power on the stresses is shown in figures 77 and 78 for the longitudinal and transverse stresses respectively. The stresses were plotted for 2000W to 4000W beam powers for similar welding speed (500mm/min). The significant variation with the beam power is in the compressive stress which gradually increases with laser power. This behavior is due to the increase in energy dissipation at higher laser power, which results in more material flow within the welded region. Therefore, the bulk material compressive stress tends to rise relatively due to tensile effect at the molten region and peak compressive stresses are found close to the fusion boundary being the most heat affected area of the bulk material. Though, the tensile stresses where almost similar rather than increase, and symmetrical around the weld for the tested samples with same welding speed. Nevertheless, the tensile stresses exceed the compressive stresses in all samples investigated as earlier noticed. The transverse stress of samples welded with a welding speed of 500mm/min approach the yield stress of the material for all laser beam power studied and the maximum Von Mises stress was about 285MPa for all sample investigated which still below the material's yield strength.

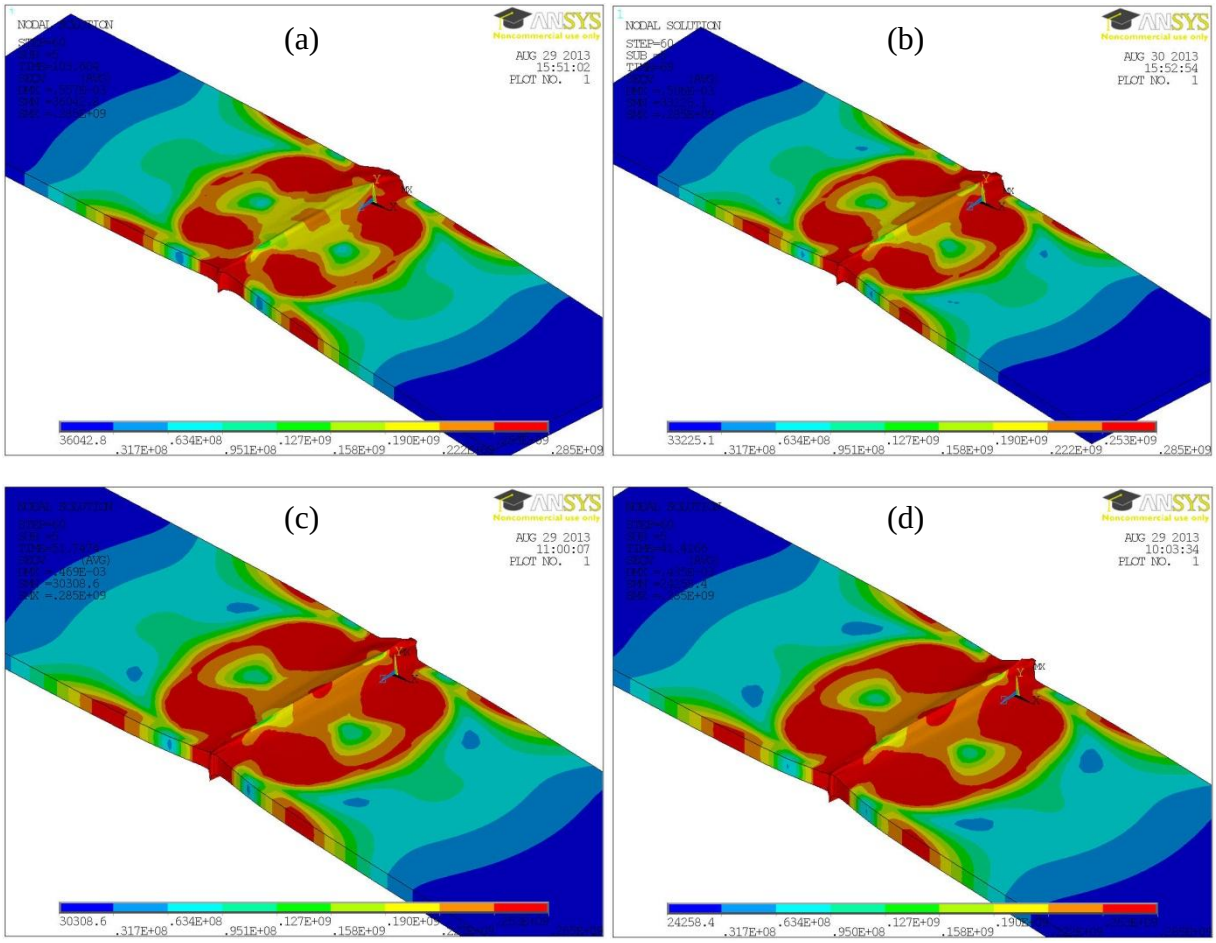

Figure 72: Von Mises Stress plot for samples welded using 3000W power at different welding speed (a) 200mm/min (b) 300mm/min (c) 400mm/min (d) 500mm/min

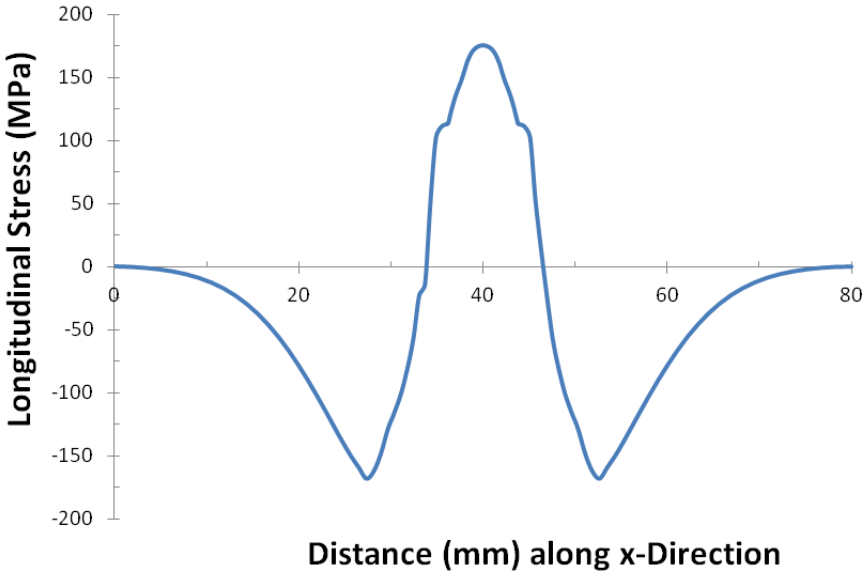

Figure 73: Longitudinal Stress distributions along the x-direction for sample welded with 2000W power at 300mm/min welding speed

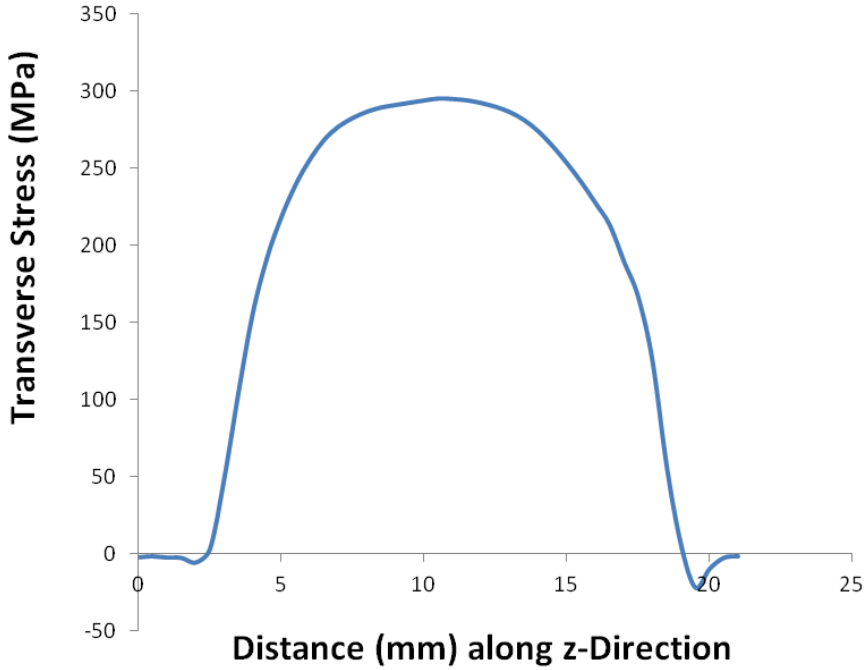

Figure 74: Transverse Stress distributions along the z-direction for sample welded with 2000W power at 300mm/min welding speed

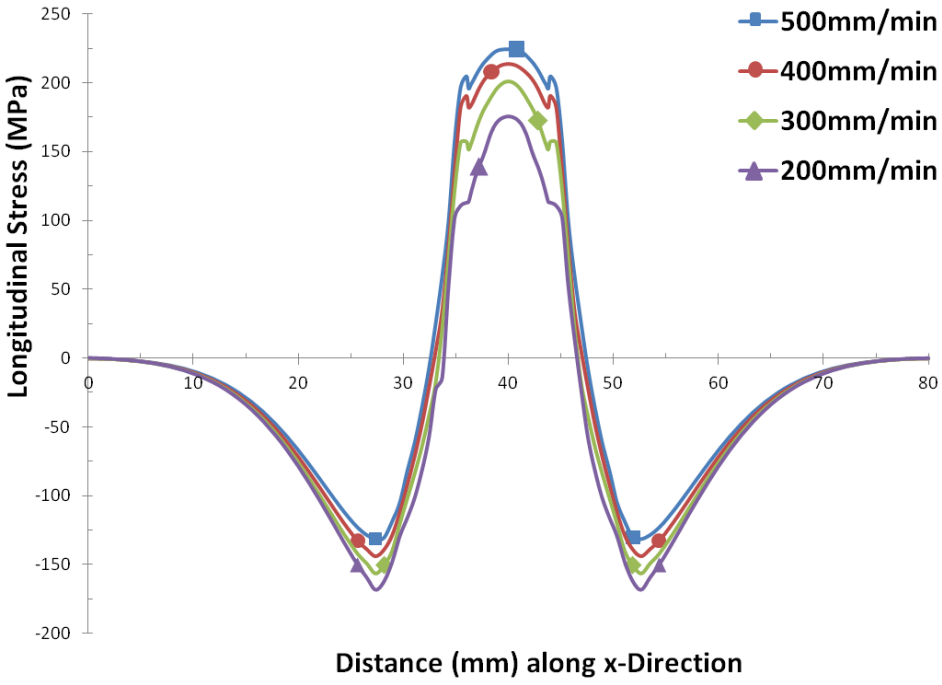

Figure 75: Variation of Longitudinal Stresses along the x-direction with welding speed (welded with 3000W Power)

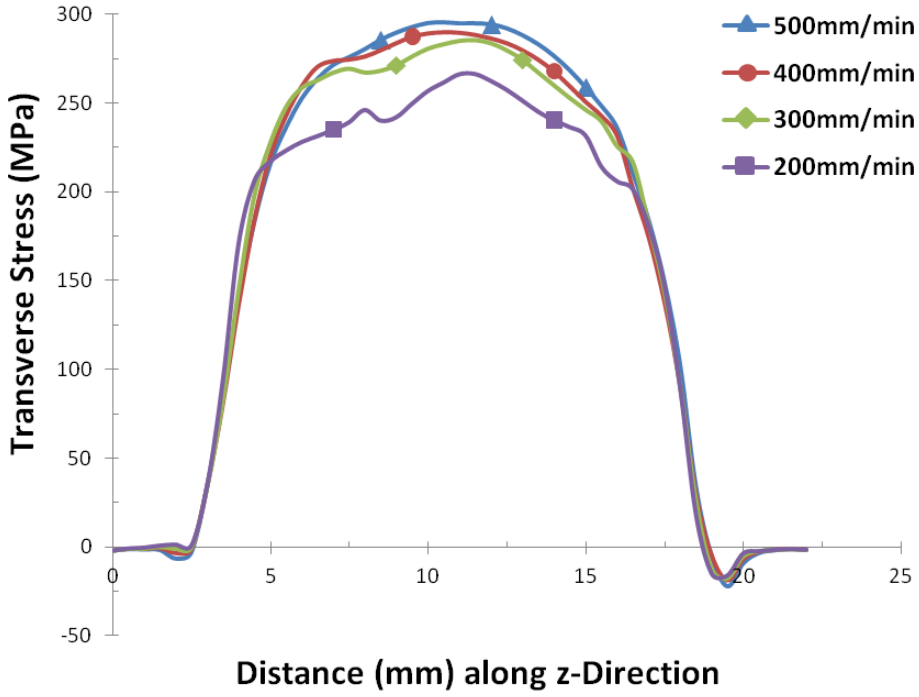

Figure 76: Variation of Transverse Stresses along the z-direction with welding speed (welded with 3000W Power)

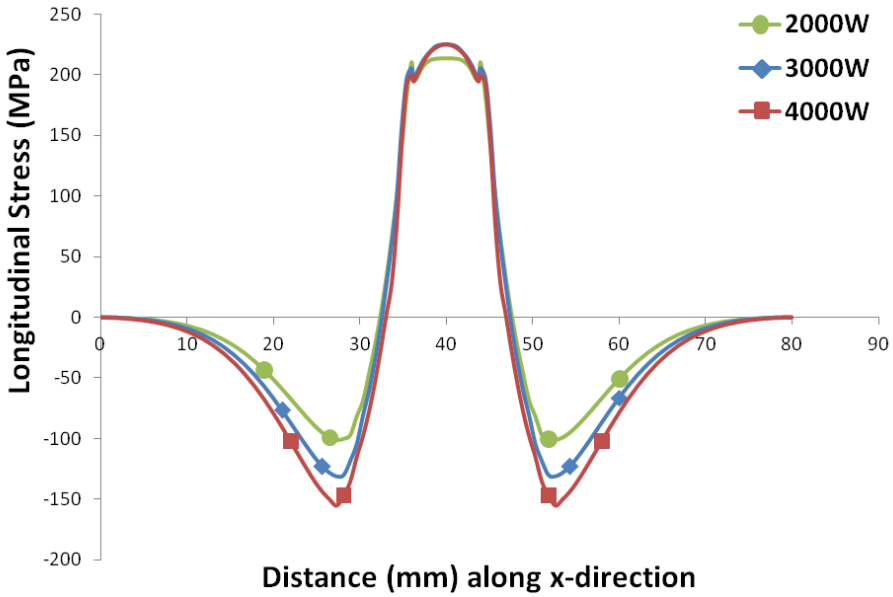

Figure 77: Variation of Longitudinal Stresses along the x-direction with Laser Power (welding speed = 500mm/min)

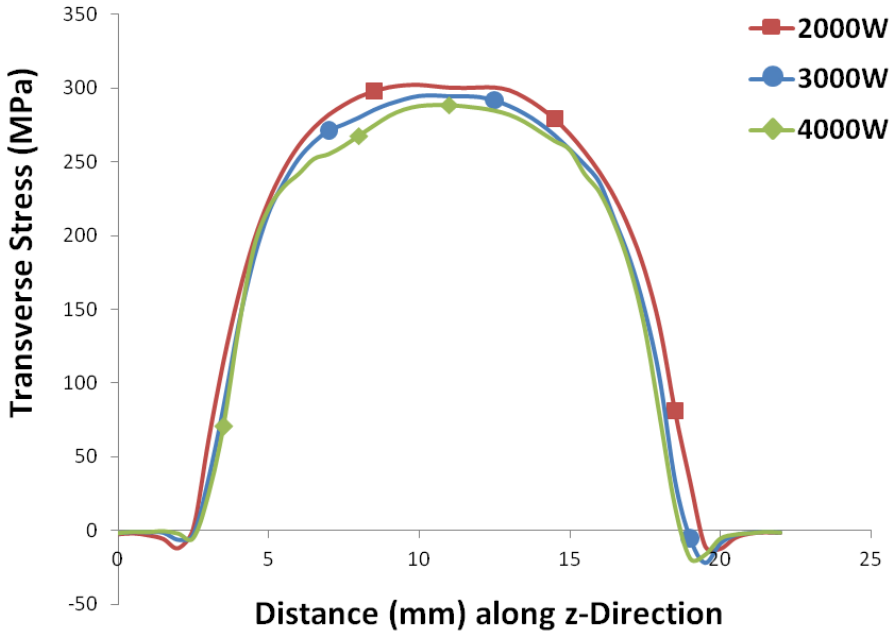

Figure 78: Variation of Transverse Stresses along the z-direction with Laser Power (welding speed = 500mm/min)

CHAPTER SIX

6.0 CONCLUSIONS AND RECOMMENDATIONS

In this section, conclusions from the experiment, characterization and simulation results are presented. Recommendation for future work is also suggested.

6.1 Conclusions

Modal testing and material characterization of laser welded of 316L austenitic stainless steel blanks are carried out. The natural frequency of welded samples is obtained via an experimental set-up coupled with LabView software. The morphological and metallurgical changes in the welded region are examined using the optical microscopy and the SEM. Microhardness distribution across the fusion zone is measured. The sequential-coupled thermo-mechanical analysis is modeled using the finite element method (FEM). The FEM Software Ansys APDL is used to execute the simulations.

It is found that the difference between the natural frequencies of the “as received” and welded samples reaches a maximum of about 12%. The modification of the elastic modulus at the welded region and the subsequent effect on the moment of inertia of the system during the laser welding process are responsible for the new natural frequencies. The parametric study reveals that higher beam power favors the natural frequency due to grain coarsening accompanying increased heat dissipation on the workpiece. Also, direct relationship is also observed for the sample thickness which is associated to increase in the moment of inertia. Increasing the welding speed was found to vary inversely with the natural frequency, but further increase causes an insignificant attenuation of the energy plasma resulting in high heat input, hence, the natural frequency increases. Natural frequencies of the welded samples are correspondingly similar to

that of the “as received” samples for all samples investigated, this confirms the absence of defects and voids within the welded region. The analysis of the experimental results indicates that sample thickness is the most influential parameters that affect the natural frequency.

The post-weld microstructural examination is conducted and the influence of the welding parameters is considered. It is observed that at high laser beam power, evaporation of the sample material occur in the irradiated surface. This causes the formation of a cavity as the laser power intensity further increase, and similar observation is true at a lesser welding speed. This situation is resulted from the excessive laser heating and recoil developed in between the vapor front and the liquid layer. From the optical microscope and SEM microstructure observation, the grain coarsening is evident in the HAZ while highly directional fine grains exist in the fusion zone. Moreover, it is found that dendritic and cellular structures are formed in the weld fusion zone. In addition, detailed examination of welded region reveals that the fusion zone is free from cracks, defect and voids. Increasing laser beam power and welding speed has been found to cause grain coarsening and grain refining respectively. The sample thickness also influences the heat distribution, microstructural development and the weld bead width.

The observed enlargement of the weld bead width at the top of the welding section is as a result of the intermittent variation in the laser power intensity and welding speed at the onset of the welding process. Despite this, no cracks or voids are noticed across this section of the weld. Solidification results in the formation of bainite at the fusion zone with noticeable cementite due to concentration of carbon in this region. While near the neighborhood of the fusion zone dendrtitic microstructures are observed due to the relatively higher cooling rate than that in the fusion zone. The mechanical properties of laser welded butt joints of austenitic steel AISI 316L banks are higher than the properties of the base material.

The temperature distribution and Stress field developed in the welding zone is modeled using the finite element method (FEM) ANSYS software. Double ellipsoidal heat source model is used to model the moving heat source. The temperature profile reveals high temperature gradient and across the fusion zone. The weld bead width is determined from the isotherm of the liquidus temperature of bulk material. The simulated weld bead width agrees well with the measured width from the SEM micrographs. Moreover, once the laser beam scans over the welded region where temperature decays sharply. This causes sharp increase in von Mises stress due to the attainment of high temperature gradient in this region. In general, tensile stresses occur within the fusion zone and compressive stresses are in the bulk material. However, the magnitude of tensile stresses exceeds the compressive stresses for all samples investigated. The compressive stresses in the bulk material gradually decrease from the peak values (close to the fusion boundary) to the minimum at both ends of the welded samples. The Von Mises stress of welded samples with a welding speed of 500mm/min approach the yield stress of the material for different laser beam power studied and it maximum value was about 285MPa for all sample investigated which is still below the material's yield strength.

6.2 Recommendations

The following are areas where future study can be carried out:

1. Further characterization of the flexural response of laser welded sample incorporating other modal parameters like mode shapes, damping ratio, damping coefficient etc. In addition the effect of the impact force on the system response can be considered.

2. Optimization of the Laser welding parameters for welding Austenitic Steels. This becomes necessary due to the wide application of austenitic steels in the various fields and the promising merits of laser beam welding

3. Analysis of microstructural development during laser welding of stainless steel alloys. The understanding of the metallurgical changes during welding is crucial to the resulting mechanical properties of the weldment.

7.0 REFERENCES

[1] A. Ribolla, G. L. Damoulis, and G. F. Batalha, "The use of Nd: YAG laser weld for large scale volume assembly of automotive body in white," *Journal of materials processing technology*, vol. 164, pp. 1120-1127, 2005.

[2] X. B. Liu, G. Yu, J. Guo, Y. J. Gu, M. Pang, C. Y. Zheng, and H. H. Wang, "Research on laser welding of cast Ni-based superalloy K418 turbo disk and alloy steel 42CrMo shaft," *Journal of Alloys and Compounds*, vol. 453, pp. 371-378, 2008.

[3] E. Kannatey-Asibu Jr, *Principles of laser materials processing* vol. 4: Wiley, 2009.

[4] J. Kell, J. R. Tyrer, R. L. Higginson, and R. C. Thomson, "Microstructural characterization of autogenous laser welds on 316L stainless steel using EBSD and EDS," *Journal of microscopy*, vol. 217, pp. 167-173, 2005.

[5] M. Griot, "Basic Laser Principles," in *Introduction to Laser Techonolgy, 36*. vol. 36: Melles Griot, www.mellesgriot.com, pp. 2-32.

[6] C. Joachim Berkmanns and U. Mark Faerber, "Facts About Laser Technology," in *43490816 0105 – 1.1 BBDO*. vol. http://www.linde-gas.com: Linde Gas.

[7] U. Miyachi, "Nd:YAG Laser Welding Guide," Unitek Miyachi Corporation (http://www.unitekmiyachi.com), 2003.

[8] A. M. El-Batahgy, "Effect of laser welding parameters on fusion zone shape and solidification structure of austenitic stainless steels," *Materials Letters*, vol. 32, pp. 155-163, 1997.

[9] M. Sokolov, A. Salminen, V. Somonov, and A. F. H. Kaplan, "Laser welding of structural steels: Influence of the edge roughness level," *Optics & Laser Technology*.

[10] N. S. Shanmugam, Buvanashekaran, G., Sankaranarayanasamy, K., "Experimental investigation and finite element simulation of laser beam welding of AISI 304 stainless steel sheet," *Experimental Techniques*, vol. 34, pp. 25-36, 2010.

[11] A. P. Kyriakongonas, "3D Numerical Modeling of Austenitic Stainless Steel 316L Multi-pass Butt Welding and Comparison with Experimental Results," in *Mechanical Engineering*: Marine Science and Technology.

[12] Z. I. Praisach, G. R. Gillbert, and D. E. Birdeanu, "Considerations on natural frequency changes in damaged cantilever beams using FEM," in *Proceedings of the 3rd WSEAS International Conference on Engineering Mechanics, Structures, Engineering Geology (EMESEG'10), Corfu Island, Greece*.

[13] A. A. V. Deokar and B. V. D. Wakchaure, "Experimental Investigation of Crack Detection in Cantilever Beam Using Natural Frequency as Basic Criterion," *International Conference on Current Trend in technology NUiCONE*, 2011.

[14] M. M. Kaldas and S. M. Dickinson, "The flexural vibration of welded rectangular plates," *Journal of Sound and Vibration*, vol. 75, pp. 163-178, 1981.

[15] S. M. DICKINSON, "Flexural vibration of rectangular plate systems.," in *Mechanical Engineering* Nottingham: The University of Nottingham., 2006.

[16] S. Patarabunditkul, "Natural Frequency Statistics of an Uncertain Plate," in *Mechatronics*: THE UNIVERSITY OF NEW SOUTH WALES, 2009, p. 89.

[17] I. T. Alzaharnah, "Flexural Characteristics of a Cantilever Plate Subjected to Heating at Fixed End," *Journal of Mechanics,* vol. 25, pp. 1-8, 2009.
[18] I. T. Alzaharnah, B. S. Yilbas, and S. A. Al-Kaabi, "Flexural Characteristics of a LaserWelded Cantilever Plate: Influence of Speed of the Heating Source," *Lasers in Engineering,* vol. 18, p. 337, 2008.
[19] I. T. Alzaharnah, S. Al-Kaabi, and B. S. Yilbas, "Effect of Temperature Field on Flexural Wave Characteristics of a Bar Resembling Welding to Rigid Body," *Advanced Materials Research,* vol. 83, pp. 1212-1219, 2010.
[20] I. T. Alzaharnah and B. S. Yilbas, "Investigation into flexural characteristics of a bar subjected to local heating: the effect of heat source location," *Proceedings of the Institution of Mechanical Engineers, Part B: Journal of Engineering Manufacture,* vol. 222, pp. 1355-1362, 2008.
[21] S. J. Hyder, B. S. Yilbas, and S. Z. Shuja, "Flexural motion in laser evaporative heated cantilever workpiece: Three-dimensional analysis," *Optical and quantum electronics,* vol. 35, pp. 111-128, 2003.
[22] B. S. Yilbas, M. Faisal, S. Z. Shuja, and A. F. M. Arif, "Laser pulse heating of steel surface and flexural wave analysis," *Optics and lasers in engineering,* vol. 37, pp. 63-83, 2002.
[23] B. S. Yilbas, S. J. Hyder, and S. Z. Shuja, "Flexural wave generation and stress analysis during laser evaporative heating of steel," *Proceedings of the Institution of Mechanical Engineers, Part C: Journal of Mechanical Engineering Science,* vol. 216, pp. 531-542, 2002.
[24] S. J. Hyder, B. S. Yilbas, and S. Z. Shuja, "Laser induced flexural wave analysis: an aluminum element in steel substrate," *Journal of materials processing technology,* vol. 136, pp. 24-34, 2003.
[25] B. S. Yilbas and S. J. Hyder, "Laser pulse heating and flexural wave generation during treatment of metallic surfaces," *Journal of materials processing technology,* vol. 141, pp. 1-8, 2003.
[26] T. A. Mai and A. C. Spowage, "Characterisation of dissimilar joints in laser welding of steel-kovar, copper-steel and copper-aluminium," *Materials Science and Engineering: A,* vol. 374, pp. 224-233, 2004.
[27] K. Lee and S. Kumai, "Characterization of intermetallic compound layer formed at the weld interface of the defocused laser welded low carbon steel/6111 aluminum alloy lap joint," *Materials transactions,* vol. 47, p. 1178, 2006.
[28] K. Lee, S. Kumai, and T. Arai, "Interfacial microstructure and strength of steel to aluminum alloy lap joints welded by a defocused laser beam," *Materials transactions,* vol. 46, p. 1847, 2005.
[29] C. Yao, B. Xu, X. Zhang, J. Huang, J. Fu, and Y. Wu, "Interface microstructure and mechanical properties of laser welding copperâ€“steel dissimilar joint," *Optics and lasers in engineering,* vol. 47, pp. 807-814, 2009.
[30] E. Taban, E. Deleu, A. Dhooge, and E. Kaluc, "Laser welding of modified 12% Cr stainless steel: Strength, fatigue, toughness, microstructure and corrosion properties," *Materials & Design,* vol. 30, pp. 1193-1200, 2009.
[31] N. Farabi, D. L. Chen, J. Li, Y. Zhou, and S. J. Dong, "Microstructure and mechanical properties of laser welded DP600 steel joints," *Materials Science and Engineering: A,* vol. 527, pp. 1215-1222, 2010.

[32] X. B. Liu, M. Pang, J. Guo, and G. Yu, "Transmission electron microscopy characterization of laser welding cast Ni-based superalloy K418 turbo disk and alloy steel 42CrMo shaft," *Journal of Alloys and Compounds,* vol. 461, pp. 648-653, 2008.
[33] X. B. Liu, G. Yu, M. Pang, J. W. Fan, H. H. Wang, and C. Y. Zheng, "Dissimilar autogenous full penetration welding of superalloy K418 and 42CrMo steel by a high power CW Nd: YAG laser," *Applied surface science*, vol. 253, pp. 7281-7289, 2007.
[34] B. S. Yilbas, M. Sami, J. Nickel, A. Coban, and S. A. M. Said, "Introduction into the electron beam welding of austenitic 321-type stainless steel," *Journal of materials processing technology,* vol. 82, pp. 13-20, 1998.
[35] S. Z. Shuja and B. S. Yilbas, "3-Dimensional conjugate laser heating of a moving slab," *Applied surface science,* vol. 167, pp. 134-148, 2000.
[36] M. PeriÄ‡, D. StamenkoviÄ‡, and V. MilkoviÄ‡, "Comparison of Residual Stresses in Butt-Welded Plates Using Software Packages Abaqus and Ansys," *Scientific Technical Review* vol. Vol. 60, pp. 22-26, 2010.
[37] P. Lacki and K. Adamus, "Numerical simulation of the electron beam welding process," *Computers & Structures,* vol. 89, pp. 977-985, 2011.
[38] M. TurÅˆa, B. Taraba, P. AmbroÅ¾, and M. Sahul, "Contribution to Numerical Simulation of Laser Welding," *Physics Procedia,* vol. 12, pp. 638-645, 2011.
[39] K. Kazemi and J. A. Goldak, "Numerical simulation of laser full penetration welding," *Computational Materials Science,* vol. 44, pp. 841-849, 2009.
[40] A. F. Osamah, "Investigation of Thermal Stress Distribution in Laser Spot Welding Process," *Al-Khwarizmi Engineering Journal,* vol. 5, pp. 33-41, 2009.
[41] A. Capriccioli and P. Frosi, "Multipurpose ANSYS FE procedure for welding processes simulation," *Fusion engineering and Design,* vol. 84, pp. 546-553, 2009.
[42] T. Belendez, C. Neipp, and A. Belendez, "Large and small deflections of a cantilever beam," *European Journal of Physics,* vol. 23, p. 371, 2002.
[43] C. Neipp, "Numerical and experimental analysis of a cantilever beam: a laboratory project to introduce geometric nonlinearity in mechanics of materials," 2003.
[44] D. V. Florica Novăcescu, and Horia Ciocârlie, "The Study of Vibrations of an Elastic System Using the LabView Graphic Programming Medium," *International Journal of Modeling and Optimization,* vol. 2, pp. 208-212, 2012.
[45] J. S. Wu and T. L. Lin, "Free vibration analysis of a uniform cantilever beam with point masses by an analytical-and-numerical-combined method," *Journal of Sound and Vibration,* vol. 136, pp. 201-213, 1990.
[46] J. P. Chopade and R. B. Barjibhe, "Free Vibration Analysis of Fixed Free Beam with Theoretical and Numerical Approach Method," *International Journal of Innovations In Engineering and Technology (IJIET),* vol. 2, pp. 352-356, 2013.
[47] S. G. Kelly, *Fundamentals of Mechanical Vibrations*, Second Edition ed.: McGraw-Hill Higher Education, 2000.
[48] L. Meirovitch, *Elements of Vibration Analysis*, Second Edition ed.: McGraw-Hill Book Company, 1986.
[49] L. Daniel J. Marquez-Chisolm, USAF, "NATURAL FREQUENCES AND MODE SHAPES OF A NONLINEAR, UNIFORM CANTILEVERED BEAM

(MSc Thesis) " in *Department of Aeronautics and Astronautics* Ohio: Air Force Institute of Technology, 2006, p. 195.
[50] T. Sakiyama and M. Huang, "Free vibration analysis of rectangular plates with variable thickness," *Journal of Sound and Vibration,* vol. 216, pp. 379-397, 1998.
[51] N. S. Shanmugam, Buvanashekaran, G., Sankaranarayanasamy, K., Ramesh Kumar, S., "A transient finite element simulation of the temperature and bead profiles of T-joint laser welds," *Materials & Design,* vol. 31, pp. 4528-4542, 2010.
[52] H. S. Carslaw and J. C. Jaeger, "Conduction of heat in solids," *Oxford: Clarendon Press, 1959, 2nd ed.*, vol. 1, 1959.
[53] A. P. Kyriakongonas and V. J. Papazoglou, "3D numerical model of austenitic stainless steel 316L multipass butt welding and comparison with experimental results," *Analysis and design of marine structures,* vol. 1, p. 371, 2009.
[54] A. Trivedi and P. Chauhan, "Modeling of Welding Heat Source for Laser Spot Welding Process," 2011.
[55] A. De, S. K. Maiti, C. A. Walsh, and H. Bhadeshia, "Finite element simulation of laser spot welding," *Science and Technology of Welding & Joining,* vol. 8, pp. 377-384, 2003.
[56] A. Malik, M. Ejaz, and N. Ullah, "Numerical Simulation of Arc Welding Investigation of various Process and Heat Source Parameters," *Failure of Engineering Materials & Structures, Code,* vol. 30, 2007.
[57] C. S. Wu, H. G. Wang, and Y. M. Zhang, "A new heat source model for keyhole plasma arc welding in FEM analysis of the temperature profile," *WELDING JOURNAL-NEW YORK-,* vol. 85, p. 284, 2006.
[58] D. Berglund, A. LundbÃ¤ck, and L. E. Lindgren, "Three-dimensional finite element simulation of laser welded stainless steel plate. NUMIFORM'01," in *Proc. 17th International Conference on Numerical Methods in Industrial Forming Processes*, 2001, pp. 1119-1123.
[59] A. Lundback, "CAD Support for heat input in a FE model," *BOOK-INSTITUTE OF MATERIALS,* vol. 784, pp. 1113-1122, 2002.
[60] X. K. Zhu and Y. J. Chao, "Effects of temperature-dependent material properties on welding simulation," *Computers & Structures,* vol. 80, pp. 967-976, 2002.
[61] D. Deng and H. Murakawa, "Numerical simulation of temperature field and residual stress in multi-pass welds in stainless steel pipe and comparison with experimental measurements," *Computational Materials Science,* vol. 37, pp. 269-277, 2006.
[62] A.-M. El-Batahgy, "Laser Beam Welding of Austenitic Stainless Steels - Similar Butt and Disimilar Lap Joints," *INTECH Open Scienc | Open Minds*, pp. 93-116, 2012.
[63] N. Abu-Dheir and B. S. Yilbas, "Quality Assessment and Metallurgical Examination of Laser Welded Sheets," *Advanced Materials Research* vol. Vols. 83-86 pp. 611-615, 2010.
[64] W. Jiang, Y. Zhang, and W. Woo, "Using heat sink technology to decrease residual stress in 316L stainless steel welding joint: Finite element simulation," *International journal of pressure vessels and piping,* vol. 92, pp. 56-62, 2012.

[65] Database, "MatWeb Material Property Database," http://www.matweb.com/search/DataSheet.aspx?MatGUID=9e9ab696974044cab4a7fd83687934eb&ckck=1.

APPENDIX (Modal test results analysis)

Regression Analysis: NF versus WS, ST, LP, WS*ST, WS*LP, ST*LP

```
* WS*LP is highly correlated with other X variables
* WS*LP has been removed from the equation.


The regression equation is
NF = - 1.4 + 1352 WS + 56175 ST - 0.0035 LP - 1766960 WS*ST + 11.2 ST*LP


Predictor      Coef  SE Coef      T      P      VIF
Constant      -1.38    86.22  -0.02  0.988
WS             1352     7599   0.18  0.867   19.435
ST            56175    50481   1.11  0.328  106.918
LP          -0.00353  0.01903  -0.19  0.862   27.989
WS*ST      -1766960  3914616  -0.45  0.675   37.730
ST*LP         11.23    10.67   1.05  0.352  133.854


S = 7.28232   R-Sq = 99.1%   R-Sq(adj) = 97.9%


Analysis of Variance

Source          DF       SS      MS      F      P
Regression       5  22899.7  4579.9  86.36  0.000
Residual Error   4    212.1    53.0
Total            9  23111.8


Source  DF   Seq SS
WS       1    907.0
ST       1  21127.7
LP       1    765.2
WS*ST    1     41.1
ST*LP    1     58.7
```

Regression Analysis: NF versus WS, ST, LP, WS*ST

```
The regression equation is
NF = - 80.7 + 3425 WS + 104121 ST + 0.0159 LP - 3223172 WS*ST


Predictor      Coef   SE Coef      T      P     VIF
Constant    -80.72     42.31  -1.91  0.115
WS             3425      7418   0.46  0.664  18.129
ST           104121     21985   4.74  0.005  19.851
LP         0.015927  0.004558   3.49  0.017   1.572
WS*ST     -3223172   3701191  -0.87  0.424  33.017


S = 7.36035   R-Sq = 98.8%   R-Sq(adj) = 97.9%


Analysis of Variance

Source          DF       SS      MS       F      P
Regression       4  22840.9  5710.2  105.40  0.000
Residual Error   5    270.9    54.2
Total            9  23111.8


Source  DF   Seq SS
WS       1    907.0
ST       1  21127.7
LP       1    765.2
WS*ST    1     41.1
```

Best Subsets Regression: NF versus WS, ST, LP

Response is NF

Vars	R-Sq	R-Sq(adj)	Mallows Cp	S	W S S	S T	L P
1	93.9	93.1	21.3	13.314		X	
1	49.1	42.8	220.1	38.338			X
2	98.1	97.5	4.6	7.9980		X	X
2	95.3	94.0	16.7	12.405	X	X	
3	98.7	98.0	4.0	7.2106	X	X	X

Regression Analysis: NF versus WS, ST, LP

The regression equation is
NF = - 47.4 - 2842 WS + 85678 ST + 0.0168 LP

Predictor	Coef	SE Coef	T	P	VIF
Constant	-47.43	17.74	-2.67	0.037	
WS	-2842	1759	-1.62	0.157	1.062
ST	85678	5782	14.82	0.000	1.430
LP	0.016753	0.004367	3.84	0.009	1.504

S = 7.21063 R-Sq = 98.7% R-Sq(adj) = 98.0%

PRESS = 784.224 R-Sq(pred) = 96.61%

Analysis of Variance

Source	DF	SS	MS	F	P
Regression	3	22799.8	7599.9	146.17	0.000
Residual Error	6	312.0	52.0		
Total	9	23111.8			

Source	DF	Seq SS
WS	1	907.0
ST	1	21127.7
LP	1	765.2

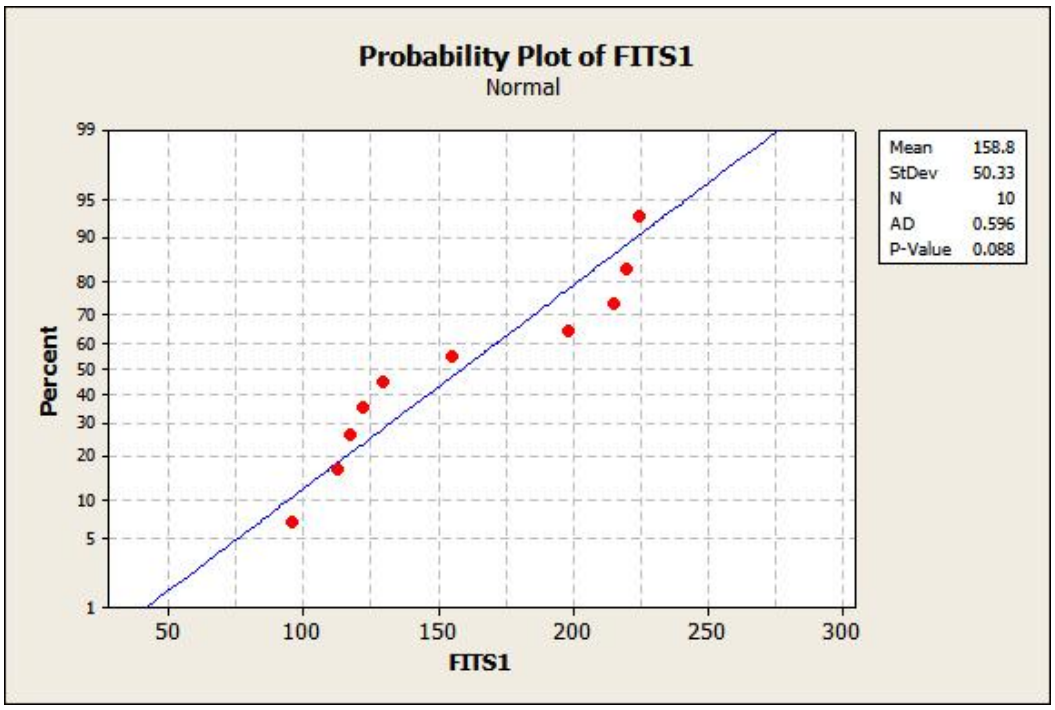
Probability Plot of FITS1
Normal
Mean 158.8
StDev 50.33
N 10
AD 0.596
P-Value 0.088
Percent
FITS1

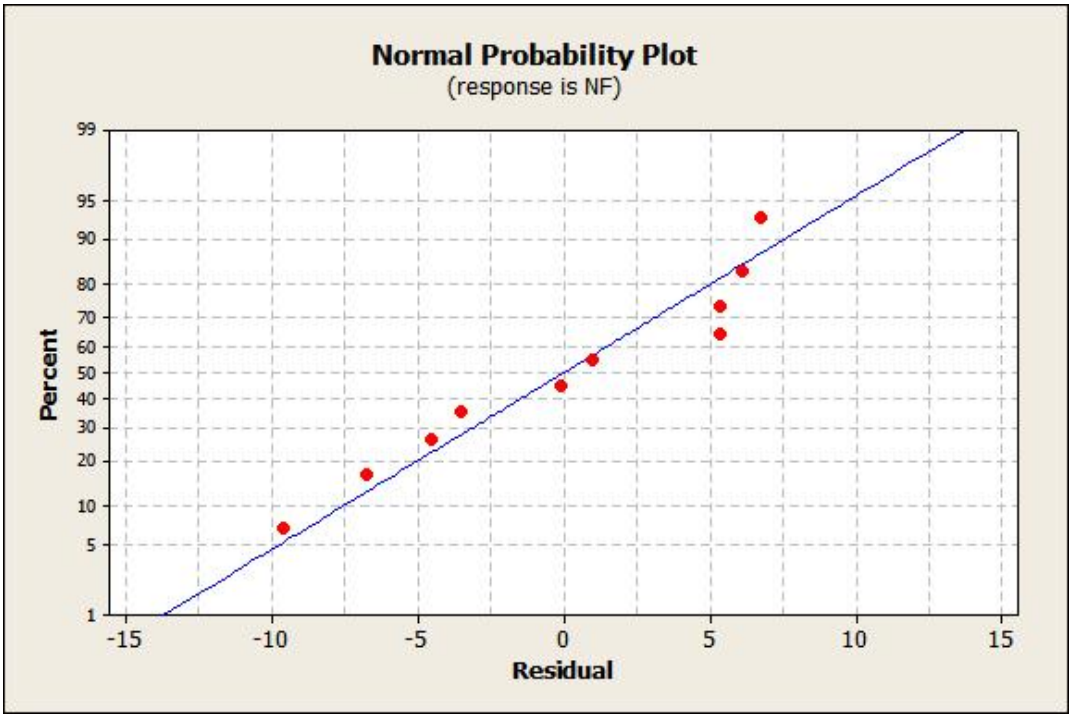
Normal Probability Plot
(response is NF)
Percent
Residual

VITA

Name: Adesina, Akeem Yusuf

Education: Received Bachelor of Science (BSc) in Mechanical Engineering from University of Ado-Ekiti (Now Ekiti State University), Ado-Ekiti, Ekiti State, Nigeria, in 2007

Received Master of Science (MSc) in Mechanical Engineering from King Fahd University of Petroleum & Minerals, Dhahran, Saudi Arabia, in 2013

Contact: al_ubudiyah@yahoo.com